# A Measurement of the Electron Neutrino Component of the T2K Beam using the Near Detector.

by

**Leigh Howard Whitehead**

**Thesis**

Submitted to the University of Warwick

for the degree of

**Doctor of Philosophy**

**Physics**

September 2012

THE UNIVERSITY OF
WARWICK

# Contents

# List of Tables

# List of Figures

# Acknowledgments

I have received brilliant support and encouragement throughout my PhD and would like to thank the following people.

Firstly, I am very grateful to my supervisor Dr Gary Barker for giving me this opportunity. He was a very approachable supervisor and I did not hesitate to ask for advice with any of my work, advice that was always forthcoming. I would also like to thank my co-supervisor Dr Steven Boyd for numerous enlightening discussions. He also listened diligently to my complaints when frustration got the better of me, and his cynicism was the perfect antidote to my troubles. It was very nice to be able to laugh and joke with my supervisors as well as concentrate on the important work. I must also thank them for their thorough reading of this document. The inhabitants of Room 450 provided me with much entertainment as well as wide and varied discussion, both about physics and otherwise. I owe a debt to Dr Phill Litchfield and his vast knowledge of neutrino physics and to Dr David Hadley, Dr Martin Haigh, Dr Antony Carver, Andrew Bennieston, Daniel Scully, Callum Lister and Nicola McConkey for an enjoyable three and a half years in the office.

I must also thank all the members of the T2K collaboration for allowing me the opportunity to contribute to such a great experiment and for providing all the data required to perform the analysis. I sincerely hope that the experiment will go from strength to strength after recovering from the 2011 Earthquake that devastated parts of the Japanese coast. In addition, my thanks also go to the staff at the Users' Office in the IQBRC building in Tokai for all their help during my stay in Japan.

Finally, I come to my family and friends. A special thank you to my wonderful parents Angela and Miles for their endless love, support and encouragement over the last 25 years, I wouldn't be writing this without the brilliant start in life that you provided. A very special thank you also goes to my twin brother and best friend Mark who has always been there for me, through the good times and the bad. He, along with my wonderful friends and extended family, also helped me to cling on to my sanity!

# Declarations

The material presented in this document has not been published or submitted for examination at another institute. It represents my own work unless stated otherwise, complete with references.

Chapter 3 provides a description of the reconstruction of events in the ECals and shows some performance plots. The ECal reconstruction software was written by a number of collaborators, including myself. I actively developed the ECal software for over two years and was in charge of the software package for an eight month period. In addition, I was also responsible for the processing of the testbeam data and was present at CERN when some of the data was taken.

The study presented in Chapter 4 was my own work and used the data taken by the ND280. The analysis software was entirely written by myself and took as input the final outputs from the ND280 reconstruction chain, a software chain written by numerous collaborators. Some of the values used in the selection criteria of the analysis were calculated by collaborators as part of other analyses and are referenced in the chapter.

The work presented in Chapter 5 was produced using software based on an initial version of software produced by other members of the T2K collaboration. However, I adapted the software to generalise the application and also re-wrote many aspects of the software to make it compatible with my requirements and the studies performed with the modified software were my own work. Two of the data samples used in the chapter were obtained from analyses performed by other members of the ND280 collaboration but the other two samples were produced by myself, as described in Chapter 4.

# Abstract

T2K is a long baseline neutrino oscillation experiment located in Japan, with a 295 km baseline and peak neutrino energy of 0.6 GeV. It is the first off-axis neutrino experiment where the beam is directed approximately 2.5° away from the detectors in order to produce a narrow-band neutrino beam. The experiment was designed to measure the mixing angle $\theta_{13}$ by measuring the neutrino oscillation process $\nu_\mu \rightarrow \nu_e$. This measurement relies on the detection of electrons at the far detector from oscillations, and so it is vital to understand the size of the intrinsic $\nu_e$ component of the beam.

A measurement of the intrinsic $\nu_e$ component of the T2K beam was performed using the ND280. An analysis that used all of the data taken by the ND280 from February 2010 until March 2011, a total of $1.09 \times 10^{20}$ POT, measured $67.7 \pm 12.9(stat) \pm 5.2(syst)$ CC $\nu_e$ interactions. The number of events corresponds to a ratio between data and simulation of $0.983 \pm 0.191(stat) \pm 0.076(syst)$ and provides strong evidence that the neutrino flux is well simulated.

The simulation from the intrinsic $\nu_e$ measurement was then combined with an analysis of $\nu_\mu$ interactions in the ND280 to constrain the neutrino flux uncertainties. An idealised study that considered only statistical and flux systematic uncertainties concluded that the intrinsic $\nu_e$ analysis improved the constraint on the flux uncertainties compared to considering only the ND280 $\nu_\mu$ analyses, with the effect most prominent at neutrino energies greater than 1 GeV.

# Chapter 1

# Neutrino Theory and Experimentation

## 1.1 History

The existence of the neutrino was first proposed by Wolfgang Pauli in 1930 as a solution to a problem with energy and momentum conservation in beta decay[1]. At the time beta decay was thought to be a two body process, similar to alpha decay, with the electron as the only outgoing particle. However, the measured energy distribution of the decay electron was inconsistent with the kinematics of a two body decay. Additionally, it was known that angular momentum was not conserved in the two body process. Pauli realised that if there was a third particle involved then it could carry the missing energy and the half integer spin required for angular momentum conservation. No other particle had been detected coming from beta decay so the third particle must have been undetectable at the time. Pauli called his new particle the *neutron*. It was a very controversial idea because very few particles were known and the suggestion of a new undetectable particle was very hard for other physicists to accept without further evidence. For example, Niels Bohr thought that the idea of energy conservation in beta decay should be abandoned. In the following year Enrico Fermi developed a theory of beta decay involving Pauli's suggested particle, renaming it the *neutrino* [2]. Bethe and Peierls showed in 1934 that the cross section of the neutrino interacting with a nucleus via the charged current interaction was [3]:

$$\sigma < 10^{-44}\,\mathrm{cm}^2 \tag{1.1}$$

The article actually ended with a statement that predicted, provided that no other method of interaction other than the charged current weak process existed for neutrinos, “one can conclude that there is no practically possible way of observing the neutrino”.

Fortunately, physicists were able to overcome the very small interaction cross section and in 1959 an experiment by Cowan and Reines provided the first evidence for the (anti)neutrino[4]. The experiment relied on a nuclear reactor to provide a source of antineutrinos to interact with protons in the target mass by the inverse beta decay process:

$$\bar{\nu}_e + p \rightarrow n + e^+ \tag{1.2}$$

The target mass consisted of water mixed with cadmium chloride where the water provided the proton targets and the cadmium was used as a neutron absorber. The experiment had a liquid scintillator detector region surrounding the target. The liquid scintillator was used to detect photons coming from processes initiated by Equation 1.2. Photons were produced by two processes: the annihilation of the positron and the absorption of the neutron. A coincidence of these two processes within a time range of $0.75\,\mu$s to $30\,\mu$s was the signal that an antineutrino had been detected.

In 1962 an experiment in Brookhaven, USA published results from studying high energy neutrinos produced from decaying charged pions in the following way:

$$\pi^- \rightarrow \mu^- + \bar{\nu} \tag{1.3}$$

and the charge conjugate process

$$\pi^+ \rightarrow \mu^+ + \nu \tag{1.4}$$

where no flavour subscripts are shown on the neutrinos because the experiment was built to determine if the neutrinos were different to the neutrinos detected by Cowan and Reines. The detector was designed to measure charged current neutrino interactions so the flavour of the produced charged lepton would determine the flavour of the neutrino. The results showed that the leptons produced in the neutrino interactions were muons, suggesting that the detected neutrinos were very likely to be a distinct type to the previously discovered electron neutrino[5]. These results proved to be the discovery of the muon neutrino.

In 2000, the tau neutrino, postulated to exist since 1975 after the discovery of the tau lepton, was finally detected by the DONuT experiment[6]. The experiment

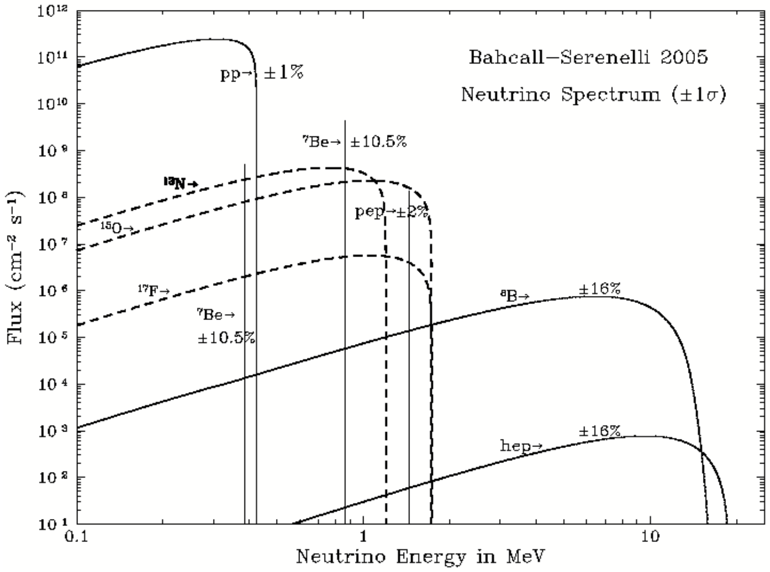

Figure 1.1: The solar neutrino flux as a function of neutrino energy as predicted by the Standard Solar Model. The low energy pp neutrinos make up at least 99% of the total solar neutrino flux. These low energy neutrinos are the hardest to detect because detectors have thresholds that are usually above this energy range. Figure from [8].

used the Tevatron at Fermilab to fire 800 GeV protons into a 1 m thick tungsten beam dump. The detector was positioned 36 m downstream of the beam dump and used various detector technologies, including emulsion and steel target regions. Neutrinos of all three flavours were produced by the protons incident on the target with the $\nu_\tau$ being produced by the decay of the $\tau$ from the decay of the $D_s^-$ meson (consisting of an anti charm quark and a strange quark):

$$D_s^- \to \tau^- + \bar{\nu_\tau} \qquad \tau^- \to \nu_\tau + X \tag{1.5}$$

where $X$ can be a mixture of hadrons and leptons that conserve energy and charge in the process. The event topology was used to distinguish the $\nu_\tau$ interactions from those caused by $\nu_\mu$ or $\nu_e$. The main distinguishing feature is a short track corresponding to the $\tau^-$ before its subsequent decay. In total DONuT measured 578 neutrino interactions with the vertex in the emulsion detector. Nine of the 578 interactions were $\nu_\tau$ interactions with an expected background of 1.5 events [7].

### 1.1.1 The Solar Neutrino Problem

The nuclear fusion processes in the Sun produce vast numbers of electron neutrinos with a range of energies. Figure 1.1 shows the prediction of the Standard Solar Model

(SSM)[8] for the components of the solar neutrino flux coming from the different fusion processes. The first major experiment built to measure solar neutrinos was in the Homestake gold mine in Lead, South Dakota. The detector consisted of 390,000 litres of liquid tetrachlorethylene and worked by a neutrino capture process [9]

$$^{37}\mathrm{Cl} + \nu_e \rightarrow {}^{37}\mathrm{Ar} + e^- \tag{1.6}$$

where the neutrino energy threshold for the reaction is 5.15 MeV. The experiment aimed to measure the Boron-8 neutrino flux, shown by the $^8$B curve in Fig. 1.1, produced by the sun during the H-He fusion process. The results showed that fewer neutrinos were detected than had been expected from the SSM. As a radio-chemical experiment, the neutrino interactions were simply counted by measuring the number of $^{37}$Ar atoms present after a certain period of data taking. No information about the interaction such as the neutrino energy, direction or the interaction time was measured, and therefore it was not known where the neutrinos were coming from or which part of the solar neutrino flux they were from. Assuming that both the experimental procedure and the SSM were correct, the electron neutrinos were going missing in between their creation point in the solar core and their detection on Earth. This anomaly became known as the *Solar Neutrino Problem*.

At least 30 years later, in 1998, Super-Kamiokande (Super-K) was able to provide more information about solar neutrinos. Super-K, a $50,000$ ton water Čerenkov detector, was able to measure the direction of the incoming neutrinos by measuring the direction of the Čerenkov light cones produced by the outgoing charged lepton from the interactions. Super-K measured the solar neutrinos by detecting scattered electrons above the Čerenkov threshold via the elastic scattering process[10]

$$\nu_l + e^- \rightarrow \nu_l + e^- \tag{1.7}$$

where $\nu_l$ represents any flavour of neutrino. Scattering on electrons has a considerably lower energy threshold than nuclear scattering to produce a charged lepton above the Čerenkov threshold and hence is the only way that Super-K can detect the low energy solar neutrinos.

The elastic scattering process can only occur through the neutral current for both the muon and tau neutrinos because the energy required to create a muon or tau is much greater than the neutrino energy. The electron neutrino can undergo this process by both the charged and neutral currents meaning that it has a significantly higher interaction cross-section. The measured neutrino flux was therefore dominated by electron neutrinos even though the neutral current process was technically sensitive to all three neutrino flavours. The processes all had identical final states so it was not possible to separate the charged current and neutral current interactions.

Due to the Čerenkov threshold for detecting electrons from Equation 1.7, Super-K could only measure the $^{8}$B component of the solar neutrino spectrum and saw only 36% of the flux predicted by the SSM[11]. Importantly, the results supported the deficit of neutrinos seen by the Homestake experiment, but other than showing that the neutrinos were definitely coming from the sun, the question concerning what was happening to the electron neutrinos in the solar flux remained.

The solar neutrino flux was also investigated by two Gallium based experiments called SAGE and GALLEX. These radio-chemical experiments used a Gallium target for neutrino interactions as opposed to the Chlorine used by Homestake. The reaction for detecting neutrinos is given below[12]:

$$^{71}\mathrm{Ga} + \nu_e \rightarrow {}^{71}\mathrm{Ge} + e^- \tag{1.8}$$

Gallium was used because the interaction has a very low energy threshold of 233 keV, much lower than that of the Chlorine experiments and Super-K. The low threshold enabled the experiments to probe the pp flux, making up over 99% of the solar neutrino flux (see Figure 1.1). The experiments therefore had considerably more events because they were sensitive to a much larger part of the solar neutrino flux, but as radio-chemical experiments they also lacked the directional and energy information. The two experiments obtained consistent results, measuring approximately half the number of expected electron neutrinos [13, 14]. The measured deficit was different to that measured by Homestake and Super-K, indicating that the process causing electron neutrino disappearance was dependent on the neutrino energy.

The Solar Neutrino Problem was finally solved by the Sudbury Neutrino Observatory (SNO). SNO was a water Čerenkov detector but unlike Super-K it used heavy water as the target mass. The advantage of using Deuterium was that in addition to the elastic scattering process there were two further processes used to detect the solar neutrinos [15]:

$$\nu_e + d \rightarrow e^- + p + p \tag{1.9}$$

$$\nu_l + d \rightarrow p + n + \nu_l \tag{1.10}$$

where $\nu_l$ represents any flavour of neutrino. Equation 1.9 shows the charged current interaction and Equation 1.10 describes the neutral current process. The important difference from Super-K comes from the neutral current process that is sensitive to all three neutrino types. SNO was able to investigate the neutral current process by detecting the neutron capture on deuterium. The neutron capture process produced Čerenkov photons arising from the emission of a 6.25 MeV photon. When looking specifically in the charged current channel SNO measured a lower than expected number of electron neutrinos. However, when looking at the neutral current data it was found that the total number of neutrinos was consistent with the SSM prediction. This meant that the deficit of electron neutrinos was made up for by a surplus in the other two neutrino flavours. This was the first evidence for neutrinos changing flavour, with the electron neutrinos oscillating into the other types of neutrino at some point from their creation in the core of the Sun to the detectors on Earth.

### 1.1.2 The Atmospheric Neutrino Anomaly

Cosmic ray interactions with nuclei in the upper atmosphere produce showers of hadronic particles that decay to produce leptons and hadrons. The production of electron and muon neutrinos in these showers is dominated by the following processes[16]

$$\pi^+ \to \mu^+ + \nu_\mu \qquad \mu^+ \to e^+ + \nu_e + \bar{\nu_\mu} \tag{1.11}$$

and the equivalent charge conjugate processes:

$$\pi^- \to \mu^- + \bar{\nu}_\mu \qquad \mu^- \to e^- + \bar{\nu_e} + \nu_\mu \tag{1.12}$$

Equations 1.11 and 1.12 suggest that the ratio of muon neutrinos to electron neutrinos should be approximately two. Super-K was able to measure the different types of neutrino using the charged current scattering between the neutrino and a nucleon:

$$\nu_l + n \to l^- + \text{hadrons} \tag{1.13}$$

The elastic scattering process used to detect solar neutrinos has a considerably lower cross section and hence made a negligible contribution to the data collected. Super-K measured the ratio to be significantly less than two and sought to determine whether there were too many electron neutrinos, too few muon neutrinos, or a combination of the two. The electron neutrino sample agreed well with expectation but it was found that the number of muon neutrinos was lower than predicted. The difference from the prediction was dependent on both energy and direction. The number of high energy muon neutrinos travelling downwards through the detector was found to agree with the expected value whereas the number of muon neutrinos travelling through the Earth was found to be lower than predicted. The results were analysed using a two flavour neutrino oscillation model and good agreement was seen with the data.

It was clear that the muon neutrinos were oscillating into either electron neutrinos or tau neutrinos. Two reactor experiments, CHOOZ and Palo Verde, were able to determine that $\nu_\mu \rightarrow \nu_e$ oscillations were not responsible, hence the oscillation must be $\nu_\mu \rightarrow \nu_\tau$ [17, 18]. The tau neutrinos were not detected by Super-K due to the high threshold for tau production in Equation 1.13. The first experiment to search for $\nu_\mu \rightarrow \nu_\tau$ oscillations using a neutrino beam is underway at the CNGS - Gran Sasso experiment. The experiment exposes the OPERA detector to a $\nu_\mu$ beam that is used to search for tau neutrinos. In 2010 the first results were released, showing a single tau neutrino candidate[19]. Further events, at the required rate to match the atmospheric results, will be needed to prove beyond doubt that the seen $\tau$ leptons originate from $\nu_\tau$ interactions resultant from $\nu_\mu \rightarrow \nu_\tau$ oscillations.

### 1.1.3 Summary

There are three types of neutrino that have been discovered at the time of writing: the electron neutrino, the muon neutrino and the tau neutrino. The three neutrinos have corresponding antineutrinos, and the number of generations of neutrino matches the number of generations of charged leptons. If a fourth generation of neutrinos were to exist, the mass of the neutrino must be greater than half the mass of the $Z^0$ as no evidence exists for the $Z^0$ decaying to a fourth neutrino state. Neutrino oscillations were an unexpected phenomena and were not predicted by the Standard Model of particle physics, but provided the solution to both the Atmospheric Neutrino Anomaly and the Solar Neutrino Problem.

## 1.2 Neutrino Theory

### 1.2.1 The Standard Model of Particle Physics

The Standard Model (SM) describes the behaviour of the fundamental forces of nature, excluding gravity. It describes the interactions of particles with respect to the electro-magnetic, strong and weak forces. There are 17 particles in the standard model: 6 quarks, 6 leptons, 4 force mediation bosons and the Higgs Boson. The particles also have corresponding antiparticles.

The six quarks are arranged in three generations, with the generations differing only by mass:

$$\begin{pmatrix} u \\ d \end{pmatrix} \begin{pmatrix} c \\ s \end{pmatrix} \begin{pmatrix} t \\ b \end{pmatrix} \tag{1.14}$$

where the $u$, $c$ and $t$ quarks have charge $+\frac{2}{3}$ and the $d$, $s$ and $b$ quarks have charge $-\frac{1}{3}$. Quarks interact with all of the fundamental forces.

The six leptons consist of three charged leptons ($e$, $\mu$ and $\tau$) and three neutrinos ($\nu_e$, $\nu_\mu$ and $\nu_\tau$) , also forming three generations that are identical apart from their masses:

$$\begin{pmatrix} e \\ \nu_e \end{pmatrix} \begin{pmatrix} \mu \\ \nu_\mu \end{pmatrix} \begin{pmatrix} \tau \\ \nu_\tau \end{pmatrix} \tag{1.15}$$

All leptons have no colour charge so they do not interact with the strong force. The charged leptons have charge $-1$ and can therefore interact both with the electromagnetic and weak forces but neutrinos are chargeless particles with respect to the electromagnetic force and hence can only interact by the weak force. Neutrinos were originally treated as massless by the SM, but the discovery of neutrino oscillations demanded that neutrinos were massive. The neutrino masses are very small but non-zero. The masses are at least 5 orders of magnitude lower than the electron, the lightest of the other SM particles.

### 1.2.2 Neutrino Interactions

Neutrino interactions can be separated into two main types based on the boson that mediates the weak interaction. Neutrinos can undergo interactions mediated by both the $W$ and $Z$ bosons, called charged current (CC) and neutral current (NC) processes respectively. All weak interactions conserve lepton flavour at the vertices.

#### Charged Current Processes

There are three main types of CC interactions of a neutrino incident on a nucleon: quasi-elastic (CCQE), resonance (CCRES) and deep inelastic scatting (CCDIS). Figure 1.2 shows the energy dependence of the different interaction cross sections plotted against data from a series of experiments. This plot does not include the newest measurements from experiments such as MiniBooNE, but gives some indication of the accuracy of the measurements, especially at low neutrino energy. The CCQE component is the most important at low energy but at about 1 GeV the resonance processes become equally important. DIS is only a major component of the cross-section above 1 GeV to 2 GeV but dominates the cross-section above 10 GeV. The uncertainties on the cross-section are reasonably large in the low energy range

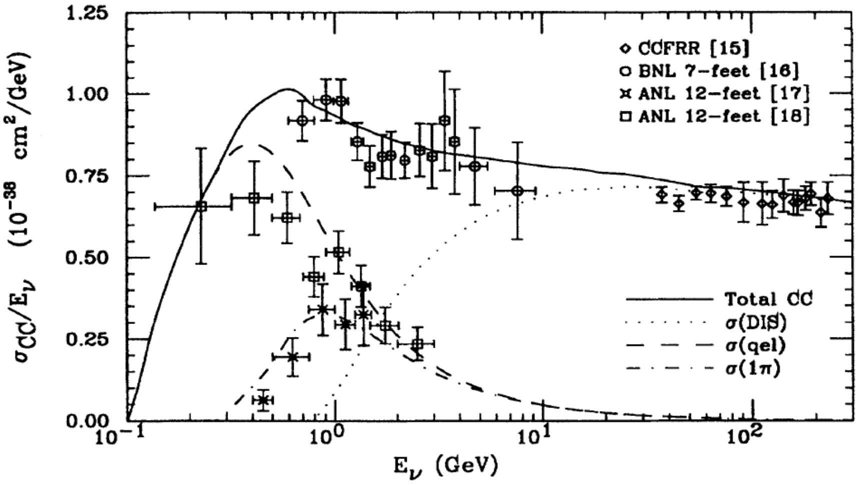

Figure 1.2: A plot of the charged-current cross-section for neutrino-nucleon scattering. The components making up the total cross-section are shown individually where the curves labelled qel and $1\pi$ correspond to the CCQE and CCRES interaction types respectively. Figure taken from [20].

and additional measurements by current experiments are vital in order to improve the understanding of the cross-sections.

Electron neutrinos can also scatter off electrons via a process called elastic scattering, whereby the electron neutrino interacts with an electron with the exchange of a $W$ boson, as shown in the top left of Figure 1.3.

The top right of Figure 1.3 shows the Feynman diagram for the CCQE process of a neutrino of flavour $l$ interacting with a neutron to produce a charged lepton of flavour $l$ and a proton. The CCQE process is the simplest of the charged current processes and allows the neutrino energy to be calculated from the two body kinematics of the final state.

An example of a resonance process is shown in the bottom left of Figure 1.3. In this case, a neutrino $\nu_l$ interacts with a proton to produce a charged lepton $l^-$ and a $\Delta^{++}$ resonance that decays into a proton and a $\pi^+$. Many other resonance processes are possible, with scattering on both initial state neutrons and protons to produce a neutron or a proton and a pion to conserve charge in the final state. Coherent pion production is the name given to resonance events where the momentum transfer to the nucleus is sufficiently small that it remains intact.

The bottom right of Figure 1.3 shows the Feynman diagram for a CCDIS interaction. The neutrino $\nu_l$ interacts with a proton producing a charged lepton $l^-$ and a spray of hadronic particles that conserve charge. A corresponding diagram exists for scattering on a neutron.

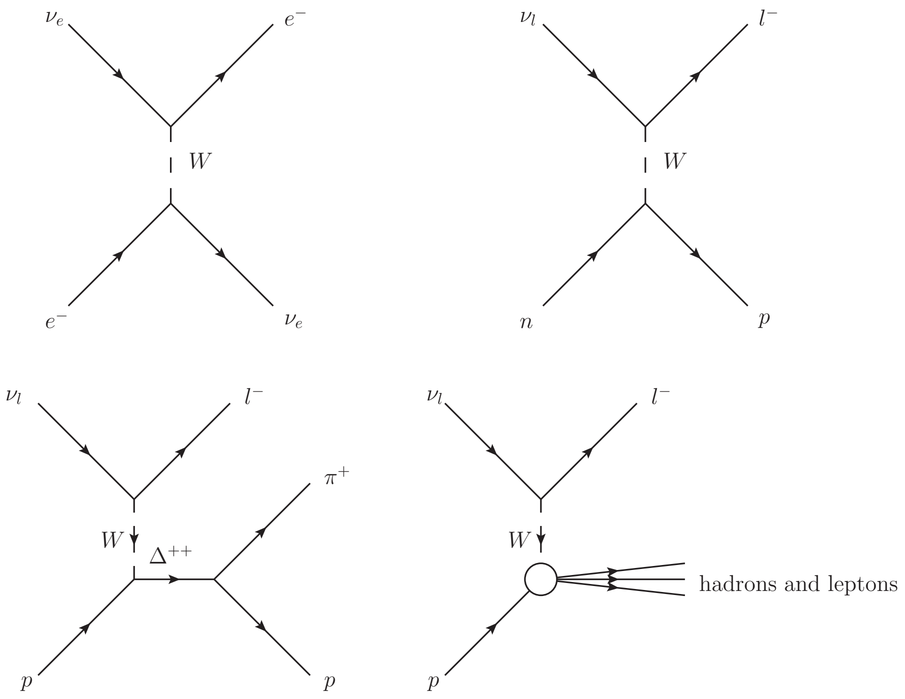

Figure 1.3: Top left: CC elastic scattering of a $\nu_e$ on an electron. Top right: CC scattering of a neutrino of flavour $l$ scattering off of a neutron to produce an $l$ lepton and a proton. Bottom left: CC scattering of a neutrino $\nu_l$ scattering off of a proton to produce an $l^-$ lepton and a $\Delta^{++}$. The $\Delta^{++}$ decays to produce a $\pi^+$ and a proton. Bottom right: CC scattering of a $\nu_l$ scattering off of a proton to produce an $l^-$ and an array of hadrons and leptons.

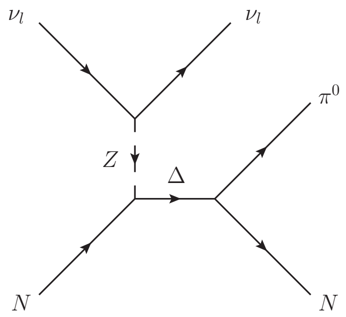

Figure 1.4: A Feynman diagram showing the NC interaction of a neutrino of flavour $l$ with a nucleon $N$ to produce a $\pi^0$ in the final state. The charge of the $\Delta$ is the same as the charge of $N$.

In all neutrino detectors the incoming neutrino is never directly measured. The existence of the neutrino is always inferred by looking for the final state charged lepton. The conservation of lepton flavour at weak vertices means that the detection of a $\mu^-$ from a neutrino interaction means that the incoming neutrino was a $\nu_\mu$.

### Neutral Current Processes

All neutrino flavours can undergo the NC elastic scattering process where the neutrino interacts with an electron, as shown in Equation 1.7.

The three categories of neutrino - nucleon interactions listed for the CC processes also exist for NC processes. The processes are analogous to the CC processes but the charged lepton in the final state is replaced by the corresponding neutrino and the exchange boson is the $Z$ instead of the $W$. NC processes have an interaction cross-section of the order of a third of that of the equivalent CC process[21].

Some of the most important of these are the NC resonance processes that produce a final state $\pi^0$. These processes are particularly important to experiments searching for CC electron neutrino interactions because the decaying $\pi^0$ produces photons than can mimic the electron signal in detectors. The two main processes that contribute to the $\pi^0$ production are:

$$\nu_l + p \rightarrow \nu_l + p + \pi^0 \tag{1.16}$$

$$\nu_l + n \rightarrow \nu_l + n + \pi^0 \tag{1.17}$$

Figure 1.4 shows the Feynman diagram for the processes shown in Equations 1.16 and 1.17, where $N$ represents either a proton or a neutron and the charge of the $\Delta$ matches the charge of the nucleon $N$.

The majority of neutrino detectors used in oscillation experiments are optimised to detect the out-going charged leptons from CC interactions. The fact that NC interactions do not produce a charged lepton means that it is difficult to reconstruct the neutrino energy from any NC interaction. This means that in oscillation experiments the NC interactions form a background to the CC interaction based analyses.

### Cross-Section Models

The CCQE process was parameterised by Llewellyn Smith[22] in 1972 and contains two parameters that were measured by fitting to data: the axial mass $M_A$ and the vector mass $M_V$. These parameters control the hadronic form factors under the assumption of a dipole form factor. The value of $M_V$ is probed from electron scattering but $M_A$ is only accessed from neutrino interactions.

The CCRES and NCRES cross-sections use the same hadronic form factors as the CCQE cross-section but the values of $M_A$ and $M_V$ differ in order to give the best fit to the data.

The DIS interaction in the few GeV neutrino energy scale is parameterised by the Bodek-Yang[23] model. The model includes four parameters that can vary in order for the model to fit data: $A$, $B$, $C_{V1}$ and $C_{V2}$.

The parameters described above are used by neutrino interaction generators to calculate the cross-sections for different interaction processes.

## 1.2.3 Neutrino Oscillations

The discovery of neutrino oscillations meant that neutrinos were known to have mass for the first time. However, the fact that they oscillate means that the mass eigenstates can not be the same as the flavour eigenstates. The flavour eigenstates, $|\nu_\alpha\rangle$, are related to the mass eigenstates, $|\nu_i\rangle$, by the unitary mixing matrix $U_{\alpha i}$[24]:

$$|\nu_\alpha\rangle = \sum_{i=1}^{3} U_{\alpha i}|\nu_i\rangle \tag{1.18}$$

where $U_{\alpha i}$ can be written as the product of three matrices containing three mixing angles $\theta_{12}$, $\theta_{23}$ and $\theta_{13}$ and a complex phase $\delta$, in the parametrisation first suggested by Chau and Keung for the Cabibbo-Kobayashi-Maskawa (CKM) matrix [25]:

$$U = \begin{pmatrix} 1 & 0 & 0 \\ 0 & c_{23} & s_{23} \\ 0 & -s_{23} & c_{23} \end{pmatrix} \begin{pmatrix} c_{13} & 0 & s_{13}e^{-i\delta} \\ 0 & 1 & 0 \\ -s_{13}e^{i\delta} & 0 & c_{13} \end{pmatrix} \begin{pmatrix} c_{12} & s_{12} & 0 \\ -s_{12} & c_{12} & 0 \\ 0 & 0 & 1 \end{pmatrix} \tag{1.19}$$

where $c_{ij} = \cos\theta_{ij}$ and $s_{ij} = \sin\theta_{ij}$.

The matrix $U$ is known as the PMNS (Pontecorvo-Maki-Nakagawa-Sakata) matrix in recognition of early work on neutrino oscillations by Pontecorvo [26] and Maki, Nakagawa and Sakata [27]. The left most matrix describes the atmospheric sector, with oscillations from $\nu_\mu \rightarrow \nu_\tau$. Similarly, the right hand matrix governs the solar sector, with oscillations of $\nu_e \rightarrow \nu_\mu$ and $\nu_e \rightarrow \nu_\tau$. The central matrix containing $\theta_{13}$ is responsible for the oscillation of $\nu_\mu \rightarrow \nu_e$ at the atmospheric mass scale.

$U$ can be expressed as a single matrix by multiplying the three matrices in Equation 1.19:

$$U = \begin{pmatrix} c_{13}c_{12} & c_{13}s_{12} & s_{13}e^{-i\delta} \\ -s_{12}c_{23} - c_{12}s_{23}s_{13}e^{i\delta} & c_{12}c_{23} - s_{23}s_{12}s_{13}e^{i\delta} & s_{23}c_{13} \\ s_{12}s_{23} - c_{12}c_{23}s_{13}e^{i\delta} & -c_{12}s_{23} - c_{23}s_{12}s_{13}e^{i\delta} & c_{23}c_{13} \end{pmatrix} \tag{1.20}$$

Equation 1.18 provides the basis for calculating the probability that a neutrino will oscillate. The flavour states are the states of the weak interaction and determine the interactions of the neutrinos, hence any measurement of neutrinos measures one of the three flavour states. The propagation of neutrinos is governed by the mass states but these are not directly measurable by experiment.

### 1.2.4 Vacuum Neutrino Oscillation Probability

The oscillation probability can be calculated by considering the propagation of neutrino states. Assuming that the neutrino mass states $|\nu_i\rangle$ are plane wave solutions to the time dependent Schrödinger equation gives:

$$|\nu_i(\vec{x}, t)\rangle = e^{-i\phi_i}|\nu_i(\vec{0}, 0)\rangle \tag{1.21}$$

where $\phi_i = p_\mu x^\mu = Et - \vec{p} \cdot \vec{x}$ is the phase of the waveform.

At some time $t$ and position $\vec{x}$ the neutrino flavour state $|\nu_\beta(\vec{x}, t)\rangle$ is measured. The flavour state can be expressed in terms of the mass states according to

Equation 1.18. Combining this with Equation 1.21 gives

$$|\nu_\beta(\vec{x},t)\rangle = \sum_i U_{\beta i} e^{-i\phi_i} |\nu_i(\vec{0},0)\rangle \tag{1.22}$$

If the neutrino source is considered to be pure in flavour $|\nu_\alpha\rangle$ at time $t = 0$ and position $\vec{x} = \vec{0}$ then the probability of measuring $|\nu_\beta(\vec{x},t)\rangle$ is given by

$$P(\nu_\alpha \to \nu_\beta) = |\langle \nu_\beta(\vec{x},t)|\nu_\alpha(\vec{0},0)\rangle|^2 \tag{1.23}$$

$\langle \nu_\beta(\vec{x},t)|$ is obtained by taking the complex conjugate of Equation 1.22

$$\langle \nu_\beta(\vec{x},t)| = \sum_i U^*_{\beta i} e^{i\phi_i} \langle \nu_i(\vec{0},0)| \tag{1.24}$$

and hence:

$$\langle \nu_\beta(\vec{x},t)|\nu_\alpha(\vec{0},0)\rangle = \sum_i U^*_{\beta i} e^{i\phi_i} \langle \nu_i(\vec{0},0)|\nu_\alpha(\vec{0},0)\rangle \tag{1.25}$$

Expanding $|\nu_\alpha(\vec{0},0)\rangle$ on the right-hand side into the mass states using Equation 1.18 gives the oscillation amplitude

$$\langle \nu_\beta(\vec{x},t)|\nu_\alpha(\vec{0},0)\rangle = \sum_i \sum_j U^*_{\beta i} U_{\alpha j} e^{i\phi_i} \langle \nu_i(\vec{0},0)|\nu_j(\vec{0},0)\rangle \tag{1.26}$$

The term $\langle \nu_i(\vec{0},0)|\nu_j(\vec{0},0)\rangle = 1$ if $i = j$ and is equal to zero for all other cases due to the orthogonality of the mass eigenstates, hence Equation 1.26 simplifies to give:

$$\langle \nu_\beta(\vec{x},t)|\nu_\alpha(\vec{0},0)\rangle = \sum_i U^*_{\beta i} U_{\alpha i} e^{i\phi_i} \tag{1.27}$$

Now consider the phases $\phi_i$ for a neutrino travelling in the $x$ direction:

$$\phi_i = E_i t - \vec{p_i} \cdot \vec{x} = E_i t - p_i x \tag{1.28}$$

The assumption of plane wave solutions means that some additional assumptions are required at this stage. Using the common convention of equal momenta for the mass states gives:

$$p_i = p = \sqrt{E_i^2 - m_i^2} = E_i \sqrt{1 - \frac{m_i^2}{E_i^2}} \approx E_i \left(1 - \frac{m_i^2}{2E_i^2}\right) \tag{1.29}$$

Using the relativistic approximation $x = t = L$ where $L$ is the distance travelled by the neutrino and $m_i << E_i$ means that the $E_i$ can be replaced by the average energy $E$. Then substituting Equation 1.29 into Equation 1.28 gives:

$$\phi_i = EL - EL\left(1 - \frac{m_i^2}{2E^2}\right) = \frac{m_i^2 L}{2E} \tag{1.30}$$

As mentioned, the assumptions made here are an artifact of assuming that the mass states have plane wave solutions. If the mass states are treated as wave packets then this assumption is not required but leads to the same result. The proof of this result is given in [24].

Substituting Equation 1.30 into Equation 1.27

$$\langle \nu_\beta(L) | \nu_\alpha(0,0) \rangle = \sum_i U_{\beta i}^* U_{\alpha i} e^{i\frac{m_i^2 L}{2E}} \tag{1.31}$$

and hence the oscillation probability is obtained by taking the modulus-squared:

$$P(\nu_\alpha \to \nu_\beta) = \sum_i U_{\beta i}^* U_{\alpha i} e^{i\frac{m_i^2 L}{2E}} \sum_j U_{\beta j} U_{\alpha j}^* e^{-i\frac{m_j^2 L}{2E}} \tag{1.32}$$

Setting $\Delta m_{ij}^2 = m_i^2 - m_j^2$ gives the following

$$P(\nu_\alpha \to \nu_\beta) = \sum_i \sum_j U_{\beta i}^* U_{\alpha i} U_{\beta j} U_{\alpha j}^* e^{i\frac{\Delta m_{ij}^2 L}{2E}} \tag{1.33}$$

Equation 1.33 can be expanded to give

$$P(\nu_\alpha \to \nu_\beta) = \sum_i \sum_j U_{\beta i}^* U_{\alpha i} U_{\beta j} U_{\alpha j}^* + \sum_i \sum_j U_{\beta i}^* U_{\alpha i} U_{\beta j} U_{\alpha j}^* \left(e^{i\frac{\Delta m_{ij}^2 L}{2E}} - 1\right) \tag{1.34}$$

The first term here is equal to $\delta_{\alpha\beta}$ by unitarity. The value of the second term for values of $i < j$ is equal to the complex conjugate of values for $i > j$ and zero for $i = j$, hence Equation 1.34 becomes

$$P(\nu_\alpha \to \nu_\beta) = \delta_{\alpha\beta} + 2\sum_{i>j} \mathfrak{Re}\left[U_{\beta i}^* U_{\alpha i} U_{\beta j} U_{\alpha j}^* \left(e^{i\frac{\Delta m_{ij}^2 L}{2E}} - 1\right)\right] \tag{1.35}$$

The real and imaginary parts of $\left(e^{i\frac{\Delta m_{ij}^2 L}{2E}} - 1\right)$ can be separated

$$\mathfrak{Re}\left(e^{i\frac{\Delta m_{ij}^2 L}{2E}} - 1\right) = \cos\left(\frac{\Delta m_{ij}^2 L}{2E}\right) - 1 = -2\sin^2\left(\frac{\Delta m_{ij}^2 L}{4E}\right) \tag{1.36}$$

$$\mathfrak{Im}\left(e^{i\frac{\Delta m_{ij}^2 L}{2E}}-1\right)=\sin\left(\frac{\Delta m_{ij}^2 L}{2E}\right) \tag{1.37}$$

allowing Equation 1.35 to be expanded to give the oscillation probability as:

$$\begin{aligned}P(\nu_\alpha\to\nu_\beta)=\delta_{\alpha\beta}-4\sum_{i>j}\mathfrak{Re}\left[U_{\beta i}^*U_{\alpha i}U_{\beta j}U_{\alpha j}^*\right]\sin^2\left(\frac{\Delta m_{ij}^2 L}{4E}\right)\\+2\sum_{i>j}\mathfrak{Im}\left[U_{\beta i}^*U_{\alpha i}U_{\beta j}U_{\alpha j}^*\right]\sin\left(\frac{\Delta m_{ij}^2 L}{2E}\right)\end{aligned} \tag{1.38}$$

The value of $P(\nu_\alpha\to\nu_\beta)$ when $\alpha\neq\beta$ provides the appearance probability of $\nu_\beta$ in an initially pure $\nu_\alpha$ beam. The special case when $\alpha=\beta$ gives the survival probability of $\nu_\alpha$. In the survival probability case Equation 1.38 simplifies because $U_{\alpha i}^*U_{\alpha i}U_{\alpha j}U_{\alpha j}^*=|U_{\alpha i}|^2|U_{\alpha j}|^2$ is a real number, hence the imaginary term goes to zero.

$$P(\nu_\alpha\to\nu_\alpha)=1-4\sum_{i>j}|U_{\alpha i}|^2|U_{\alpha j}|^2\sin^2\left(\frac{\Delta m_{ij}^2 L}{4E}\right) \tag{1.39}$$

### 1.2.5 Three Flavour Oscillation Probability

The three flavour oscillation probabilities can be calculated using Equation 1.38 or 1.39 for $i,j=1,2$ or 3 with $U=U_{PMNS}$ as defined in Equation 1.20. For a long baseline $\nu_\mu$ beam experiment the two important probabilities are the $\nu_\mu$ survival probability and the $\nu_e$ appearance probability. The $\nu_\mu$ survival probability is:

$$\begin{aligned}P(\nu_\mu\to\nu_\mu)=1-4|U_{\mu 3}|^2|U_{\mu 2}|^2\sin^2\left(\frac{\Delta m_{32}^2 L}{4E}\right)\\-4|U_{\mu 3}|^2|U_{\mu 1}|^2\sin^2\left(\frac{\Delta m_{31}^2 L}{4E}\right)\\-4|U_{\mu 2}|^2|U_{\mu 1}|^2\sin^2\left(\frac{\Delta m_{21}^2 L}{4E}\right)\end{aligned} \tag{1.40}$$

Converting to SI units, measuring $\Delta m_{ij}^2$ in eV$^2$, $L$ in km and $E$ in GeV, the arguments of the sine terms become

$$\frac{\Delta m_{ij}^2 L}{4E}=\frac{1.27\Delta m_{ij}^2 L}{E} \tag{1.41}$$

Equation 1.40 can be simplified by taking $\Delta m_{32}^2=\Delta m_{31}^2=\Delta m^2$ and also by noting the dependence of the terms on $\frac{L}{E}$. The equations also show that the oscillation probability depends on two parameters that are free to be chosen by experimental design. The values of $L$ and $E$ can be chosen to give an $\frac{L}{E}$ ratio that maximises the oscillation probability such that:

$$\frac{L}{E} = \frac{\pi}{2}\frac{1}{1.27\Delta m^2} \tag{1.42}$$

In this case the experiments are optimised to look for oscillations caused by the mass splitting $\Delta m^2$ and hence the final term in Equation 1.40 can be neglected as it is suppressed by a factor of $\sim 400$, giving the $\nu_\mu$ survival probability as:

$$\begin{aligned}
P(\nu_\mu \rightarrow \nu_\mu) &= 1 - 4|U_{\mu 3}|^2 \left(|U_{\mu 2}|^2 + |U_{\mu 1}|^2\right) \sin^2\left(\frac{1.27\Delta m^2 L}{E}\right) \\
&= 1 - 4|U_{\mu 3}|^2 \left(1 - |U_{\mu 3}|^2\right) \sin^2\left(\frac{1.27\Delta m^2 L}{E}\right) \\
&= 1 - 4\cos^2\theta_{13}\sin^2\theta_{23}\left(1 - \cos^2\theta_{13}\sin^2\theta_{23}\right)\sin^2\left(1.27\Delta m^2 \frac{L}{E}\right)
\end{aligned} \tag{1.43}$$

The appearance probability $P(\nu_\mu \rightarrow \nu_e)$ is calculated in a similar way using Equations 1.38 and 1.20 to give the result:

$$\begin{aligned}
P(\nu_\mu \rightarrow \nu_e) = &- 4\mathfrak{Re}\left[U^*_{e3}U_{\mu 3}U_{e2}U^*_{\mu 2}\right]\sin^2\left(\frac{\Delta m^2_{32}L}{4E}\right) \\
&- 4\mathfrak{Re}\left[U^*_{e3}U_{\mu 3}U_{e1}U^*_{\mu 1}\right]\sin^2\left(\frac{\Delta m^2_{31}L}{4E}\right) \\
&- 4\mathfrak{Re}\left[U^*_{e2}U_{\mu 2}U_{e1}U^*_{\mu 1}\right]\sin^2\left(\frac{\Delta m^2_{21}L}{4E}\right) \\
&+ 2\mathfrak{Im}\left[U^*_{e3}U_{\mu 3}U_{e2}U^*_{\mu 2}\right]\sin\left(\frac{\Delta m^2_{32}L}{2E}\right) \\
&+ 2\mathfrak{Im}\left[U^*_{e3}U_{\mu 3}U_{e1}U^*_{\mu 1}\right]\sin\left(\frac{\Delta m^2_{31}L}{2E}\right) \\
&+ 2\mathfrak{Im}\left[U^*_{e2}U_{\mu 2}U_{e1}U^*_{\mu 1}\right]\sin\left(\frac{\Delta m^2_{21}L}{2E}\right)
\end{aligned} \tag{1.44}$$

As before, taking $\Delta m^2_{32} = \Delta m^2_{31} = \Delta m^2$ and neglecting terms from the suppressed solar mass scale reduces the expression to two terms:

$$\begin{aligned}
P(\nu_\mu \rightarrow \nu_e) = &- 4\left(\mathfrak{Re}\left[U^*_{e3}U_{\mu 3}U_{e2}U^*_{\mu 2}\right] + \mathfrak{Re}\left[U^*_{e3}U_{\mu 3}U_{e1}U^*_{\mu 1}\right]\right)\sin^2\left(\frac{\Delta m^2 L}{4E}\right) \\
&+ 2\left(\mathfrak{Im}\left[U^*_{e3}U_{\mu 3}U_{e2}U^*_{\mu 2}\right] + \mathfrak{Im}\left[U^*_{e3}U_{\mu 3}U_{e1}U^*_{\mu 1}\right]\right)\sin\left(\frac{\Delta m^2 L}{2E}\right)
\end{aligned} \tag{1.45}$$

Substituting the values for the components of $U$ from Equation 1.20 reduces the imaginary term to zero and writing the oscillation term according to Equation 1.41 gives the $\nu_e$ appearance probability as:

$$\begin{aligned} P(\nu_\mu \rightarrow \nu_e) &= 4c_{13}^2 s_{13}^2 s_{23}^2 \sin^2\left(1.27\Delta m^2 \frac{L}{E}\right) \\ &= \sin^2 2\theta_{13} \sin^2\theta_{23} \sin^2\left(1.27\Delta m^2 \frac{L}{E}\right) \end{aligned} \tag{1.46}$$

It can be seen from Equation 1.46 that $\theta_{13}$ can not be measured directly in accelerator beam experiments, it must always be extracted using the current world best measurements of $\sin^2\theta_{23}$ and $\Delta m^2$.

### 1.2.6 CP Violation

The combined operation of charge conjugation C and parity P is known as CP. Charge conjugation is the operation that converts a particle into the corresponding antiparticle and the parity operator reverses the directions of the spatial coordinates such that $P(x, y, z, t) \rightarrow P(-x, -y, -z, t)$.

The complex phase $\delta$ was introduced in Equation 1.19 and allows for CP violation in the neutrino sector. If the solar terms are not neglected in the expansion of $P(\nu_\mu \rightarrow \nu_e)$ in Equation 1.45 then two terms containing $\delta$ arise: a term containing $\cos\delta$ and a term containing $\sin\delta$. The $\cos\delta$ term is CP-even and hence does not cause a difference in oscillation probability between neutrinos and antineutrinos. However, the $\sin\delta$ term is CP-odd and changes sign between neutrinos and antineutrinos, producing a difference between the oscillation probabilities. It is clear from Equation 1.39 that no CP-violation can be measured from experiments measuring survival probability because there is no contribution from imaginary terms, and hence no terms containing $\sin\delta$.

The $\sin\delta$ term is also multiplied by $\sin\theta_{13}$ so a non-zero value of $\theta_{13}$ is required to be able to measure CP-violation. This would lead to the conclusion that an optimal value of $\theta_{13}$ would be large. However, the picture is complicated by considering the CP asymmetry[28]:

$$A_{CP} = \frac{P(\nu_\mu \rightarrow \nu_e) - P(\bar{\nu}_\mu \rightarrow \bar{\nu}_e)}{P(\nu_\mu \rightarrow \nu_e) + P(\bar{\nu}_\mu \rightarrow \bar{\nu}_e)} \propto \frac{\sin\delta}{\sin\theta_{13}} \tag{1.47}$$

The CP asymmetry is inversely proportional to $\sin\theta_{13}$, meaning that a small value of $\theta_{13}$ would be optimal for measuring $A_{CP}$. The left plot in Figure 1.5 shows the CP asymmetry for a typical neutrino oscillation experiment and shows that for values

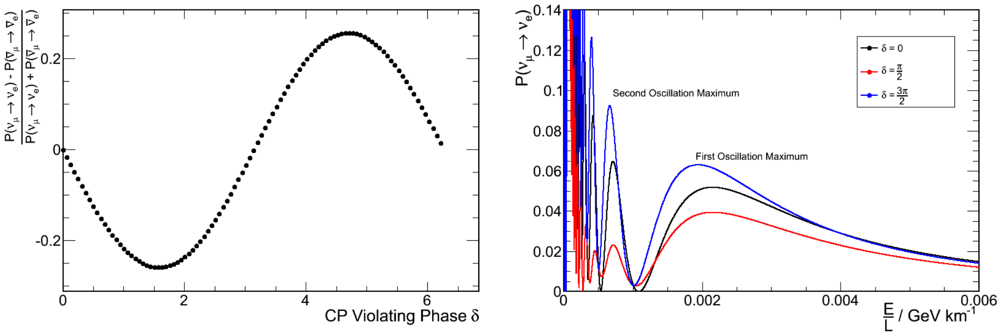

Figure 1.5: Left: The CP asymmetry plotted as a function of $\delta$ for a baseline of 295 km and a neutrino energy of 0.6 GeV. The values used for the oscillation parameters were from [29] and $\sin^2 2\theta_{13} = 0.1$. Right: $P(\nu_\mu \rightarrow \nu_e)$ plotted as a function of $\frac{E}{L}$ for three values of $\delta$: 0 and the values corresponding to the minimum and maximum asymmetry, $\frac{\pi}{2}$ and $\frac{3\pi}{2}$. The right most peak corresponds to the position of the first oscillation maximum.

of $\delta$ close to $\frac{\pi}{2}$ or $\frac{3\pi}{2}$ that the asymmetry is relatively large.

There are two main methods that could be used to probe $\delta$ using a high intensity long baseline $\nu_\mu$ experiment. If the beam polarity can be changed by reversing the current in the magnetic horn then the beam can be converted from $\nu_\mu$ to $\bar{\nu_\mu}$ and then measure the CP asymmetry $A_{CP}$, and hence measure $\delta$. Alternatively, an experiment could have detectors covering both the first and second oscillation maxima. The right plot in Figure 1.5 shows the oscillation probability as a function of $\frac{E}{L}$ for different values of $\delta$. The value of delta has a clear effect on the probability curves, with the red curve corresponding to $\delta = \frac{\pi}{2}$, and the blue curve to $\delta = \frac{3\pi}{2}$. The relative effect of $\delta$ differs between the first two oscillation maxima, and would allow the value of $\delta$ to be extracted by measuring the oscillation probability at the first and second maxima.

### 1.2.7 Neutrino Oscillations in Matter

Neutrinos interact in matter as they propagate meaning that they have an effective mass that is different from their vacuum mass. The effective mass change can produce a change in the mixing angles, causing the oscillation probability in matter to differ from the vacuum oscillation probability. The effect of matter on neutrino oscillations is called the MSW effect, named after Wolfenstein, Mikheyev and Smirnov, as a result of their work on the subject [30] [31]. Consider for simplicity the case with only two neutrino generations, $\nu_e$ and $\nu_\mu$. The vacuum oscillation probability $P(\nu_\mu \rightarrow \nu_e)$ in this case can be calculated using Equation 1.38 and a $2 \times 2$ rotation matrix

$$U = \begin{pmatrix} \cos\theta & \sin\theta \\ -\sin\theta & \cos\theta \end{pmatrix} \tag{1.48}$$

and it follows that

$$P(\nu_\mu \to \nu_e) = \sin^2 2\theta \sin^2 \left(1.27\Delta m^2 \frac{L}{E}\right) \tag{1.49}$$

In matter, all three neutrino types can undergo NC scattering off nucleons and electrons but electron neutrinos interact differently to other neutrinos because they can undergo a CC elastic scattering process where a $\nu_e$ scatters off an electron via the exchange of a $W$ boson. The NC interactions are responsible for an absolute change in the mass states but do not create a change in the mass splittings, since all neutrino flavours are affected in the same way. However, since the CC elastic scattering process only occurs for electron neutrinos there is a change in the mass splittings. It can be shown that the two flavour oscillation probability in matter is given by[32]

$$P(\nu_\mu \to \nu_e) = \sin^2 2\theta_M \sin^2 \left(1.27\Delta m_M^2 \frac{L}{E}\right) \tag{1.50}$$

where the oscillation parameters are related to the vacuum oscillation parameters in the following way:

$$\sin^2 2\theta_M = \frac{\sin^2 2\theta}{\sin^2 2\theta + (\cos 2\theta - x_\nu)^2} \tag{1.51}$$

and

$$\Delta m_M^2 = \Delta m^2 \sqrt{\sin^2 2\theta + (\cos 2\theta - x_\nu)^2} \tag{1.52}$$

with

$$x_\nu = \frac{2\sqrt{2} G_F N_e E}{\Delta m^2} \tag{1.53}$$

where $G_F$ is the Fermi constant, $N_e$ is the electron number density and $E$ is the neutrino energy. $x_\nu$ provides a measure of how important the matter effects are for a given set of parameters and for the case where $N_e \to 0$, Equation 1.50 reduces to the vacuum oscillation probability, given in Equation 1.49. The matter effects are most pronounced for neutrinos with an energy close to the resonant energy such that $x_\nu = \cos 2\theta$ and $\sin^2 2\theta_M = 1$, where variations from the vacuum oscillation probability can be large and also vary with energy. For matter effects on earth the only free variable in equation 1.53 is $E$, meaning that the relative size of matter effects scales linearly with energy, making it more important for high energy neutrinos. For antineutrinos $x_\nu \rightarrow -x_\nu$ so a difference can be observed between the oscillation probabilities of neutrinos and antineutrinos.

### 1.2.8 Neutrino Mass Hierarchy

The absolute values of the masses of the neutrino mass states are not known but details about the differences between the values have been measured. The most widely used mass differences are $\Delta m^2_{32} = m^2_3 - m^2_2$ and $\Delta m^2_{21} = m^2_2 - m^2_1$ because these correspond to the mass splittings responsible for the atmospheric and solar oscillations respectively. The current values for the two mass splittings are summarised below [29]:

$$|\Delta m^2_{32}| = 2.43 \pm 0.13 \times 10^{-3}\,\mathrm{eV}^2 \tag{1.54}$$

$$\Delta m^2_{21} = 7.59^{+0.20}_{-0.21} \times 10^{-5}\,\mathrm{eV}^2 \tag{1.55}$$

The vacuum neutrino oscillation probabilities do not depend on the sign of the mass splittings because the oscillatory sine term containing $\Delta m^2$ is squared in the equation. However, it was shown in Equation 1.53 that matter oscillations have an intrinsic dependence on the sign of $\Delta m^2$. Measurements of the solar mass splitting $\Delta m^2_{21}$ come from matter oscillations because the neutrinos oscillate inside the core of the Sun, hence the sign of $\Delta m^2_{21}$ is known. Conversely, the atmospheric neutrino mass splitting $\Delta m^2_{32}$ is measured from vacuum neutrino oscillations and hence the sign of $\Delta m^2_{32}$ is not known.

Figure 1.6 shows a graphical representation of the mass hierarchy with the normal hierarchy ($\Delta m^2_{32} > 0$) on the left and the inverted hierarchy ($\Delta m^2_{32} < 0$) on the right. A very long baseline experiment will be required to measure the sign of $\Delta m^2_{32}$ so that the matter effects are not negligible in the oscillation probability.

### 1.2.9 Majorana Neutrinos

In 1937 Ettore Majorana proposed a theory that allowed neutral fermions to be identical to their antiparticles [33]. Such particles are now known as Majorana particles. If neutrinos are Majorana particles then the expression given in Equation 1.19 needs to be extended to account for two phases that can no longer be absorbed by redefining fields[12]:

$$U = U_{\mathrm{PMNS}} \begin{pmatrix} 1 & 0 & 0 \\ 0 & e^{i\alpha} & 0 \\ 0 & 0 & e^{i\beta} \end{pmatrix} \tag{1.56}$$

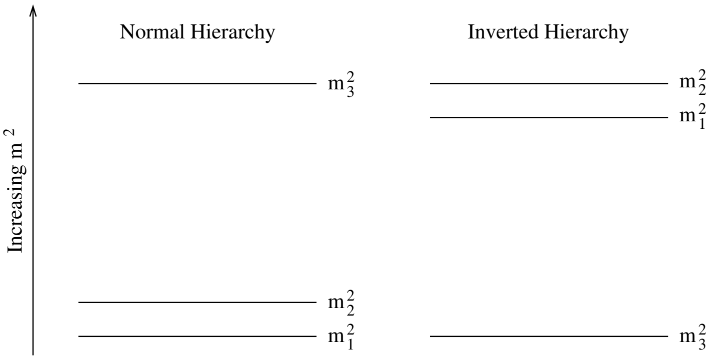

Figure 1.6: The neutrino mass hierarchy shown for both the normal (left) and inverted (right) schemes. The actual form of the hierarchy is not known because the sign of $\Delta m^2_{32}$ is unknown. The relative sizes of $\Delta m^2_{32}$ and $\Delta m^2_{21}$ are not shown to scale.

where $\alpha$ and $\beta$ are the two Majorana phases. These phases are not measurable by neutrino oscillation experiments because oscillation probabilities depend on the modulus squared and these complex phases cancel in the calculations. This behaviour is expected because neutrino oscillations do not cause mixing between neutrinos and antineutrinos. In order to measure the Majorana phases, an experiment would need to look at a process that involved the mixing of neutrinos and antineutrinos, such as the proposed neutrino-less double beta decay process.

Fermions in the standard model have Dirac masses $m_D$ from the coupling of the left and right-handed chiral states. No right-handed neutrino state has been observed so a standard Dirac mass term for neutrinos can not be defined. The Majorana formalism generates a coupling between a fermion field and its charge conjugate field for neutral fermions that comes from the equivalence of the fermion and antifermion. This coupling generates two mass terms, $m_L$ and $m_R$, one for both the left and right-handed states. The very small neutrino masses can then be explained by the Seesaw mechanism[34], a process that can generate very small masses for the neutrinos given that massive right-handed neutrinos exist in this case.

## 1.3 Neutrino Oscillation Experiments and the Measurement of Oscillation Parameters

The discovery of neutrino oscillations and the formalisation of the theory describing the mechanism meant that there were a new set of parameters that required measurement. Specialised neutrino oscillation experiments were devised in order to perform these measurements, making use of accelerator generated neutrino beams or antineutrinos from nuclear reactors.

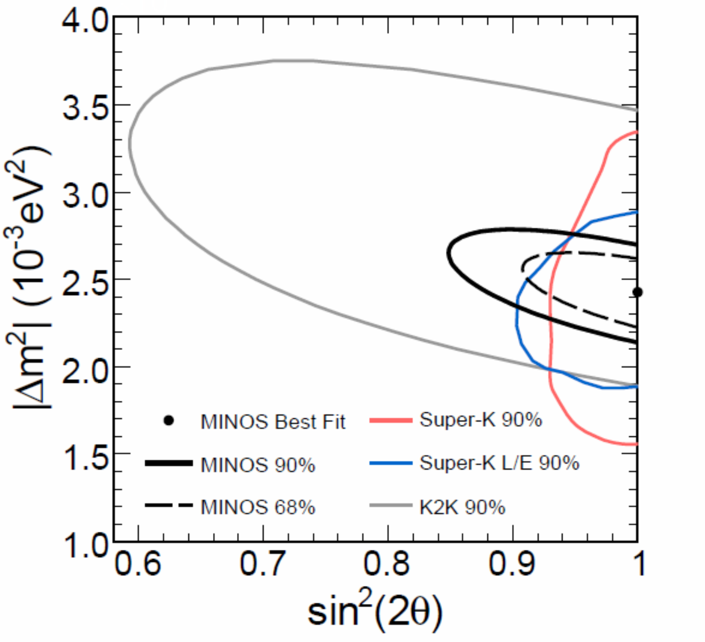

Figure 1.7: Results from MINOS, K2K and Super-K for the atmospheric neutrino mixing parameters showing $\Delta m^2_{32}$ plotted against $\sin^2(2\theta_{23})$. Figure taken from [36].

### 1.3.1 Neutrino Beam Experiments

Neutrino beam experiments use man-made beams of neutrinos to provide the flux for the experiments. The experiments considered all used beams of $\nu_\mu$ or $\bar{\nu_\mu}$ produced from decays of mesons that were in turn produced from firing protons onto a fixed target.

#### K2K

The Japanese KEK to Kamioka (K2K) experiment used a $\nu_\mu$ beam produced at KEK and used Super-K, 250 km away, as the far detector. The near detector suite, consisting of a smaller 1 kton water Čerenkov detector and a fine-grained detector system, was positioned 300 m downstream of the proton target. The experiment was designed to measure $\nu_\mu$ disappearance that enabled measurement of the atmospheric sector parameters $\Delta m^2_{32}$ and $\theta_{23}$. Figure 1.7 shows the K2K result compared to MINOS (see below) and Super-K. The K2K best fit point was found to be at [35]:

$$\Delta m^2_{23} = 2.8 \times 10^{-3}\,\mathrm{eV}^2 \quad \text{and} \quad \sin^2(2\theta_{23}) = 1.0$$

### MINOS

The Main Injector Neutrino Oscillation Search is a long baseline neutrino oscillation experiment based at Fermilab in the USA. It consists of the beamline at Fermilab, a 27 ton near detector 1.04 km from the target and a 4 kton far detector at a baseline of 735 km. Both detectors are magnetised tracking detectors with plastic scintillator as the active medium and steel planes as the target mass. The experiment uses a 93 % pure $\nu_\mu$ beam that can have its polarity reversed to produce a beam with an enhanced $\bar{\nu_\mu}$ component[37]. MINOS was designed to look for both $\nu_\mu$ disappearance and $\nu_e$ appearance, in contrast to the reactor experiments that search for $\bar{\nu}_e$ disappearance.

The $\nu_\mu$ disappearance probability gives sensitivity to the atmospheric neutrino mixing parameters $\Delta m^2_{23}$ and $\theta_{23}$. Figure 1.7 shows the MINOS results along with K2K and Super-K. The best fit point measured by MINOS is at [38]:

$$\Delta m^2_{32} = 2.32^{+0.12}_{-0.08} \times 10^{-3}\,\mathrm{eV}^2 \quad \text{and} \quad \sin^2(2\theta_{23}) > 0.94 \text{ at } 90\,\%$$

The MINOS results for $\nu_e$ appearance are shown compared to those from CHOOZ in Figure 1.8, plotted as $\delta$ against $2\sin^2(2\theta_{13})\sin^2\theta_{23}$. MINOS saw 54 events in the far detector compared to a prediction of $49.1 \pm 7.0(\text{stat}) \pm 2.7(\text{syst})$, corresponding to a $0.7\sigma$ significance of a non-zero $\theta_{13}$ [39].

MINOS switched to run in $\bar{\nu_\mu}$ mode and measured the atmospheric oscillation parameters using antineutrinos. Figure 1.9 shows a comparison of the results for the $\bar{\nu_\mu}$ and $\nu_\mu$ data taking periods. The best fit point was measured at [40]:

$$\Delta\bar{m}^2_{32} = 3.36^{+0.46}_{-0.40}(\text{stat}) \pm 0.06(\text{syst}) \times 10^{-3}\,\mathrm{eV}^2$$

$$\sin^2(2\bar{\theta}_{23}) = 0.86^{+0.11}_{-0.12}(\text{stat}) \pm 0.01(\text{syst})$$

Assuming that the same parameters described the oscillation of neutrinos and antineutrinos, the MINOS results give agreement at the 2 % level. Antineutrino running is currently ongoing to double the statistics available for a second analysis. If proven, a difference in the behaviour of $\nu_\mu$ and $\bar{\nu_\mu}$ would mean that CPT is violated as it implies that the particle and antiparticle have different masses.

### T2K

Tokai to Kamioka (T2K) is a long baseline neutrino oscillation experiment in Japan. It is the first neutrino experiment to use an off-axis beam where the muon neutrinos are directed at an angle of 2.5° away from the detectors. The beam is produced at

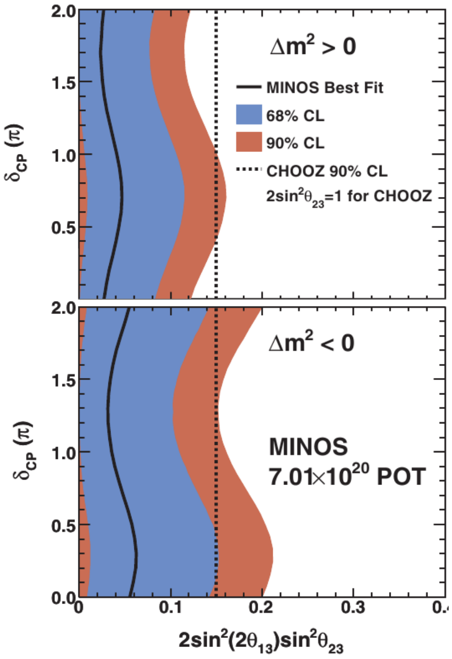

Figure 1.8: Results from MINOS and CHOOZ for $\delta$ and $2\sin^2(2\theta_{13})\sin^2\theta_{23}$ The CHOOZ limit is shown for $\Delta m^2_{32} = 2.43 \times 10^{-3}\,\mathrm{eV}^2$ and $\sin^2(2\theta_{23}) = 1.0$. The top and bottom plots show the normal and inverted hierarchies respectively[39].

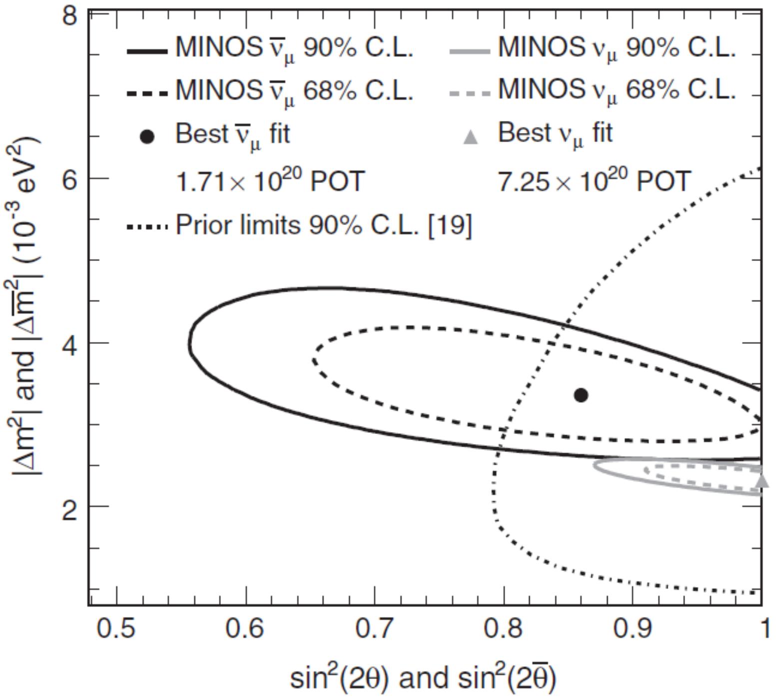

Figure 1.9: Results from MINOS, showing $\Delta\bar{m}^2_{32}$ plotted against $\sin^2(2\bar{\theta}_{23})$ for $\bar{\nu_\mu}$ disappearance compared to $\Delta m^2_{32}$ plotted against $\sin^2(2\theta_{23})$ for the MINOS $\nu_\mu$ run [40].

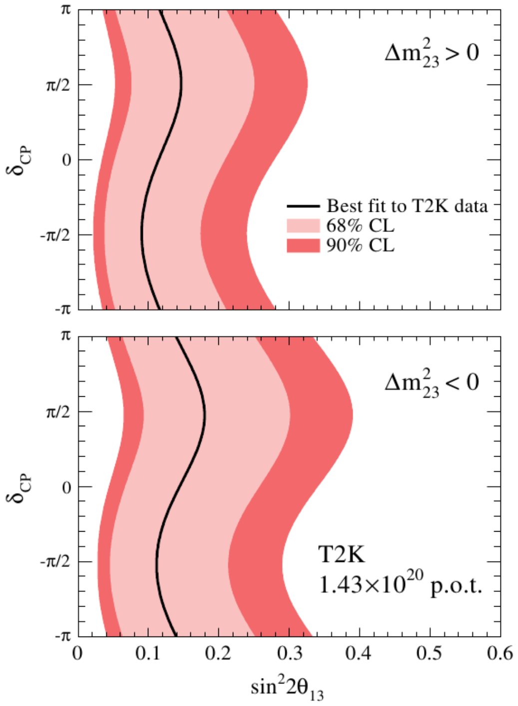

Figure 1.10: The confidence region in $\delta$ and $\theta_{13}$ as measured by T2K [41]. The top (bottom) shows the normal (inverted) hierarchy.

the J-PARC site in Tokai, on Japan's east coast. The neutrinos travel 295 km to the far detector, Super-K, passing through the near detector complex at 280 m. The T2K experiment is described in detail in Chapter 2.

The first results from T2K were published in 2011, with the indication of electron neutrino appearance in the muon neutrino beam, with a best fit point at $\sin^2 2\theta_{13} = 0.11$[41]. Figure 1.10 shows the allowed regions in $\delta$ and $\theta_{13}$. The result is incompatible with a value of $\sin^2 2\theta_{13} = 0$ at the $2.5\sigma$ level. Even though the significance is not high enough to be considered a discovery, this result provides a strong indication that $\theta_{13}$ is non-zero, and could even be quite large.

### NO$\nu$A

The NuMI Off-Axis $\nu_e$ Appearance experiment (NO$\nu$A) will be a long baseline experiment based at Fermilab, USA. The experiment will be the successor to MINOS and makes use of the same NuMI $\nu_\mu$ beam. The experiment will consist of two detectors, both consisting mostly of the same materials, to measure the neutrino beam at distances of 240 m and 810 km. The far detector will be a fully active 30 kton detector consisting of liquid scintillator filled cells arranged in perpendicular orienta-

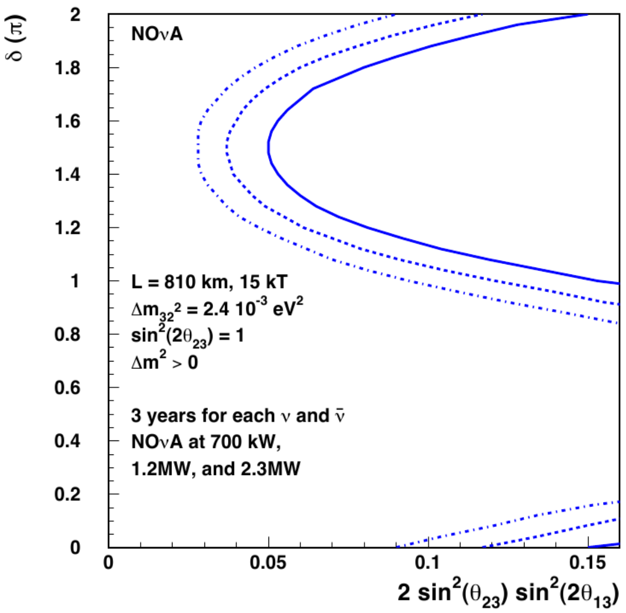

Figure 1.11: NO$\nu$A 95 % confidence level sensitivity for the mass ordering shown as a function of $2\sin^2\theta_{23}\sin^2 2\theta_{13}$ and $\delta$ for three years running at three different beam power values. The solid line corresponds to 700 kW, dashed line to 1.2 MW and the dotted line to 2.3 MW. Figure from [43].

tions to give a 3 dimensional readout. The near detector will be of the same design, with the addition of 10 cm thick iron plates between the cells in the downstream section[42]. The long baseline means that NO$\nu$A is sensitive to matter effects, meaning it is sensitive to the mass hierarchy. The 95 % confidence level resolution for the mass hierarchy is shown in Figure 1.11 as a function of $2\sin^2\theta_{23}\sin^2 2\theta_{13}$ and $\delta$ after three years of running for three different beam power scenarios. The plot shows that for any true value of $2\sin^2\theta_{23}\sin^2 2\theta_{13}$ and $\delta$ to the left of the curve then NOvA will determine the sign of $\Delta m^2_{32}$ at the 95 % confidence level. The far detector is expected to be complete by early 2014[43].

### 1.3.2 Reactor Experiments

Reactor experiments take advantage of the copious production of $\bar{\nu}_e$ from nuclear power stations. All of the reactor experiments used the same detection method as the Cowan and Reines experiment, measuring the $\bar{\nu}_e$ flux by the inverse beta decay process shown in Equation 1.2. The detection of photons from the positron annihilation and from the neutron capture within a small time window is the signature of a $\bar{\nu}_e$ interaction.

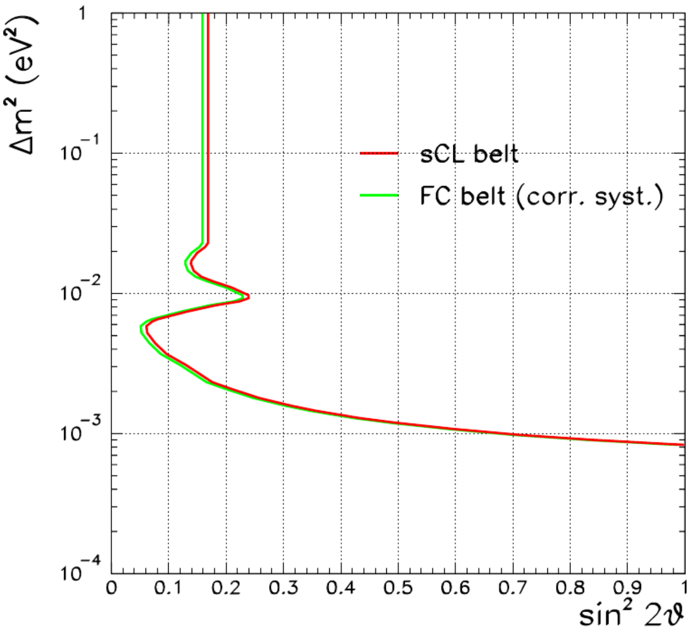

Figure 1.12: The CHOOZ result plotting $\Delta m^2_{32}$ against $\sin^2(2\theta_{13})$. The green line labelled as FC corresponds to the Feldman-Cousins consideration of the systematic errors. Plot taken from [17].

### CHOOZ

CHOOZ was an experiment in France that had a single liquid scintillator detector located 1 km from two nuclear reactor cores at the CHOOZ power station. The $\frac{L}{E} \sim 300\,\text{kmGeV}^{-1}$ value for CHOOZ was designed to be sensitive to the oscillations driven by $\Delta m^2_{32}$ and hence provide information about $\theta_{13}$. CHOOZ found, at the 90 % level, no evidence for oscillation of $\bar{\nu_e} \rightarrow \bar{\nu_x}$ [17], setting a limit on the $\Delta m^2_{32}$, $\sin^2(2\theta_{13})$ phase space shown in Figure 1.12.

### Palo Verde

Palo Verde was a similar experiment to CHOOZ, based in Arizona, USA. It used a liquid scintillator detector placed to detect neutrinos from three reactor cores at baselines of 750 m from one of the reactors and 890 m from the other two. Like CHOOZ, Palo Verde was built to be sensitive to oscillations driven by the atmospheric mass splitting. No evidence was seen for the oscillation of $\bar{\nu_e} \rightarrow \bar{\nu_x}$ and a limit was obtained on the parameter space that was slightly less stringent than the CHOOZ limit [18].

### KamLAND

The Kamioka Liquid scintillator Anti-Neutrino Detector (KamLAND) was built to measure the mixing angle $\theta_{12}$ and the mass splitting $\Delta m^2_{21}$ by measuring $\bar{\nu_e}$ from 55 nuclear power stations across Japan. The detector consisted of a 1 kton target of liquid scintillator placed in the cavern of the Kamiokande experiment. The power stations provided $\frac{L}{E}$ values ranging from 20 to 100 kmGeV$^{-1}$. The final results from KamLAND, considering reactor, solar and geo neutrinos, gave the following values for the solar sector parameters [44]:

$$\Delta m^2_{21} = 7.59 \pm 0.21 \times 10^{-5}\,\text{eV}^2 \quad \text{and} \quad \tan\theta_{12} = 0.47^{+0.06}_{-0.05}$$

### Double CHOOZ

The Double CHOOZ experiment re-uses the site of the original CHOOZ experiment at the CHOOZ nuclear reactor in France. The cavern that contained the CHOOZ detector was re-used to house the Double CHOOZ far detector at a distance of 1.05 km. Work has begun on constructing a second detector closer to the reactors that will act as the near detector at a distance of approximately 250 m, planned to be operational from early 2013 [45]. In 2011 Double CHOOZ began taking data with just the far detector and saw an indication of a non-zero $\theta_{13}$ [46]:

$$\sin^2 2\theta_{13} = 0.086 \pm 0.041(\text{stat}) \pm 0.030(\text{syst}) \tag{1.57}$$

The result excludes $\theta_{13} = 0$ at the 90 % level but is not significant enough to actually be a measurement of a non-zero $\theta_{13}$. Figure 1.13 shows the three sigma discovery potential assuming that $\Delta m^2_{32} = 2.5 \times 10^{-3}\,\text{eV}^2$.

### Daya Bay

Daya Bay is a reactor neutrino experiment in China. The $\bar{\nu_e}$ flux is provided by three pairs of reactor cores at Daya Bay, Ling Ao and Ling Ao II. The experiment uses a total of eight identical 20 ton liquid scintillator detectors, of which 6 are currently built, grouped in the following way: Two detectors are positioned at each of the two near detector sites and the remaining 4 detectors form the far detector. The Daya Bay near detector has a 363 m baseline to the Daya Bay cores and the Ling Ao near detector has baselines of 481 m and 526 m from the Ling Ao and Ling Ao II sites respectively. The far detector is positioned with a baseline of 1985 m from the Daya Bay cores and 1615 m from Ling Ao and Ling Ao II.

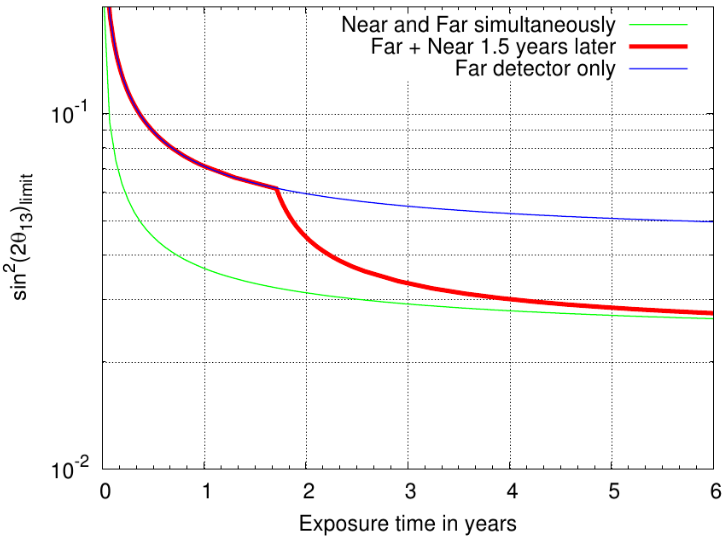

Figure 1.13: The three sigma discovery potential of Double CHOOZ plotted as a function of number of years of running where $\Delta m^2_{32} = 2.5 \times 10^{-3}\,\text{eV}^2$ [47].

In March 2012, results were published from Daya Bay from the first 55 days of data taking with a measurement of $\theta_{13}$ with a significance greater than $5\sigma$[48]:

$$\sin^2 2\theta_{13} = 0.092 \pm 0.016(\text{stat}) \pm 0.005(\text{syst}) \tag{1.58}$$

The measurement used a rate-only analysis but the spectrum of events is shown with the best fit oscillation curve in Figure 1.14 showing good agreement with the data. The measurement shows that the value of $\theta_{13}$ is relatively large, and in agreement with the lower accuracy measurements from T2K and Double CHOOZ.

### RENO

The Reactor Experiment for Neutrino Oscillations (RENO) is based in South Korea, at the Yonggwang nuclear power station. The power station consists of 6 separate reactor cores positioned in a linear configuration that provide the $\bar{\nu}_e$ flux for the experiment. The experiment has two identical 16 ton liquid scintillator detectors, positioned at distances of 290 m and 1380 m from the centre of the reactor line respectively [49].

RENO began data taking in August 2011 and released a measurement of $\theta_{13}$ in April 2012[50] using a rate only analysis. The energy spectrum of the events detected at the near and far detectors over a period of 229 days is shown in Figure 1.15 and shows a clear deficit of events in the peak region. The bottom plot in the

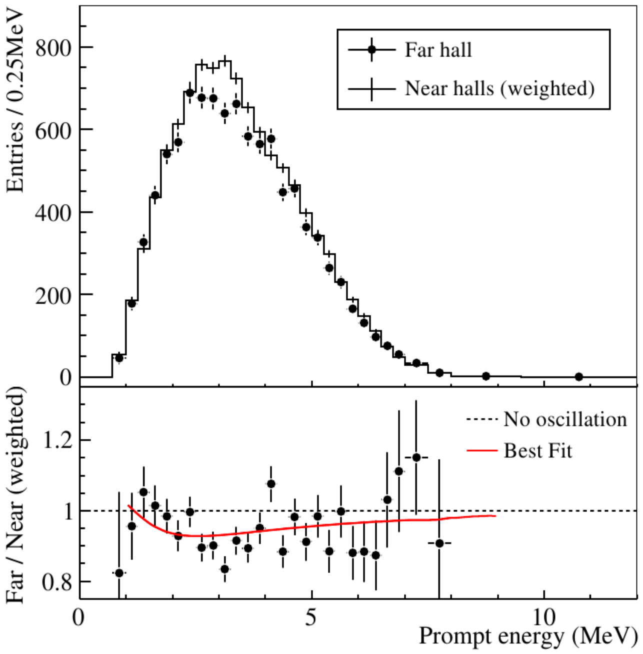

Figure 1.14: The Daya Bay $\bar{\nu}_e$ energy spectrum (top) and the ratio of events in the near and far detectors as a function of energy (bottom). The red line in the bottom plot shows the best fit oscillation curve. Figure from [48].

figure shows the near-far ratio as a function of distance. The best fit to the data gave a measurement of

$$\sin^2 2\theta_{13} = 0.103 \pm 0.013(\text{stat}) \pm 0.011(\text{syst}) \tag{1.59}$$

in good agreement with the Daya Bay measurement.

### 1.3.3 Anomalies in Neutrino Oscillation Measurements

The results from the experiments discussed in sections 1.3.2 and 1.3.1 are all consistant within the uncertainties quoted. However, there have been some results that do not appear to fit into the Standard Model neutrino oscillation framework.

#### LSND

The Liquid Scintillator Neutrino Detector (LSND) was an experiment in Los Alamos, USA, that was searching for $\bar{\nu}_e$ appearance in a $\bar{\nu}_\mu$ beam. The 167 ton detector was placed just 30 m upstream of the neutrino target, with an average neutrino energy of approximately 50 MeV. It was also able to change the beam polarity to look for $\nu_\mu \rightarrow \nu_e$ oscillations.

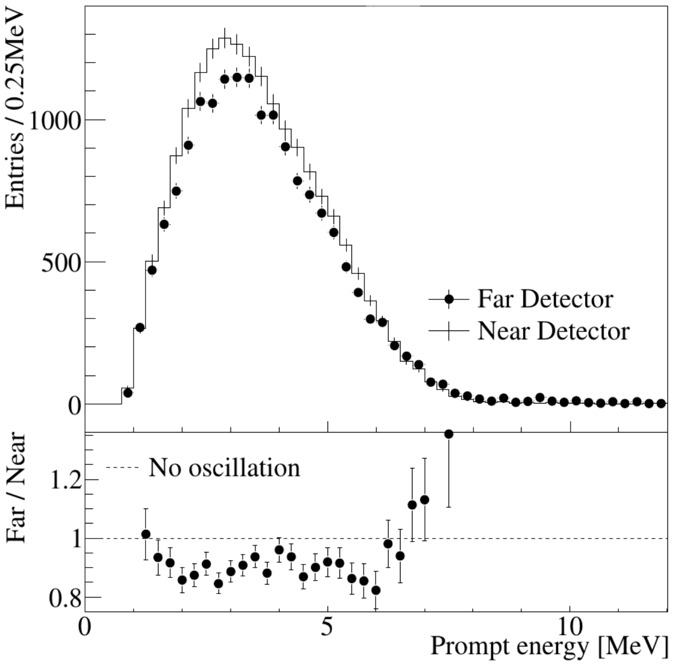

Figure 1.15: The measured energy spectra in the RENO near and far detectors after 229 days of running (top) and the ratio of the far detector and near detector energy spectra (bottom). Figure adapted from [50].

In antineutrino running, an excess of $51.0^{+20.2}_{-19.5}$ $\bar{\nu_e}$ events was seen [51]. The interpretation of this result as an oscillation is shown by the filled regions in Figure 1.16, with the $\Delta m^2$ value inconsistent with world average $\Delta m^2_{32}$ by at least two orders of magnitude.

In neutrino mode, 40 $\nu_e$ interactions were measured with a background expectation of $21.9 \pm 2.1$ events, providing a result consistent with the antineutrino result [52].

### MiniBooNE

MiniBooNE was built to measure potential $\nu_\mu \rightarrow \nu_e$ oscillations at a similar $\frac{L}{E}$ value to LSND. It began taking data from the Fermilab Booster $\nu_\mu$ beam at Fermilab before switching polarity to take $\bar{\nu_\mu}$ data. The beam has an average energy of approximately 800 MeV and directs the neutrinos at the MiniBooNE detector placed 581 m upstream of the beryllium proton target. The fully active target consists of 818 tons of mineral oil that produces both Čerenkov and scintillation light, collected by an array of Photomultiplier Tubes (PMTs) positioned around the target volume.

The result from the $\nu_\mu$ data is shown in Figure 1.17, ruling out the allowed

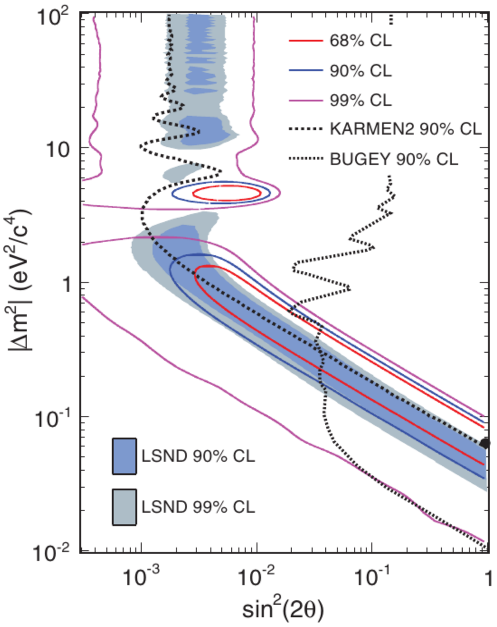

Figure 1.16: A comparison of the MiniBooNE $\bar{\nu_\mu} \rightarrow \bar{\nu_e}$ result to those from LSND, KARMEN2 and BUGEY for a two neutrino $\bar{\nu_\mu} \rightarrow \bar{\nu_e}$ oscillation model. [53].

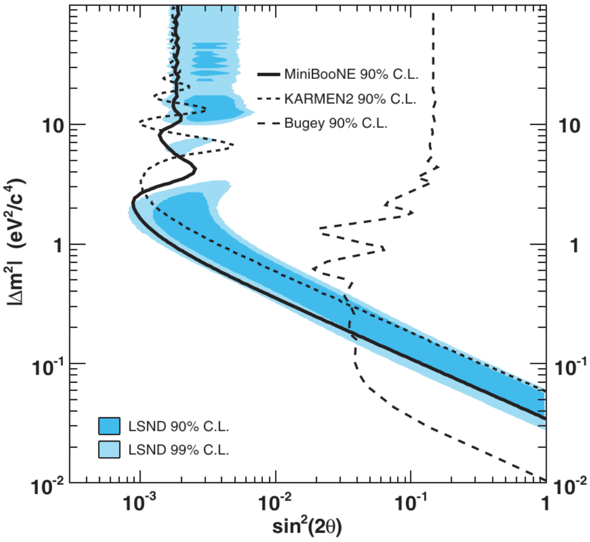

Figure 1.17: A comparison of the MiniBooNE $\nu_\mu \rightarrow \nu_e$ result for $E_{\nu_\mu} > 475\,\text{MeV}$ for a two neutrino oscillation model compared to those from LSND, KARMEN2 and BUGEY for a $\bar{\nu_\mu} \rightarrow \bar{\nu_e}$ model[54].

region from LSND at the 90 % level. The energy of the events considered in the analysis was $E_{\nu_\mu} > 475\,\mathrm{MeV}$. However, in the energy range from 200 MeV to 475 MeV an excess of $128.8 \pm 20.4 \pm 38.3$ events was seen[55]. This low energy excess is currently unexplained.

An excess of events was also seen in the $\bar{\nu_\mu}$ data. In the energy range 475 MeV to 1250 MeV, an excess of $20.9 \pm 14.0$ events were seen[53]. Figure 1.16 shows the results compared to LSND, giving good agreement with the results from LSND for $\Delta m^2 < 10\,\mathrm{eV}^2$.

### Summary

Figure 1.16 shows that the $\bar{\nu_\mu} \rightarrow \bar{\nu_e}$ results from LSND and MiniBooNE give a mass splitting in the range of $0.1\,\mathrm{eV}^2$ to $1\,\mathrm{eV}^2$. This is inconsistent, by approximately two orders of magnitude, with the measured mass splittings from the solar and atmospheric sectors, meaning that they do not fit with the Standard Model neutrino oscillations. In order to reconcile these results with the other neutrino oscillation results sterile neutrinos and CP violation are required. In addition, since the re-calculation of the reactor antineutrino fluxes there is an unexplained deficit of events in short baseline reactor experiments, consistent with results from LSND and MiniBooNE [56].

Sterile neutrinos would allow for further mass splitting terms on the scale required by the LSND oscillations that would have a very small effect on other oscillations due to the large difference in the optimal $\frac{L}{E}$ values. These extra neutrinos must be sterile because there is no evidence for the existence of additional neutrinos from weak interactions. The current status of sterile neutrino searches is not presented here but is discussed in detail in [57].

## 1.4 Summary of Neutrino Oscillation Parameters

The values of the neutrino oscillation parameters have been measured by a series of experiments as described in Section 1.3. Table 1.1 summarises the values of the three mixing angles and the two common mass-splittings.

| Parameter | Value |
|---|---|
| $\sin^2 2\theta_{12}$ | $0.861^{+0.026}_{-0.022}$ |
| $\sin^2 2\theta_{23}$ | $> 0.92$ |
| $\sin^2 2\theta_{13}$ | $0.098 \pm 0.013$ |
| $\lvert\Delta m^2_{32}\rvert$ | $2.43 \pm 0.13 \times 10^{-3}\,\mathrm{eV}^2$ |
| $\Delta m^2_{21}$ | $7.59^{+0.20}_{-0.21} \times 10^{-5}\,\mathrm{eV}^2$ |

Table 1.1: Summary of neutrino oscillation parameters. All values taken from [29].

# Chapter 2

# The T2K Experiment

## 2.1 Motivation and Overview

The T2K experiment [58] is a long baseline neutrino oscillation experiment in Japan. The $\nu_\mu$ beam is created at J-PARC in Tokai on the east coast and travels 295 km across the country to the far detector, Super-Kamiokande. Figure 2.1 gives a graphical overview of the experiment, showing the positions of the near detector (ND280) and Super-K.

T2K was built in order to provide detailed measurements of neutrino oscillation parameters to improve on the results from first generation neutrino oscillation experiments such as K2K. The primary goal of T2K is to perform a measurement of the unknown mixing parameter $\theta_{13}$, but the experiment is also capable of performing accurate measurements of the atmospheric sector oscillation parameters $\Delta m^2_{32}$ and $\theta_{23}$. Initial results from T2K[41] and Double CHOOZ[46] give an indication that $\theta_{13}$ could be quite large, which were recently confirmed by Daya Bay[48] and RENO[50]. There is still the need for T2K to perform a measurement of $\theta_{13}$ from a neutrino appearance measurement, and with the relatively large value of $\theta_{13}$ there

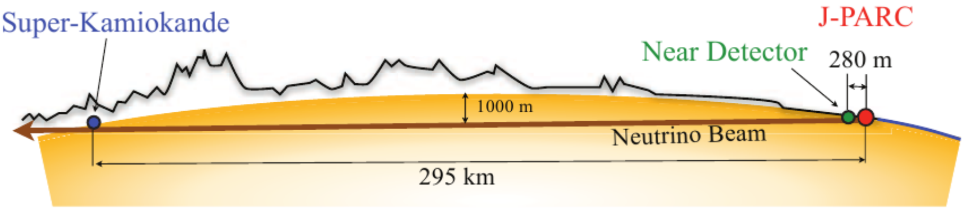

Figure 2.1: A simple schematic diagram of the T2K experiment showing the beam passing from J-PARC, through the near detector and on to Super-Kamiokande. Distances are not shown to scale. Figure from [58].

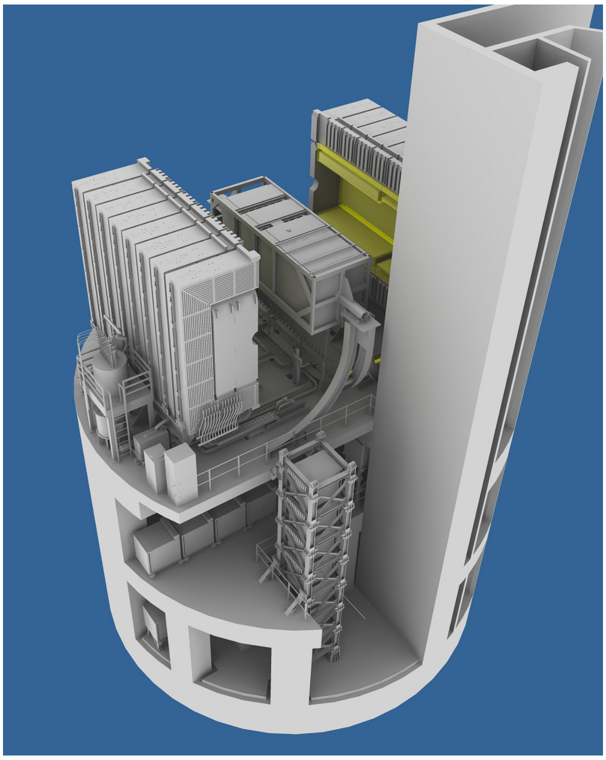

Figure 2.2: An engineering figure showing the entire near detector pit. The vertical and horizontal collections of modules in the bottom part of the figure make up INGRID and the top floor shows the ND280 with the magnet open. The beam centre passes through the centre of INGRID, where the vertical and horizontal parts of the cross meet. The large vertical structure on the right is the housing of the lift shaft.

is a possibility of measuring $\delta$.

T2K is the first long baseline beam experiment to place the detectors in an off-axis position. The baseline of 295 km and peak energy of approximately 0.6 GeV maximise the oscillation probability according to Equation 1.42 for $\Delta m^2 = \Delta m^2_{32} = 2.5 \times 10^{-3}\,\mathrm{eV}^2$. The near detector complex also contains an on-axis detector called the Interactive Neutrino Grid (INGRID). The relative positions of INGRID and ND280 are shown in Figure 2.2, with INGRID in the foreground making up the cross shape, and the ND280 on the upper floor with the magnet in the open position.

## 2.2 J-PARC Complex

The accelerator complex is located at J-PARC, Tokai, on the east coast of Japan. Figure 2.3 shows the main components of the J-PARC site: the LINAC, 3 GeV

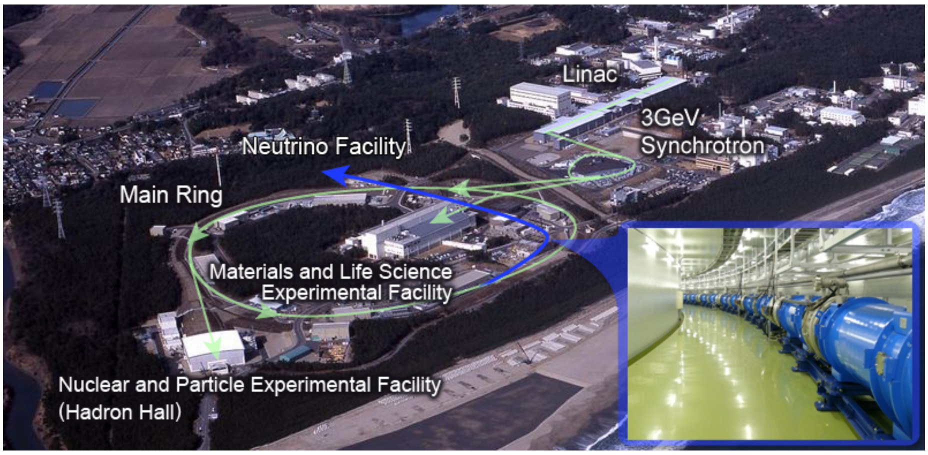

Figure 2.3: An aerial view of the J-PARC site showing the locations of the LINAC, 3 GeV Synchrotron, 30 GeV Main Ring and the ND280 (neutrino) facility. The inset image shows the primary beamline that directs the protons from the main ring to the T2K target.

synchrotron (RCS), 30 GeV main ring synchrotron (MR) and the neutrino beamline.

The first stage in the accelerator is the $H^-$ LINAC. It accelerates the $H^-$ ions to 181 MeV (the energy will be upgraded to 400 MeV in 2013) before passing them into charge-stripping foils that convert the beam into a proton beam. The protons are passed into the RCS where they are accelerated up to energies of 3 GeV. Approximately 5 % of the protons are passed from the RCS into the MR, with the rest passed into the Materials and Life Science area. Protons circulate the MR in 8 bunches (or 6 bunches in the first running period) of $1.2 \times 10^{13}$ protons with a repetition rate of $\sim 0.3$ Hz and reach energies of 30 GeV. The bunches are approximately 50 ns wide with the total spill of 8 bunches covering a time of about 5 $\mu$s. The beam power is designed to be approximately 0.75 MW. Figure 2.4 shows that the MR is shared with a number of other experiments that are housed in the hadron facility of J-PARC and are not associated with the T2K project.

### 2.2.1 Neutrino Beamline

The 30 GeV protons are fast extracted from the MR and bent tightly inside the ring into the neutrino beamline, as shown in Figure 2.4. The fast extraction process involves the extraction of all eight proton bunches within a single cycle of the MR. The neutrino beamline consists of two sections, the primary and secondary beamlines. The primary beamline starts with the kicker magnets used to extract the proton beam from the MR. The beam is bent round the tight arc section by a series of combined function superconducting magnets and passed through a series

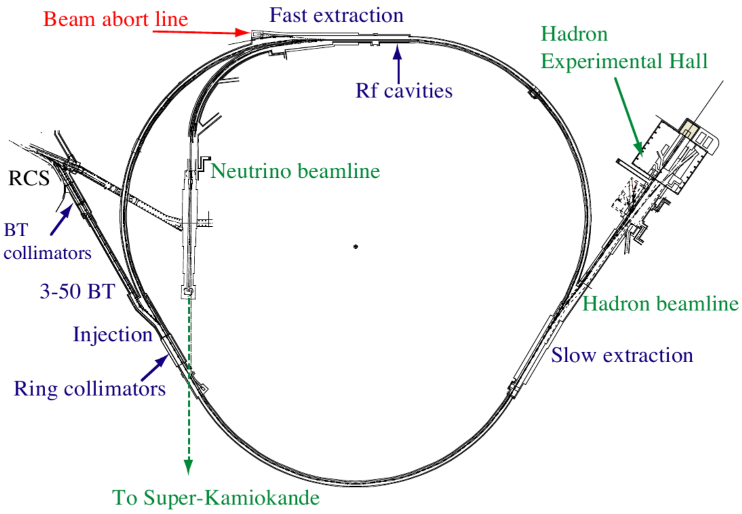

Figure 2.4: A schematic diagram of the MR and Neutrino Beamline.

of monitors to check the beam profile and other properties. The magnets are known as combined function magnets because they both steer and focus the proton beam. The proton beam then passes through a graphite baffle with a 30 mm beam hole to remove the beam halo before colliding with the graphite target. The beam halo refers to the small number of protons on the edge of the beam that can escape and induce radioactivity in the components of the accelerator. The baffle is therefore used to protect the target region from radiation damage. The target is 91.4 cm long, 2.6 cm in diameter, has a density of 1.8 gcm$^{-3}$ and is housed within the first magnetic horn. The low density of the target helps to protect it from the high temperatures, expected to reach up to 700°C, generated by the protons incident on the target. Figure 2.5 shows the total number of protons on target (POT) delivered by the MR over the 2010-2011 run period. The beam power steadily increased during the two running periods and reached 145 kW before the 2011 Japan Earthquake.

The secondary beamline, shown in Figure 2.6, starts with the three magnetic focusing horns used to focus the positively charged mesons from the proton-target collision into the 96 m decay pipe. The three horns run with an operating current of about 250 kA. The mesons travel along the decay pipe until they decay to produce neutrinos. Some negative mesons that are highly boosted along the beam direction will not be removed by the magnetic horns, causing a contamination of antineutrinos in the beamline. Muon neutrinos are mostly produced by the following meson decays:

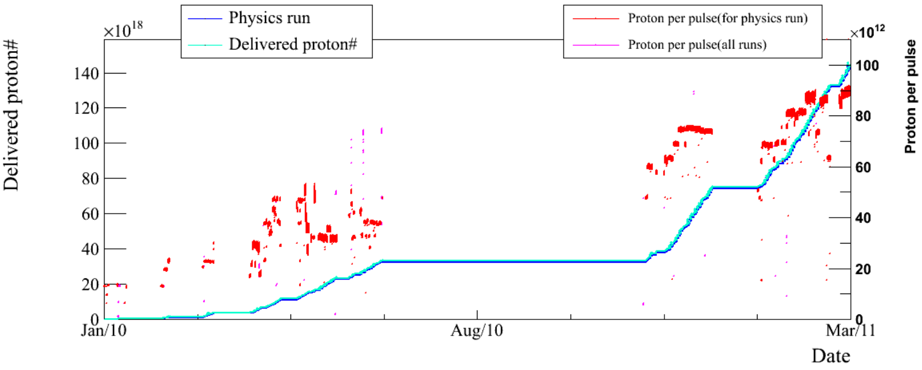

Figure 2.5: The integrated number of protons on target (POT) delivered by the accelerator from January 2010 until the shutdown caused by the major earthquake in March 2011. The flat region in the centre of the plot corresponds to the summer shutdown period. Figure from [59].

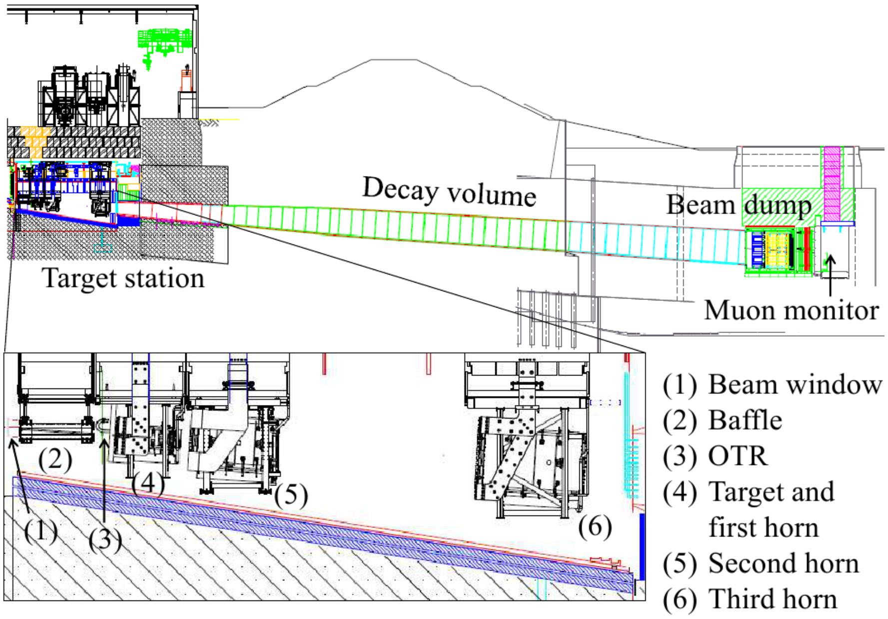

Figure 2.6: A diagram showing the components of the secondary beamline with a zoomed in view of the target station. Figure from [58]

$$\pi^+ \rightarrow \mu^+ \nu_\mu \tag{2.1}$$

$$K^+ \rightarrow \mu^+ \nu_\mu \tag{2.2}$$

and electron neutrinos by

$$K^+ \rightarrow e^+ \nu_e \pi^0 \tag{2.3}$$

$$K_L^0 \rightarrow e^+ \nu_e \pi^- \tag{2.4}$$

$$\mu^+ \rightarrow e^+ \nu_e \bar{\nu_\mu} \tag{2.5}$$

The charge conjugates of these processes, while suppressed by the focusing of positive mesons, occur to produce the corresponding antineutrinos. Figure 2.7 shows the relative fluxes of the different neutrinos and antineutrinos seen at Super-K from the beam simulation. The antineutrinos have approximately 10% of the flux of their corresponding neutrino and the $\nu_e$ component of the beam is approximately 1%. The decaying muons shown in Equation 2.5 are not produced in the proton-target collisions but in processes such as those given in Equations 2.1 and 2.2. The beam dump, positioned downstream of the decay pipe, 109 m from the target, consists of 2.4 m of iron and 3.17 m of graphite in thickness. It was designed to stop all particles other than neutrinos and muons with momenta greater than 5.0 GeV/c. These high energy muons pass into the muon monitor, a detector used to measure the beam intensity and direction. The neutrinos pass through the muon monitor and travel inland towards INGRID, ND280 and Super-K.

### Neutrino Flux Simulation

The neutrino flux simulation is very important as it provides the base neutrino flux used to generate the simulations for all of the detectors, as shown for the Super-K flux in Figure 2.7. The flux simulation models the interaction of the proton beam with the graphite target, and predicts the spectrum of neutrinos coming from the decay of the mesons created in the interactions. The simulation uses GEANT[60] to model the entire secondary beamline and the 30 GeV proton-graphite interactions are modelled by FLUKA[61]. The cross-sections controlling the production of pions and kaons in the target were tuned using measurements from the NA61/SHINE[62] experiment at CERN. NA61/SHINE had a dedicated run where a 30 GeV beam of protons was fired onto a replica T2K graphite target to measure the meson production cross-sections for the proton momentum used in the T2K beam. In phase space regions not covered by NA61/SHINE for kaon production, additional data

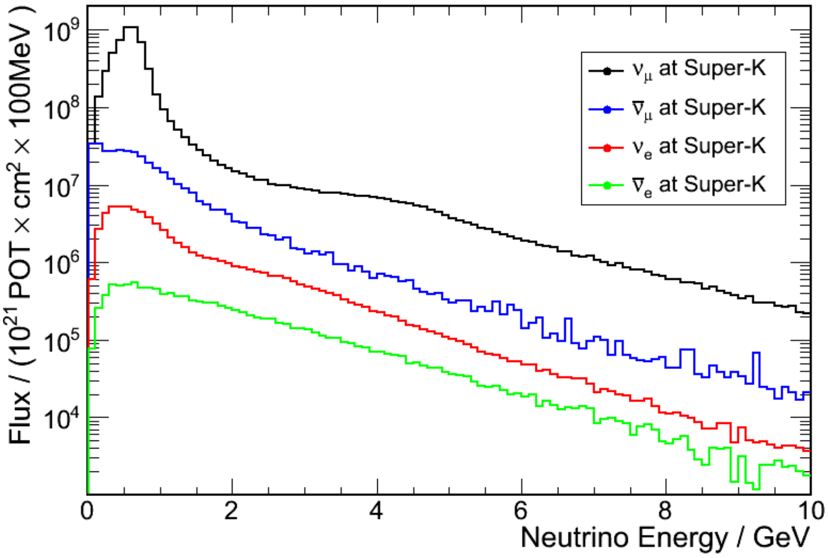

Figure 2.7: The predicted neutrino flux from simulation at Super-K broken down by (anti)neutrino type.

from proton-beryllium experiments in the 1970s (Allaby et al[63] and Eichten et al[64]) were used to tune the cross-section values.

### 2.2.2 Off-Axis Beam

The neutrino beam points in a direction approximately 2.5° away from Super-K and the ND280, as shown in Figure 2.8, though the ND280 presents a much larger solid angle than Super-K. The neutrino energy $E_\nu$ can be calculated by considering the two body kinematics of meson decays such as those shown in Equations 2.1 and 2.2:

$$E_\nu = \frac{m_M^2 - m_\mu^2}{2\left(E_M - p_M \cos\theta\right)} \tag{2.6}$$

where the $M$ subscript refers to the parent meson. The angle $\theta$ is the angle between the pion and the neutrino in the lab frame and approximates the off-axis angle. Figure 2.9 shows the energy of neutrinos from pion parents as a function of the pion energy for four different values of the angle $\theta$. As the off-axis angle increases the neutrino energy becomes increasingly mono-energetic, meaning that the energy spectrum of the neutrinos is narrow compared to an on-axis beam. This is advantageous to a neutrino oscillation experiment because the oscillations are dependent on the $\frac{L}{E}$ value and to maximise the probability of oscillations the neutrino energy needs

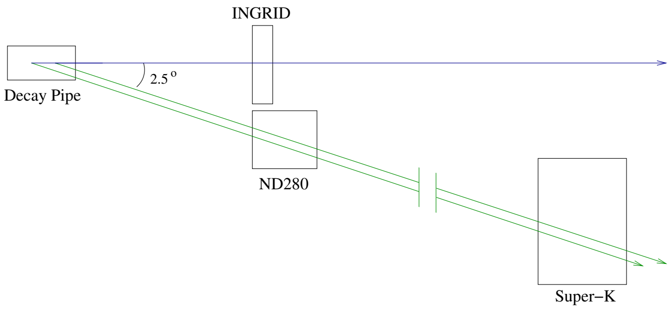

Figure 2.8: Schematic showing the relative positions of the three detectors with the ND280 and Super-K at 2.5° off-axis. The sizes of the detectors are not shown to scale and the ND280 subtends a considerably larger solid angle than Super-K.

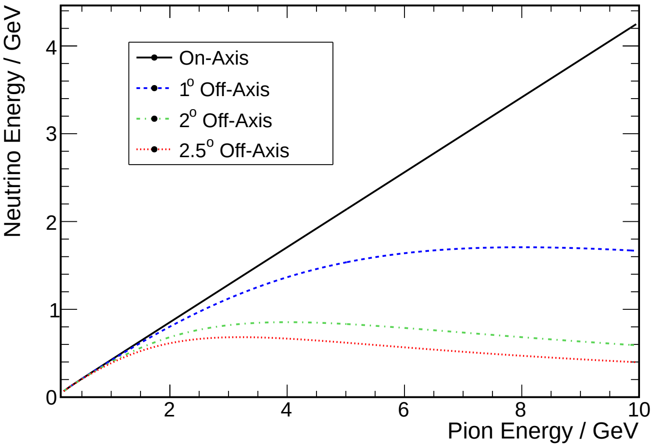

Figure 2.9: The neutrino energy plotted as a function of the parent pion energy for an on-axis configuration and three different off-axis angles.

to be matched to the baseline. It also removes the high energy tail that can cause backgrounds to the oscillation measurements through DIS interactions. Finally, it also means that the neutrino energy is less dependent on the hadronic modelling that predicts the pion energy, but it means that there is a greater dependence on the pion angle. The primary disadvantage of an off-axis configuration is that the flux decreases with off-axis angle, meaning the choice of off-axis angle is a balance between narrowing the energy distribution and maintaining a reasonable event rate.

## 2.3 The INGRID Detector

INGRID is an on-axis monitoring detector in the near detector complex. It has the primary goal of measuring the beam direction to a precision of better than 1 mrad.

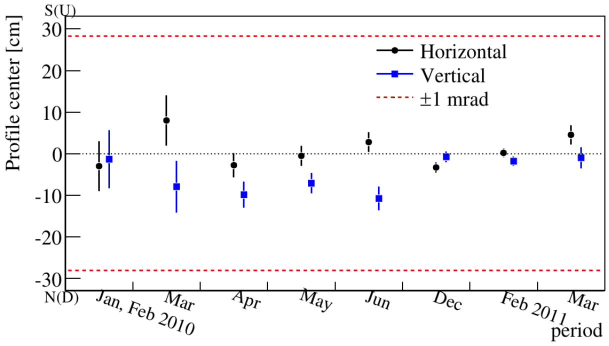

Figure 2.10: A plot showing the centre position of the beam at INGRID from January 2010 until March 2011. The dashed lines show the region allowed by the design requirements of an uncertainty of ±1 mrad in the beam direction. Figure from [65].

At the 0.75 MW design power of T2K there will be enough neutrino interactions to make this measurement every day. This is a very important measurement because even a small change in off-axis angle changes the neutrino energy distribution at ND280 and Super-K. For example, using Equation 2.6, a change of 1 mrad away from the nominal value of the off-axis angle $\theta$ for a neutrino produced by a 2 GeV pion changes the neutrino energy by ±1.3 %. Figure 2.10 shows the beam position measured by INGRID for all current running periods, where the dashed lines correspond to the beam stability requirement of ±1 mrad accuracy of the beam direction, showing that the beam was stable within the design requirements over the entire running period.

INGRID consists of 16 identical target modules and a single proton module. Figure 2.11 shows the positioning of the modules with 7 modules forming each of the horizontal and vertical branches. The two other target modules are placed away from the main cross shape. The proton module is positioned in the centre of the cross, in between the vertical and horizontal components.

The target modules contain 11 pairs of scintillator tracking planes where each pair has an X and a Y plane. X and Y are the horizontal and vertical directions perpendicular to the beam direction Z. Each scintillator plane is made from 24 scintillator bars that are 5 cm × 1 cm × 1.2 m in dimension. The tracking planes are separated by 6.5 cm layers of iron providing a total of 116 tons of target material for neutrino interactions. The modules have 3 or 4 veto planes depending on whether they are adjacent to another module as adjacent modules share a veto plane. The veto planes cover the top, bottom, left and right sides of the modules and consist of 22 scintillator bars. The structure of the modules is shown in Figure 2.12.

Figure 2.13 shows the proton module, a pure scintillator module containing

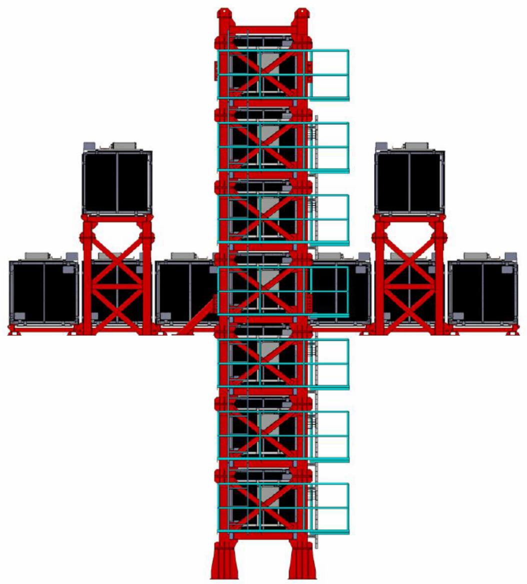

Figure 2.11: The layout of the INGRID detector looking downstream. Figure from [58].

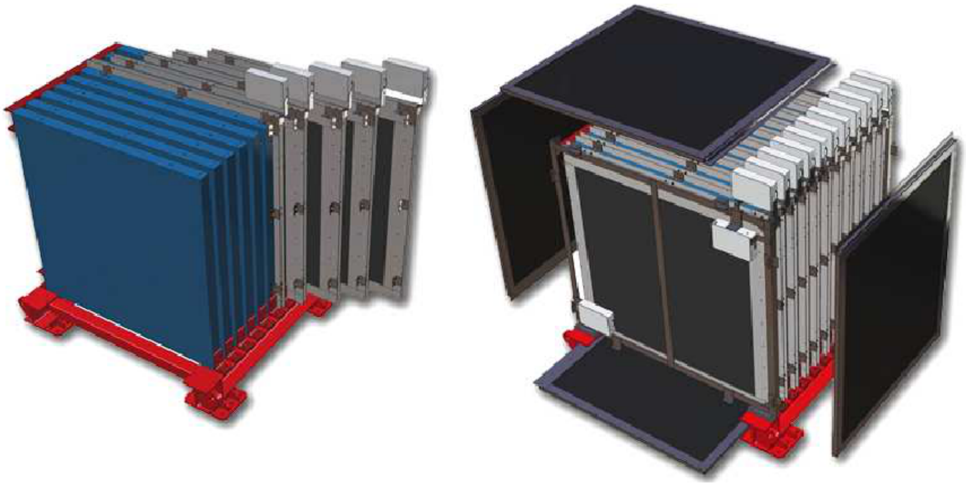

Figure 2.12: A figure showing one of the INGRID modules with (right) and without (left) the veto planes. Figure from [58].

Figure 2.13: An exploded figure of the INGRID proton module. Figure from [58].

no iron planes. The proton module was added in order to specifically study CCQE events. The standard target modules are not able to distinguish CCQE events from other CC events because they can only track the muon as the proton stops in the thick iron planes. It has 17 pairs of X-Y tracking planes that have a different composition to those in the target modules. There are 16 scintillator bars with a smaller cross-section of 2.5 cm × 1.3 cm used in the central region with 8 bars identical to those in the target modules on either side of the central region. The smaller bars in the central region are used to help to resolve the proton tracks.

## 2.4 The ND280

The ND280 is the T2K off-axis near detector and is located 280 m downstream of the target. It is positioned at approximately the same off-axis angle as Super-K, as shown in Figure 2.8. The main purpose of the ND280 is to provide measurements of the unoscillated neutrino flux, including making a measurement of the $\nu_e$ component of the beam. In addition, ND280 will also be used for neutrino interaction cross-section measurements on water, carbon, lead and brass. The uncertainties in the flux and process cross-sections are major sources of uncertainty to the oscillation measurements at Super-K meaning that the ND280 can be used to greatly reduce the systematic uncertainties in the oscillation analyses.

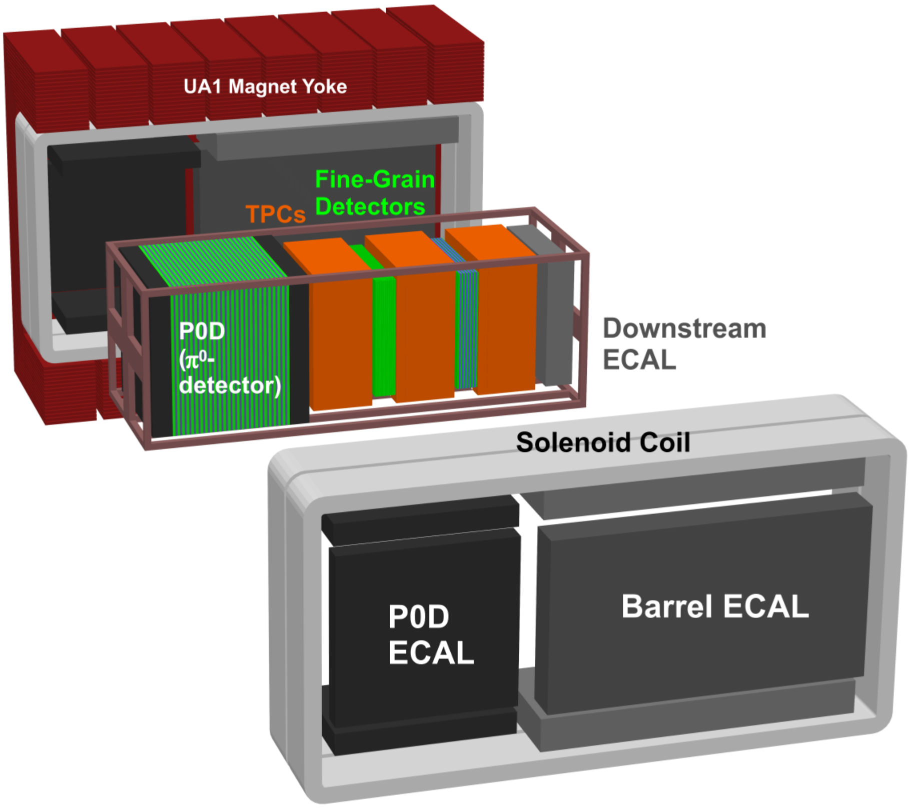

Figure 2.14: An exploded view of the ND280 showing all of the subdetectors apart from the SMRD, with the beam travelling from left to right.

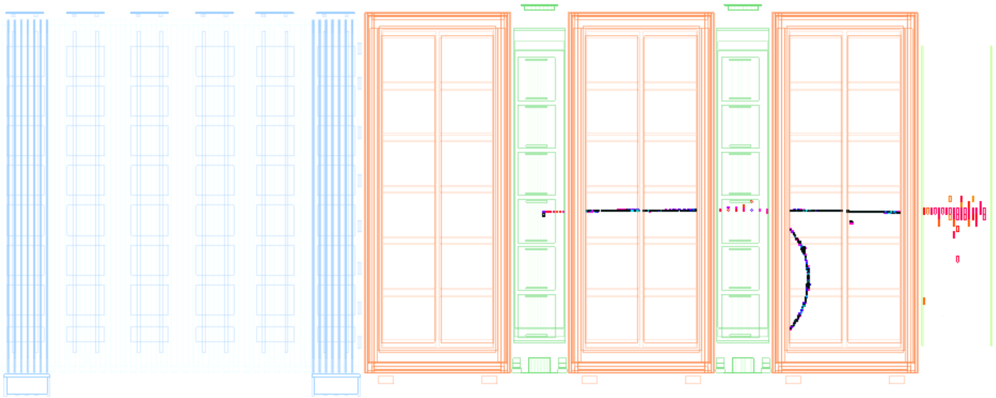

Figure 2.15: An example of a CCQE $\nu_e$ interaction in FGD1. The electron passes through TPCs 2 and 3, interacting in FGD2, before showering in the DsECal. The highly curved track in TPC3 is a scattered electron produced in the interaction in FGD2.

The ND280 is a hybrid detector formed from five main subdetectors, as shown in Figure 2.14. The most upstream of the subdetectors is the Pi-zero Detector (P0D) that is located in the basket region. The region immediately downstream of the P0D is the tracker region consisting of the three Time Projection Chambers (TPCs 1, 2 and 3) and the two Fine-Grained Detectors (FGDs 1 and 2). The Downstream Electromagnetic Calorimeter (DsECal) is the most downstream subdetector, located behind the tracker region. The two other sets of ECal modules surround the basket region; the Barrel ECal surrounds the tracker region and the P0D ECal surrounds the P0D. The detectors are enclosed in the re-conditioned UA1/NOMAD magnet from CERN. The magnet runs with a current of 2.9kA producing a magnetic field of 0.2 T that allows for the measurement of particle momenta. The spaces between the return yokes are instrumented to form the Side Muon Range Detector (SMRD). An example of a CCQE $\nu_e$ event in the ND280 is shown in Figure 2.15 where the electron is created in the neutrino interaction in FGD1 and travels through TPC2, FGD2 and TPC3 before showering in the DsECal. It also undergoes an interaction in FGD2 that produces two particles, one of which stops in FGD2 and the other can be seen in TPC3 as a low momentum track.

### 2.4.1 Optical Readout

The P0D, FGDs, ECals and SMRD are all plastic scintillator based detectors and use the same wavelength shifting fibres and optical sensors. The fibres used are 1 mm diameter Y-11 wavelength shifting (WLS) fibres manufactured by Kuraray[1]. The WLS fibres absorb the blue light emitted from the plastic scintillator and emit green light to be detected by the optical sensors. Avalanche photodiodes called Multi-Pixel Photon Counters (MPPCs) produced by Hamamatsu[2] were chosen as the ND280 photosensor.

#### MPPC

The MPPCs consist of an array of 667 avalanche photo-diodes called pixels that are operated at a voltage greater than the breakdown voltage. The pixels are connected in parallel and are isolated from neighbouring pixels to minimise the probability that a photon detection in one pixel would also trigger the neighbouring pixels. The MPPCs used in the ND280 were developed for T2K, based on a commercially available Hamamatsu model. The customised model includes a larger sensitive area of $1.3\times1.3\,\text{mm}^2$, matched to maximise the light acceptance from the Y-11 wavelength

---

[1] Kuraray CO. LTD. Tokyo 100-8115, Japan

[2] Hamamatsu Photonics K.K. Hamamatsu City 430-8587, Japan

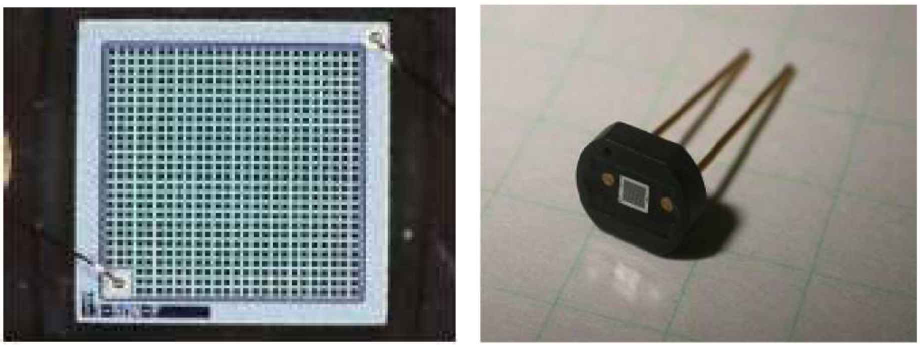

Figure 2.16: A magnified view of the face of an MPPC (left) and the entire MPPC device (right). Figure from [58].

shifting fibres. In addition, the sensitive region for the MPPCs is well matched to the emission spectra from the Y-11 fibres. The MPPCs were chosen because they met the photo-detector requirements for ND280 [66]:

- Equal or better photon detection efficiency than a multi-anode PMT.
- Compact size to fit within the limited space of the magnet.
- Operate within a 0.2 T magnetic field.
- Good stability and relatively low cost for a large number of channels.

The MPPCs run in Geiger mode meaning that the applied voltage is greater than the breakdown voltage of the device, typically by approximately 1 V. A photon incident on the active area produces an avalanche of electrons, with a gain of the order $10^6$.

Figure 2.17 shows an MPPC and the components of the connector for use in the ECals. The connector was primarily required to ensure a good coupling between the MPPC and the WLS fibre. The foam spring provides an elastic force to lightly press the MPPC onto the fibre. The MPPC and foam spring are placed inside the clip, a component designed to clip onto the plastic ferrule that was glued onto the end of the WLS fibre. The printed circuit board provides the mounting point for a micro coaxial cable that provides both the power to the MPPC and the readout channel. The shroud encloses the entire assembly and provides a fixing point to screw the component onto the ECal bulkhead. The other ND280 subdetectors have different methods for housing the MPPCs.

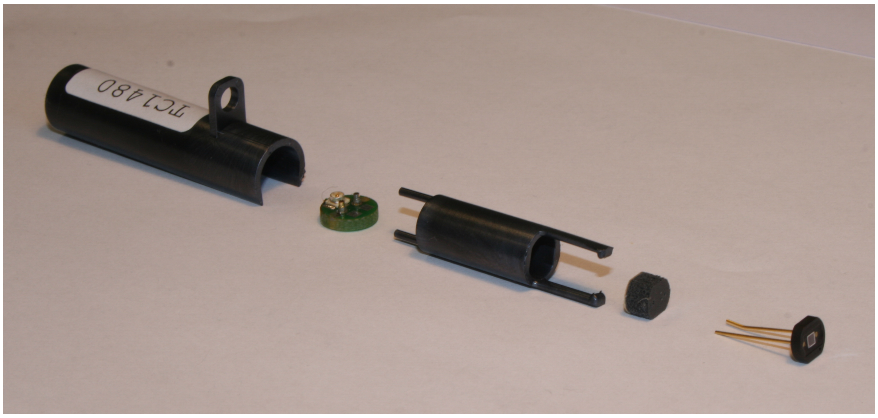

Figure 2.17: A photograph of an MPPC complete with components for installing it in the ECal modules. From right to left: MPPC, foam spring, clip, printed circuit board and shroud.

### 2.4.2 The P0D

The P0D was designed with the primary physics goal of measuring neutral current $\pi^0$ events in a water target. Neutral current single $\pi^0$ events form a major background for the $\nu_e$ appearance search at Super-K. The neutral current production of single $\pi^0$ mesons is very poorly understood in the sensitivity region of T2K, and hence must be measured and understood to provide an accurate background prediction for the $\nu_e$ appearance measurement at Super-K.

The P0D is formed from four sections named Super-P0Dules. Figure 2.18 shows the four Super-P0Dules with the two smaller electromagnetic calorimetry modules either side of the two water target modules. The water provides the oxygen target required to measure the NC $\pi^0$ cross-section on the same target material as Super-K and the scintillator planes provide the particle tracking. The P0D uses $TiO_2$ coated plastic scintillator bars with a triangular cross section with a 32.5 mm base and height of 17 mm. In total, the P0D provides approximately 15 tons of target mass.

The Super-P0Dules are made from a series of P0Dules. Each P0Dule consists of two scintillator tracking planes, one with vertical bars and one with horizontal bars. The planes consist of 134 vertical bars of 2200 mm or 126 horizontal bars of 2268 mm depending on orientation, all read out on a single end using a wavelength shifting fibre coupled to an MPPC. The P0Dules in the calorimetry Super-P0Dules are separated by a 4 mm layer of stainless steel clad lead and those in the water target Super-P0Dules are sandwiched between 1.5 mm sheets of brass. The lead and brass layers provide the material to induce photon showers in the detector and

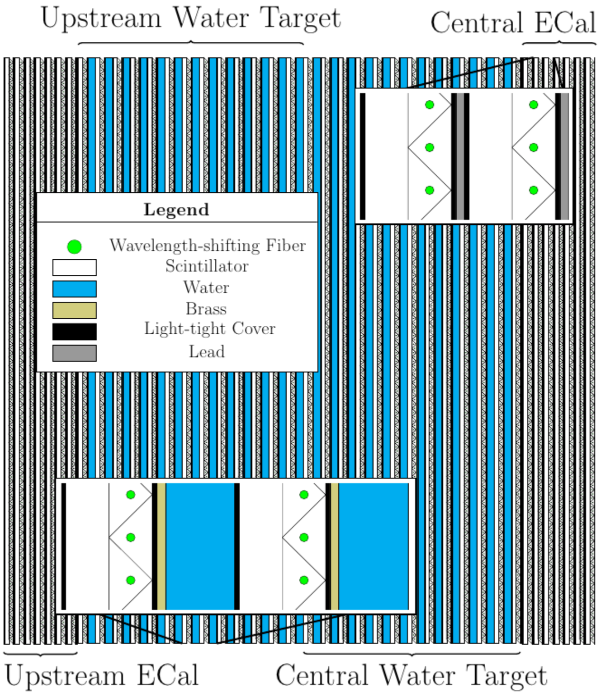

Figure 2.18: A detailed schematic of the P0D showing the relative positions of the four Super-P0Dules with zoomed in images showing the P0Dule construction. Figure from [58].

hence allows photons to be reconstructed.

### 2.4.3 The Tracker

The two FGDs and three TPCs, collectively known as the tracker, occupy the basket region downstream of the P0D. The primary physics goal of the tracker is to measure CCQE events from both $\nu_\mu$ and $\nu_e$ interactions. The design of the tracker region is a compromise between the need for sufficient target mass to produce large event rates and the need to keep the target mass small so as to make an accurate measurement of particle momenta in the TPCs.

#### The FGDs

The two FGD modules provide both the target mass within the tracker region and detailed particle tracking to distinguish the nucleons from the outgoing lepton from neutrino interactions. The FGDs are constructed from $TiO_2$ coated plastic scintillator bars $9.6 \times 9.6\,\mathrm{mm}^2$ in cross-section and 1843 mm in length, each threaded with a wavelength shifting optical fibre. The optical fibre is read out by an MPPC on one end and is mirrored on the other end to maximise the light collected by the sensor.

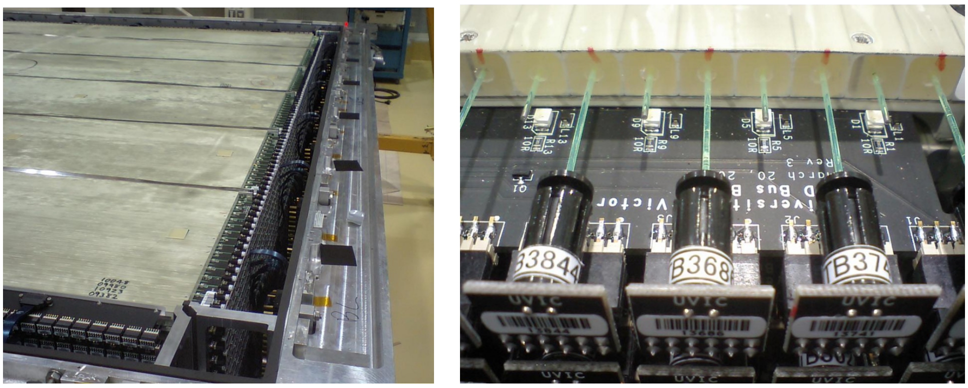

Figure 2.19: Left: FGD1 during construction. Right: A zoomed in view of the MPPCs coupled to the wavelength shifting fibres. Photographs taken from [67].

Within a single layer the fibres are read out on alternating ends, as shown in the right of Figure 2.19.

The two FGD modules are not identical. FGD1, shown in the construction phase in Figure 2.19, consists of 30 layers of 192 scintillator bars, with each layer alternating between the X and Y directions perpendicular to the beam. FGD2 consists of 14 layers grouped into 7 X-Y pairs that are separated by six 2.5 cm thick water targets. The absolute dimensions of the two FGDs are identical, allowing for the direct comparison of interactions on carbon and oxygen in FGDs 1 and 2 respectively. The FGDs each provide approximately 1 tonne of target material meaning the event rate is considerably lower than in the P0D. A simple particle identification is performed in the FGDs using range and energy loss ($\frac{dE}{dx}$) to distinguish protons from other particles.

Figure 2.20 shows the time of interaction vertices in the FGD for the first running period. The six bunches of the MR can be seen clearly with very few events occurring outside the beam windows.

### The TPCs

The three TPCs provide precision particle tracking for charged particles. The large volume of the TPCs enables the momentum of the particles to be measured using the curvature of the particle trajectory due to the magnetic field. The TPCs are three identical modules, each with a 3000 l volume filled mostly with gaseous argon to give high levels of ionisation from the movement of the charged particles. Figure 2.21 shows the design of the TPC. Ionisation electrons move in the electric field from their creation point on the particle track to the Micromega read-out on the

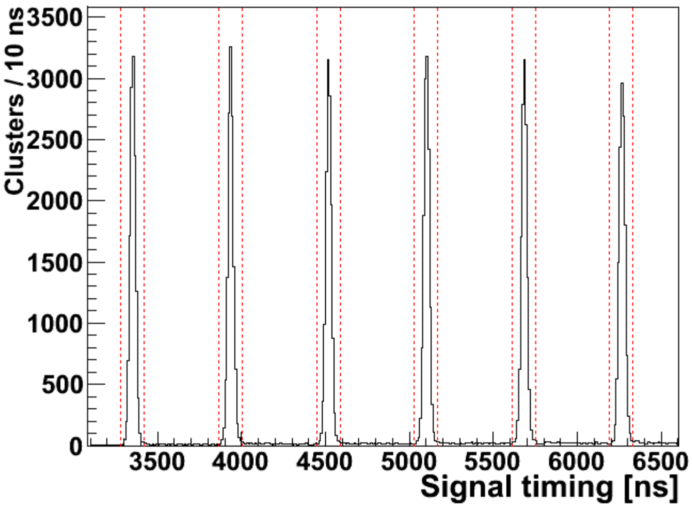

Figure 2.20: The time of interaction vertices in the FGD during Run 1 clearly showing the 6 proton bunches. The dashed lines show the ± 70 ns regions from the expected time. Figure from [68].

edge containing the front end cards.

Tracking in 3D is achieved in the TPC by using time to measure the position in the drift direction. The time of the hits in the TPC are compared to those in the FGDs and ECals in order calculate the drift distance. The other two coordinates are measured directly by the location of the drift electron on the Micromega readout pads. The amount of ionisation and the momentum of the track allow for precise measurement of the energy loss, a powerful tool for particle identification. Figure 2.22 shows the variation of the energy loss as a function of particle momentum for data and the prediction from the Bethe-Bloch function and the differences between the particles allows for electrons and protons to be distinguished from muons and pions.

### 2.4.4 The ECals

The ECals surround the basket region on all but the upstream side. All 13 ECal modules use the same detector technology consisting of $40 \times 10\,\mathrm{mm}^2$ plastic scintillator bars threaded with wavelength shifting fibres. The read out of all of the fibres is performed by MPPCs. The modules all contain lead layers to provide the target material for electrons and photons to shower.

Table 2.1 provides details on the number of layers in each module and the number and size of scintillator bars within the layers. The view refers to the coordinates measured by each layer; the first letter is the coordinate measured by the bar

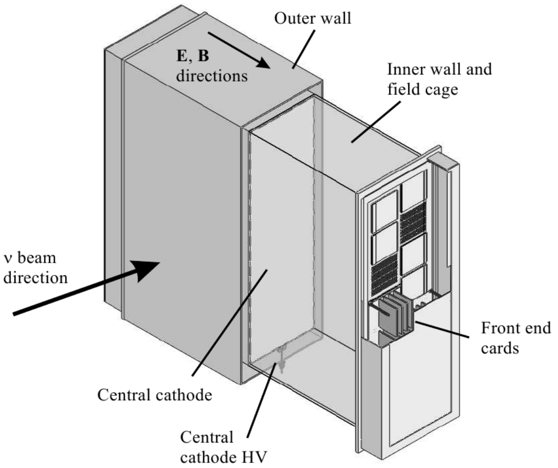

Figure 2.21: A schematic diagram of one of the TPCs. Figure from [58].

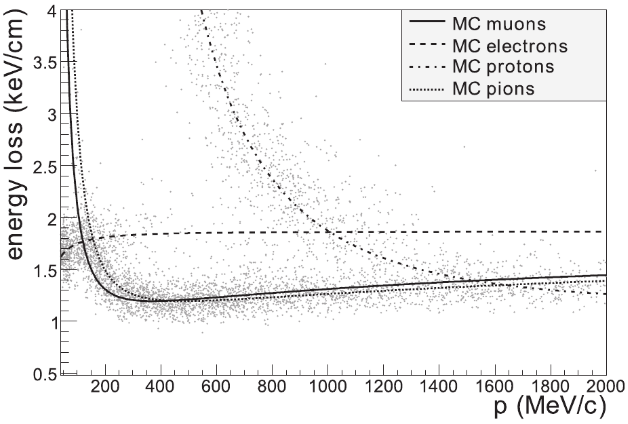

Figure 2.22: The measured energy loss for particles in the first T2K data run. The curves show the prediction from the Bethe-Bloch formula for four particle types. Figure from [58].

| ECal Module | View | Layers | Bars / Layer | Bar Length / m |
|---|---|---|---|---|
| DsECal | XZ | 17 | 50 | 2.00 |
| | YZ | 17 | 50 | 2.00 |
| Barrel Side | YX | 15 | 57 | 3.84 |
| | ZX | 16 | 96 | 2.28 |
| Barrel Top/Bottom | XY | 15 | 38 | 3.84 |
| | ZY | 16 | 96 | 1.52 |
| P0D Side | YX | 6 | 69 | 2.34 |
| P0D Top/Bottom | XY | 6 | 38 | 2.34 |

Table 2.1: A summary of the scintillator bar details for the different ECal modules including the number of bars per layer and the length of the bars.

and the second is the coordinate measured by the layer. For example, in the DsECal the Z coordinate depends on which layer is hit whereas the X and Y positions depend on which scintillator bars are hit.

The DsECal consists of 34 layers of scintillator bars in alternating XZ and YZ layers separated by a 1.75 mm layer of lead. All of the fibres are read out on both ends allowing for first position estimates based on time and charge information. The DsECal also forms part of the ND280 cosmic trigger.

The Barrel ECal consists of 6 modules, each with 31 layers. Figure 2.14 shows that there are two large side modules and four smaller top/bottom modules. The fibres in the 3.84 m bars are read out on both ends but the shorter fibres are mirrored on one end, and read out on the other. As with the DsECal, the scintillator layers are separated by a 1.75 mm layer of lead.

The DsECal and Barrel ECals form the Tracker ECal. The main goal of the Tracker ECal is to aid the Tracker in the full reconstruction of neutrino interactions in the FGDs. It is also very important in measuring electron energies from beam $\nu_e$ interactions since momentum measurement in the TPC becomes more difficult at higher energies due to very low curvature of the tracks. Measurement of neutral clusters will allow for $\pi^0$ searches in the tracker region, using the ECals to reconstruct the two decay photons, providing a complimentary measurement to the P0D.

The P0D ECal also has 6 modules: 2 side modules and 4 top/bottom modules. All modules consist of 6 layers, each separated by a 4 mm layer of lead. The lead layers are thicker than in the larger ECal modules in order to try to contain the photon showers. The fibres all have single ended read out with the other end mirrored. The P0D ECal is designed to detect muons and photons that escape from the P0D. This is especially important when the particle directions are perpendicular

Figure 2.23: Top left: The scanner used to check for fibres damaged in the insertion process. Top Right: All MPPCs connected to the fibres and mounted on the bulkhead. Bottom Left: Connection of the coaxial cables from the MPPCs to the front-end electronics. Bottom Right: The finished P0DECal left side module.

to the beam line since the P0D can not reconstruct particles in this view. It also provides additional calorimetry information for photon showers that are not fully contained in the P0D. Figure 2.23 shows a series of photographs from the P0DECal left side module construction at the University of Warwick.

### 2.4.5 The SMRD

The SMRD is designed to aid in the momentum and angle measurements of muons from CCQE interactions. It also helps establish backgrounds caused by neutrino interactions in the magnet and forms the majority of the ND280 cosmic trigger. Figure 2.24 shows some of the SMRD modules in position between the magnet return yokes with their associated electronic readout boards.

There are 8 sets of SMRD modules along the length of the magnet. The modules consist of 3 layers apart from the three most downstream vertical layers that have 4, 6 and 6 layers respectively. The increased number of layers are in the region where the muon flux from the tracker is greatest. Each horizontal layer consists of 4 scintillator bars that are 875 mm long, 167 mm wide and 7 mm in height.

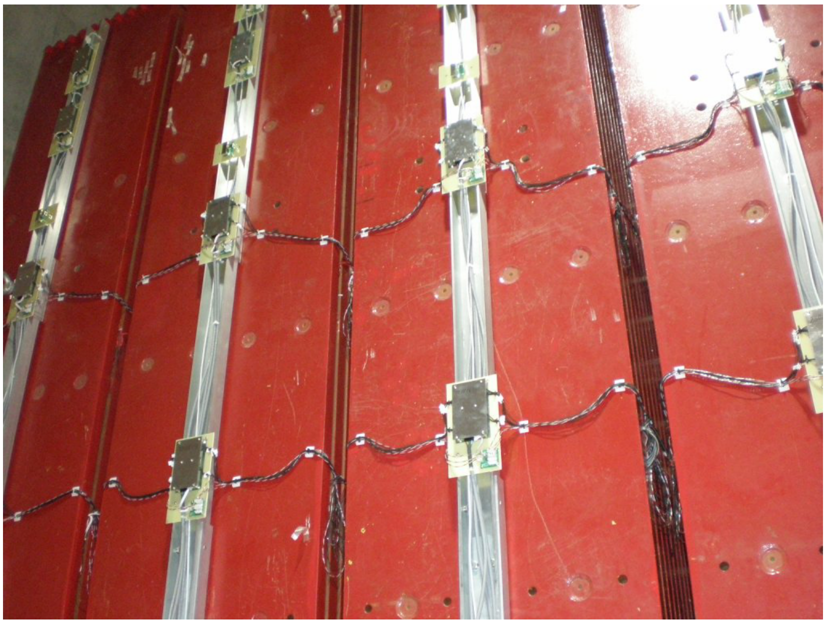

Figure 2.24: A photograph of some SMRD modules positioned between the magnet return yokes. The readout boards can be seen positioned with each of the modules. Photograph taken from [67].

Vertical layers are formed from 5 scintillator bars that are 875 mm by 175 mm by 7 mm.

The scintillator bars have a curved etched groove on one surface that is used to house a wavelength shifting fibre, as shown in Figure 2.25. The fibre is 255 cm long and is read out on both ends by MPPCs to maximise the signal size and to provide some information about where the hit occurred along the fibre.

## 2.5 Super-Kamiokande

Super-Kamiokande [69] is a 50 kton (22.5 kton fiducial mass) water Čerenkov detector located in a mine 1 km underneath Mt Ikeno, near Kamioka, Japan. It was built for a range of physics reasons, including the search for proton decay and for the study of neutrinos from various sources. Super-K has been a very successful detector, helping to solve the solar neutrino problem and the atmospheric neutrino anomaly, and also acted as the far detector for K2K. It is 295 km from the target at J-PARC and lies at an off-axis angle of about 2.5° to the neutrino beam. Charged particles travelling with a velocity above the Čerenkov threshold produce light as they propagate through the pure water and the light is collected by an array of approximately 13,000 PMTs. The detector has been running since 1996 through

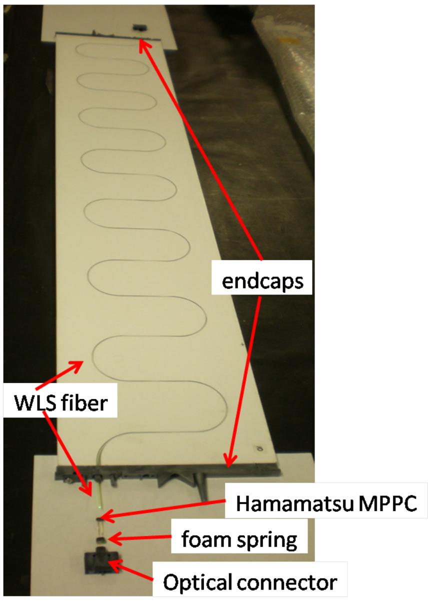

Figure 2.25: A photograph of an SMRD bar and associated readout components. Figure from [58].

four running periods, with the fourth period ongoing.

Super-K started taking data from the T2K beam in January 2010, recording all information within a 1 ms window around the GPS time stamp from the T2K spill time. Figure 2.26 shows the timing of events taken during the T2K trigger. The left plot shows the event time and the 8 (or 6) bunches of the beam are clearly visible. The plot on the right shows the same information as a residual from the expected time.

The water is held in a 41 m tall stainless steel tank that is 39 m in diameter. Approximately $2-2.5$ m from the tank wall is an inner stainless steel framework that acts as the mounting point for the PMTs. The inner surface is covered by 11,129 hemispherical Hamamatsu PMTs that are 50 cm in diameter and the outer surface contains a sparse array of 1,885 20 cm Hamamatsu PMTs. The two sets of detectors are independent and optically separated and are named the Inner Detector (ID) and Outer Detector (OD) respectively. A schematic diagram of Super-K showing both the ID and OD is shown in Figure 2.27. The ID forms the main part of the detector where the neutrino interactions used for analysis occur and the OD is used to veto incoming charged particles from the surrounding rock and cosmic rays.

The flavour of neutrino interactions at Super-K is measured by considering the leptons arising from the interactions. Muons and electrons behave differently in the water, with muons having minimal interactions and the electrons undergoing

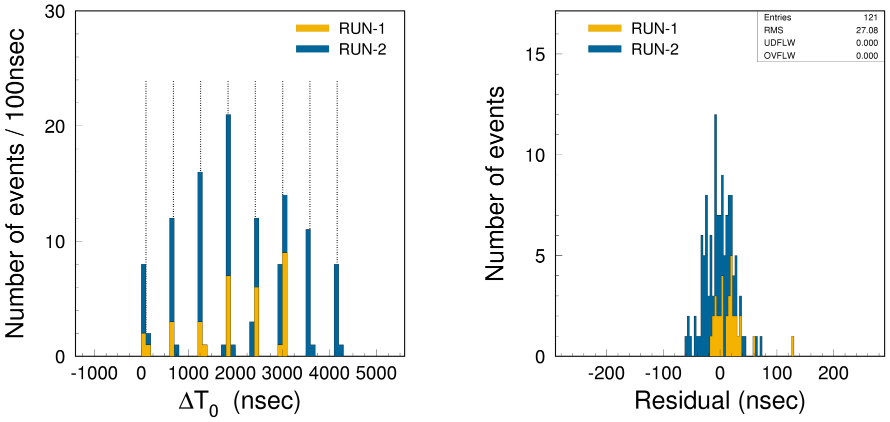

Figure 2.26: The time of events from the T2K beam (left) and plotted as a residual (right). Figures from [59].

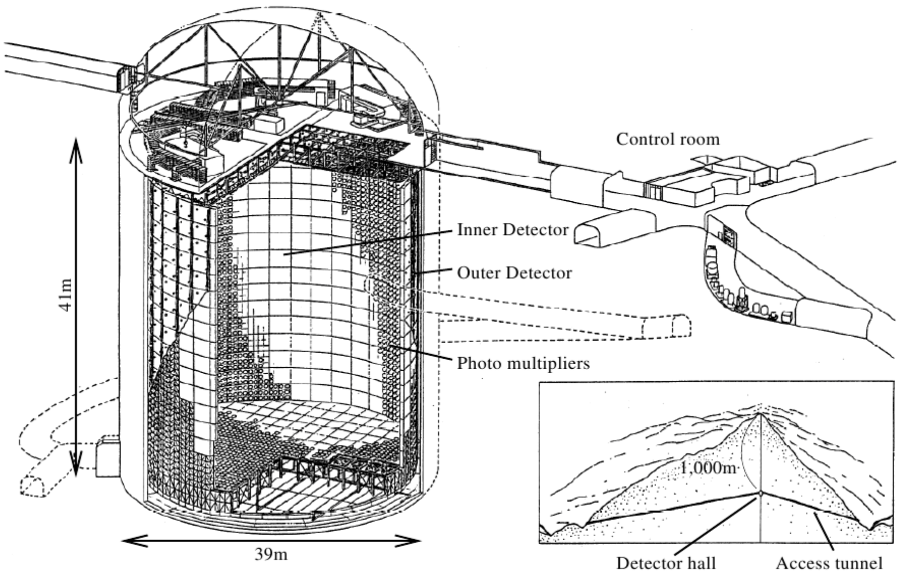

Figure 2.27: A schematic diagram of Super-K from [28].

multiple scatters and producing showers. The difference in behaviour means that the muon Čerenkov light rings are sharp, whereas the electron rings are more fuzzy. Figure 2.28 shows an example of the difference in the ring patterns from interactions from the T2K beam, showing the muon ring at the top and the electron ring at the bottom. Neutral pions can be detected by looking for two electron-like rings caused by the two decay photons and then calculating the invariant mass of the system.

Super-K does not have a magnetic field meaning that it is not able to measure the charge of the particles. It is the charge of the lepton in CC (anti)neutrino interactions that determines whether an event was caused by a neutrino or an antineutrino. This means that Super-K can not distinguish between interactions from neutrinos and antineutrinos.

## 2.6 Current Results and Physics Reach

In Summer 2011 the first results from the electron neutrino appearance search were published, providing an indication of a non-zero $\sin^2 2\theta_{13}$ as described previously in section 1.3.1. This measurement was the first indication of a non-zero and relatively large value of $\sin^2 2\theta_{13}$.

Figure 2.29 shows the 90 % confidence limit sensitivity of T2K to $\sin^2 2\theta_{13}$ plotted as a function of $\Delta m^2_{23}$ after 5 years of running at 0.75MW beam power. Three different systematic uncertainty scenarios are shown ranging from 5 % to 20 %. Taking $\Delta m^2_{23} = 2.5 \times 10^{-3}\,\text{eV}^2$ gives a 90 % confidence limit sensitivity of $6 \times 10^{-3} \leq \sin^2 2\theta_{13} \leq 8 \times 10^{-3}$ depending on systematic uncertainties.

Recent results from T2K[41], Double CHOOZ[46], Daya Bay[48] and RENO[50] show that $\theta_{13}$ is relatively large. With these measurements of $\sin^2 2\theta_{13}$, the neutrino physics field will begin to focus on the measurement of the CP violating phase $\delta$.

The left plot in Figure 1.5 shows the difference in oscillation probability for T2K between neutrinos and antineutrinos plotted as an asymmetry as a function of $\delta$. For certain values of $\delta$ the asymmetry is approximately 25 % and hence it could be measurable in the future. Acquiring equal amounts of data in both neutrino and antineutrino mode is not trivial because of the beam production mechanism and the lower cross-sections for antineutrinos. A proton incident on a carbon target has a net positive charge, meaning there is a positive bias to the mesons produced and positive mesons decay to produce neutrinos. Antineutrinos are produced in the decay of negative mesons which are produced in lower quantities. An antineutrino run would need to be approximately four times as long as a neutrino run to acquire the same statistics, due to the lower flux and lower interaction cross-sections.

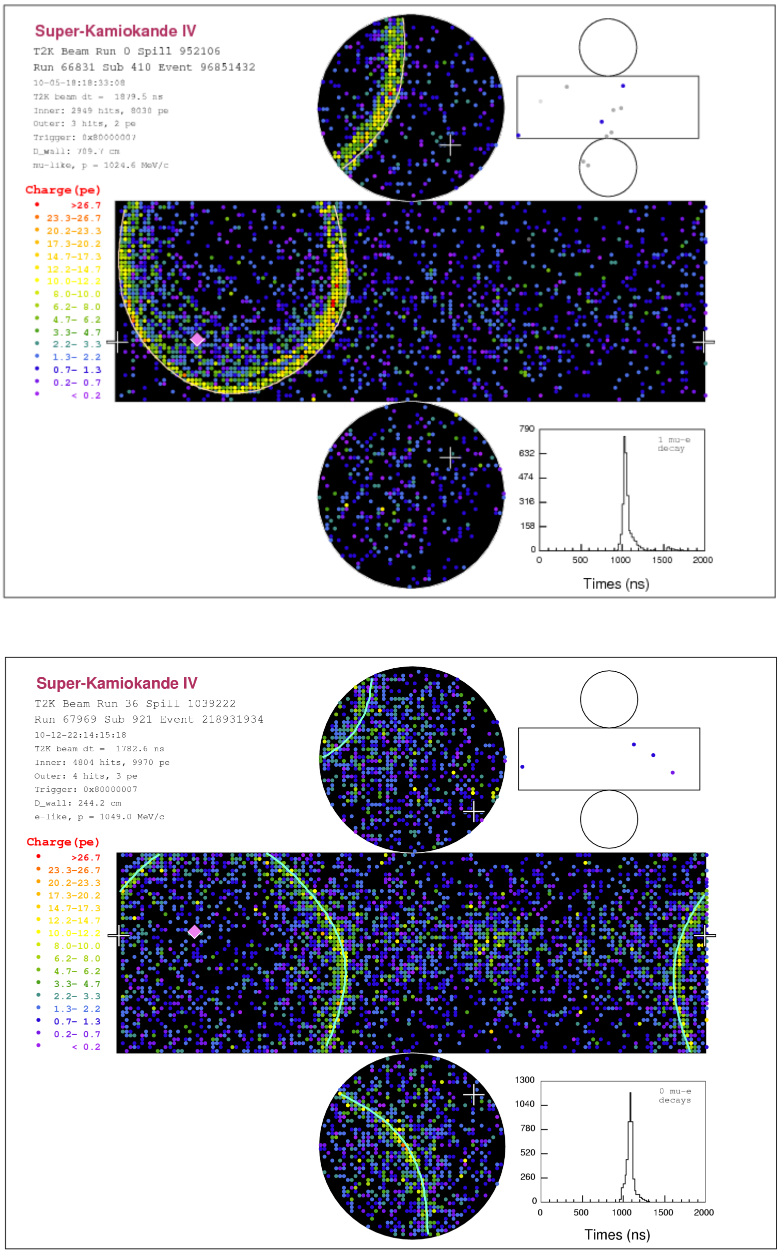

Figure 2.28: Super-K event displays showing neutrino interactions from the T2K beam. The top figure shows the muon ring from a $\nu_\mu$ event and the bottom figure shows the electron resulting from a $\nu_e$ interaction. Figures from [59].

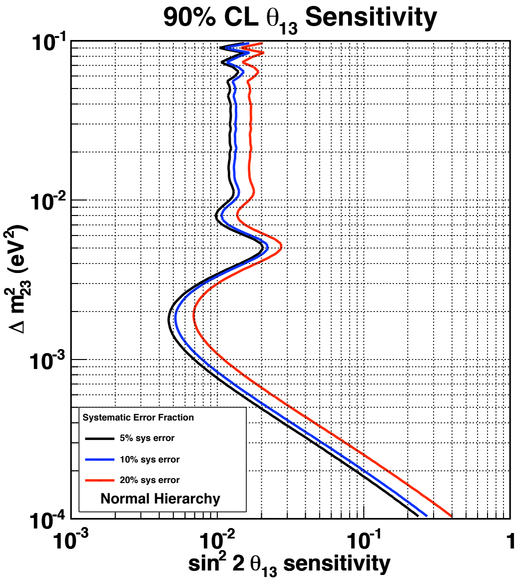

Figure 2.29: The T2K 90 % confidence limit sensitivity to $\sin^2 2\theta_{13}$ plotted as a function of $\Delta m^2_{23}$ after 5 years of running at a beam power of 0.75MW and assuming the normal hierarchy. The three curves correspond to three difference systematic uncertainty values: 5 % (black), 10 % (blue) and 20 % (red). Figure from [70].

The plot on the right of Figure 1.5 shows that antineutrino running would not be required with a second detector at the second oscillation maximum where the effect of $\delta$ is greater than at the first maximum. The value of $\delta$ could be fitted using data from both the first and second oscillation maxima. The second oscillation maximum occurs at a distance of $\sim 900$ km for T2K. This method has the advantage of not requiring a long antineutrino run but would require the construction of an entire new detector. The detector would need to be considerably larger than Super-K to account for the reduction of flux with distance, and would most likely be a liquid Argon TPC to provide a sufficiently high energy resolution.

# Chapter 3

# Reconstruction in the Electromagnetic Calorimeters

The reconstruction of both data and simulation in the DsECal and the Barrel ECals is performed by a software package called ecalRecon. P0D ECal event reconstruction is performed by a different software package and is not described here.

An overview of the ECal reconstruction chain is shown in a flow diagram in Figure 3.1. The figure breaks the reconstruction chain down into the 9 main algorithms. The chain begins with the hit preparation stage where the hit objects are prepared for the following algorithms. The green steps correspond to the 2D clustering stages and the yellow steps are those algorithms that manipulate the full 3D clusters.

## 3.1 Hit Preparation

The ECal reconstruction begins with data that have passed through the calibration software packages and contains a list of hits, called a hit selection, for each of the ECal modules. A hit corresponds to a charge deposit in a scintillator bar as measured by an MPPC. The first task of the reconstruction is to divide up each hit selection into two smaller selections separated by view. Each ECal detector module contains hits from two different views, which differ depending on the module type. Each hit at this stage only provides information in two dimensions: the coordinate of the bar and the coordinate of the layer. Figure 3.2 shows the coordinates measured for two hits in different layers, illustrating that the position along the bar is not measured by these hits. The hits are then grouped in time such that the time between successive hits in the group is less than 50 ns as illustrated by Figure 3.3. This is done in

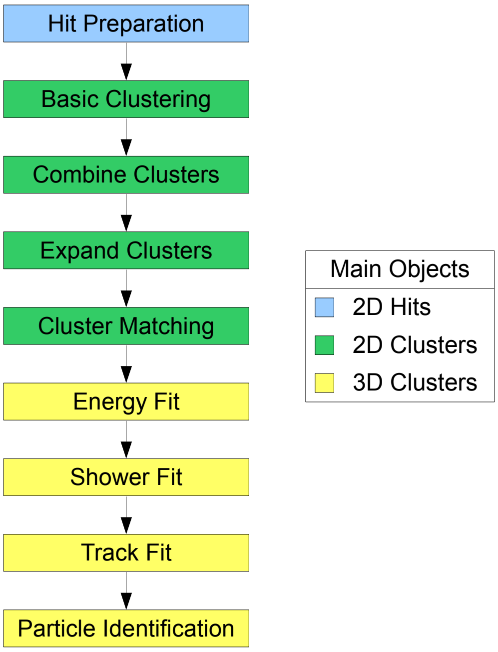

Figure 3.1: A flow diagram showing the main stages of the ECal reconstruction chain. The colours indicate the main type of reconstructed object at each step: 2D hits (blue), 2D clusters (green) and 3D clusters (yellow).

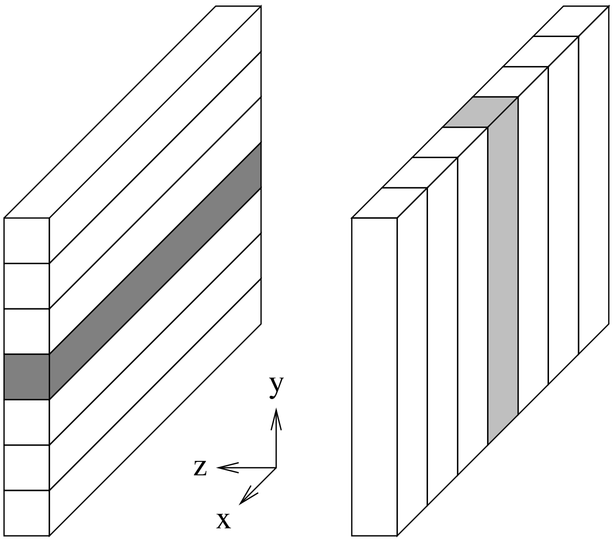

Figure 3.2: An illustration of the two dimensional form of single hits. The darkly shaded bar on the left has its $y$ coordinate defined by the bar and the $z$ coordinate defined by the layer. Similarly, the lightly shaded bar on the right has the $x$ coordinate defined by the bar and the $z$ coordinate defined by the layer.

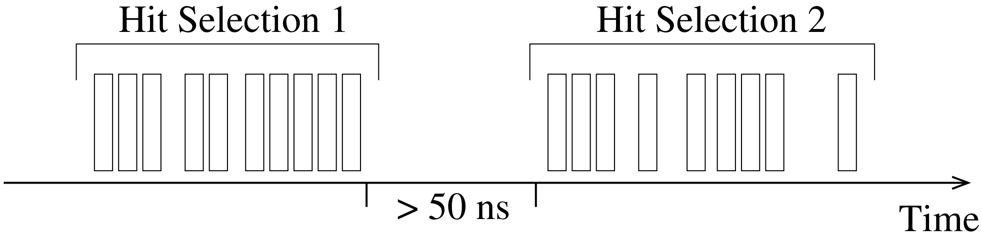

Figure 3.3: Illustration of the splitting up of hits into different hit selections when a gap of at least 50 ns exists between successive hits.

order to isolate the individual events to ensure that separate events in time are not reconstructed together whilst ensuring that an individual event is not split up.

All of the scintillator bars in the DsECal and the long bars in the Barrel ECal are read out on both ends so the reconstruction combines the hits from the sensors on each end of a bar using the method described in Section 3.1.1. The hit recombination process also applies the attenuation correction in order to correct for the attenuation of light travelling in the WLS fibre. Finally the charges of the hits are scaled to Minimum ionising particle Equivalent Units (MEU) using parameters measured from the deposition of energy in the scintillator bars by through-going cosmic ray muons.

### 3.1.1 Hit Recombination

The two hits from either end of a scintillator bar that is read out at both ends need to be recombined since the physical energy deposit was at a single point along the bar. The combination of two single hits on the same bar allows for the estimation of the coordinate along the length of the bar by using timing information shown in Equation 3.1:

$$d = 0.5\left(c_e\left(t_1 - t_2\right) + l\right) \tag{3.1}$$

where $d$ is the distance from sensor 1 to the hit position, $c_e$ is the effective speed of light in the fibre, $t_1$ and $t_2$ are the times of the hits on sensors 1 and 2 respectively, and $l$ is the distance from sensor 2 to sensor 1. The equation shows that if the hit on sensor 1 is later than the hit on sensor 2, the reconstructed hit position is closer to sensor 2 than sensor 1. The effective speed of light was determined and differs between simulation and data. The attenuation correction, as described in 3.1.2, is applied to the single hits and the charge of the combined hit is then calculated from the single hits. The combined hit is stored as a single object with both of the original contributing hits attached to it.

### 3.1.2 Attenuation Correction

After the coordinate along the bar has been estimated, the attenuation correction can be applied to correct for the light lost in the wavelength shifting fibre. For single ended bars, the position along the length of the bar is assumed to be at the centre. The correction is applied using a scale factor calculated by dividing the attenuation factor at the hit position by the attenuation factor at a normalisation point, currently taken at a distance of 1 m from the end of the bar. The correction factor is used to scale the charge of the single hits. The parameters currently used to apply the correction were measured from a fibre scanning program during fibre quality assurance at the University of Warwick. These parameters will be updated in due course to those suggested by a study of muons from cosmic ray data taken in the ND280 pit.

## 3.2 Clustering

After the completion of the hit preparation stage the data consist of a series of hit selections containing hits from the same 2D view. The next objective is to group the hits together spatially in 2D such that the hits caused by the same incident particle are grouped together into a single, composite object. This process is known as clustering and in the ECals is currently performed in three separate algorithms that run sequentially. The sequence of clustering is: Basic Clustering, Combine Clusters and Expand Clusters. The clustering criteria were tuned using the simulation. After the completion of the 2D clustering process an incident particle should consist of two 2D clusters, one in each view.

### 3.2.1 Basic Clustering

The first stage of clustering uses the hit with the highest charge as a seed and tries to cluster hits in neighbouring bars and layers. Hits are clustered with the seed hit if all of the following criteria are met:

i Hit is in the neighbouring or next-to neighbouring layer in a given view.

ii Hit is in the neighbouring bar within the same layer.

iii Hit time is within ±15 ns of the seed hit time.

Figure 3.4 gives a visual representation of the first two points listed above. Once all the possible hits have been clustered with the seed hit, the algorithm runs recursively over the clustered hits, with each hit becoming the seed in turn. In this way the search criteria are applied to all hits that are clustered, ending when no more unclustered hits can be grouped with any of the hits in the cluster. At this point, the algorithm then tries to repeat the entire process again with any hits that are not associated with the first cluster and continues until no more clusters can be formed. A minimum of three hits must be clustered before the object is passed on to the next algorithm.

### 3.2.2 Combine Clusters

The cluster merging algorithm aims to combine the clusters from basic clustering for events that have some sparse regions in terms of hits. For example, hadronic showers can often have regions without many hits and could be reconstructed as multiple objects by the basic clustering algorithm. The cluster with the highest number of hits is used as the seed and then attempts are made to combine it with the smaller clusters. The times of the clusters must agree within 40 ns, where the cluster time is defined as the average of the constituent hit times. Secondly, the clusters must match geometrically in 2D using the equation given below, in this case for the XZ view:

$$\Delta = (x_C - x_S) + \frac{wx_S}{wz_S}\,(z_C - z_S) \tag{3.2}$$

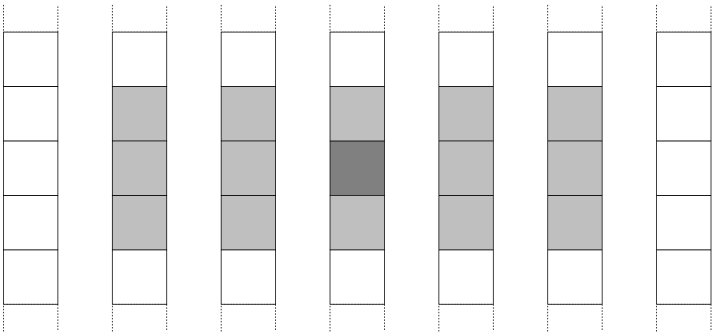

Figure 3.4: A schematic showing how the basic clustering works. The seed hit shown in dark grey is clustered with any hits located in the positions shown in lighter grey. The apparent gaps between the layers are the layers in the other view.

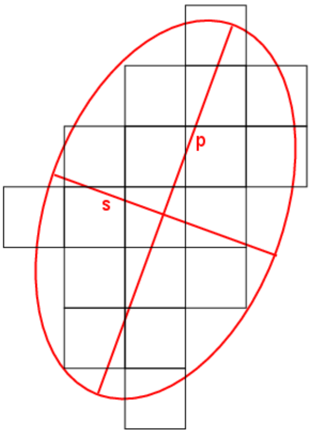

Figure 3.5: A graphical representation of a PCA of a cluster of hits to give the primary (p) and secondary (s) axes of the cluster, shown in red.

where the $C$ subscript is for the candidate cluster and the $S$ subscript is for the seed cluster. The positions $(x,\, z)$ are the average positions of the clusters and the widths $(wx,\, wz)$ are obtained from a charge weighted principal component analysis (PCA) of each cluster, giving the relative extent of the cluster in that direction. Figure 3.5 shows a graphical representation of the PCA method used to find the two axes of the cluster of hits. The parameter $\Delta$ is a measure of how closely related the two objects are, given the position and shape of the seed cluster. If the two clusters form a $\Delta$ value that satisfies the criterion $|\Delta| < 80\,\mathrm{mm}$ then the clusters are merged together to form a single cluster.

### 3.2.3 Expand Clusters

Expand clusters can be considered as an analogous algorithm to combine clusters that tries to add unmatched hits into the 2D clusters. Each unclustered hit is considered in turn and the algorithm tries to match it with each of the clusters in the same view. The first criterion is that the hit time and the cluster time must agree within 40 ns. The second criterion is a similar, but more complex version of Equation 3.2 used to merge clusters. If the hit passes both of the cuts then the hit is added to the cluster.

## 3.3 Tracker Object Seeds

In the global ND280 reconstruction framework the ECal reconstruction is performed after the reconstruction in the tracker region. This allows the reconstructed objects in the tracker to be used to define positions and regions of interest in the ECals. The algorithm looks at all tracks from the FGDs and TPCs, including those that are matched together between FGDs and TPCs and those that are FGD or TPC only. The tracks are then extrapolated to the front face of the ECal using a Kalman filter and if the extrapolation succeeds then a seed point is defined. The seed point stores the position, direction and momentum of the extrapolated track, defined at the front face of the ECal module. The seed points can be used in the cluster matching described in Section 3.4.

## 3.4 Cluster Matching

The 2D clusters from each view need to be combined into full 3D objects by matching the 2D clusters from one view with the 2D clusters from the other view. The cluster matching algorithm calculates two sets of matching likelihoods. The first set of likelihoods are calculated using the seed points discussed in Section 3.3 to match clusters together and the second set are from a local likelihood method in the case that no tracker seeds were found.

The seeded cluster matching considers only the hits from the two front-most layers of the 2D clusters. It then generates a likelihood based on the 2D position and time of the two clusters compared to the seed point. The local likelihoods are calculated using properties of the clusters and the criteria for matching come from two parameters calculated for the two candidate 2D clusters:

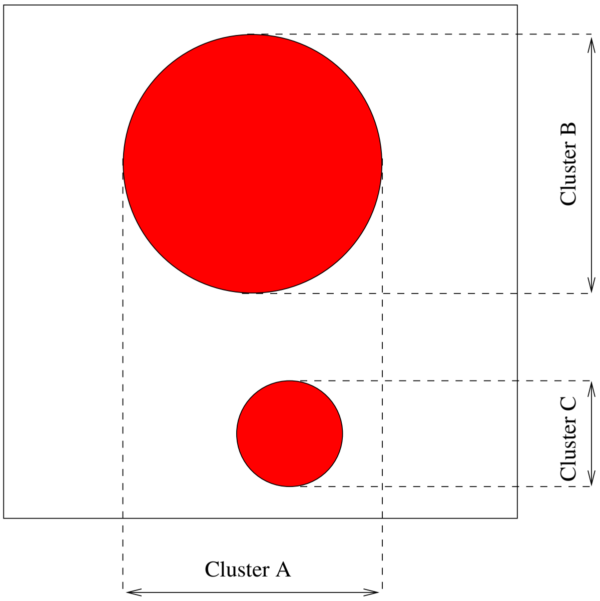

Figure 3.6: An illustration of overlapping clusters. Cluster A, a superposition of two clusters, will be matched with either cluster B or C depending on the result of the clustering likelihood. In this case, cluster A would be matched with cluster B since they are the most similar, and cluster C would remain as an unmatched cluster.

i Ratio of cluster charges.

ii Difference in starting layer between the two clusters, where the starting layer is the closest hit layer to the centre of the ND280.

The likelihood variable is formed between all possible combinations of clusters from one view with clusters from the other view. The pairs of clusters with the best likelihood value are combined if the likelihood passes a quality cut. In the event that a cluster could be matched with two clusters from the other view, the match with the best likelihood value is taken. The merged clusters are stored as 3D clusters and any clusters that were not matched are stored separately as unmatched 2D clusters. In the case shown in Figure 3.6 where there are two clusters in one view but only a single cluster in the other view as the deposits are overlapping, the pair with the best likelihood are matched. The example shown in Figure 3.6 is typical of an electron that emitted a Bremsstrahlung photon before reaching the detector, and the tracker seeding would also help to get the correct match as an electron track from the TPC would be located in the region where clusters A and B overlap.

### 3.4.1 Rematching

The rematching step tries to associate any unclustered hits with the unmatched 2D clusters in the other view. This is particularly important for very low energy particles that may have produced three hits in one view and only one or two hits in the other view. The algorithm was originally developed for looking for photons from $\pi^0$ decays. The three hit threshold in the basic clustering algorithm means that low energy objects may not be reconstructed if there are not enough hits to form a cluster in one of the views. A hit is associated with a cluster if it passes a tight time cut of 10 ns between the hit time and the cluster time and a cut on the layer number given below:

$$L_{min} - 1 \leq L_{hit} \leq L_{max} + 1 \tag{3.3}$$

where $L_{hit}$ is the layer of the hit and $L_{min}$ and $L_{max}$ are the minimum and maximum layers of the cluster. The process is repeated for all of the unmatched hits and unmatched clusters, with any clusters that have extra hits associated being made into 3D clusters.

### 3.4.2 Hit Position Recalculation

After the 2D clusters have been combined to form a 3D cluster the hits can have the position along the bar recalculated using the hits from the other view. This provides a more accurate position than the one previously obtained in the initial hit recombination, discussed in 3.1.1. The third coordinate is measured by performing a least squares fit of all the hits in the neighbouring four layers that are in the other view. After the position has been calculated, the hit is re-calibrated in the same way as in section 3.1, applying both the MEU charge scaling and the attenuation correction. This does not have the effect of applying the calibrations twice because the original single hit charges are used, not the calculated charge of the recombined hit.

The hit position recalculation step represents the last step in the clustering together of the hits into a single 3D object. Figure 3.7 shows a comparison of the number of hits in a 3D object in the DsECal between testbeam data and simulation for electrons at four different energies: 400 MeV (top left), 600 MeV (top right), 1.0 GeV (bottom left) and 2.0 GeV (bottom right). These data were taken during the DsECal testbeam program in 2009 at CERN, described in Appendix A. Good agreement is seen between the data and simulation across the energy range, with the distributions slightly wider in data that in the simulation. The distributions show

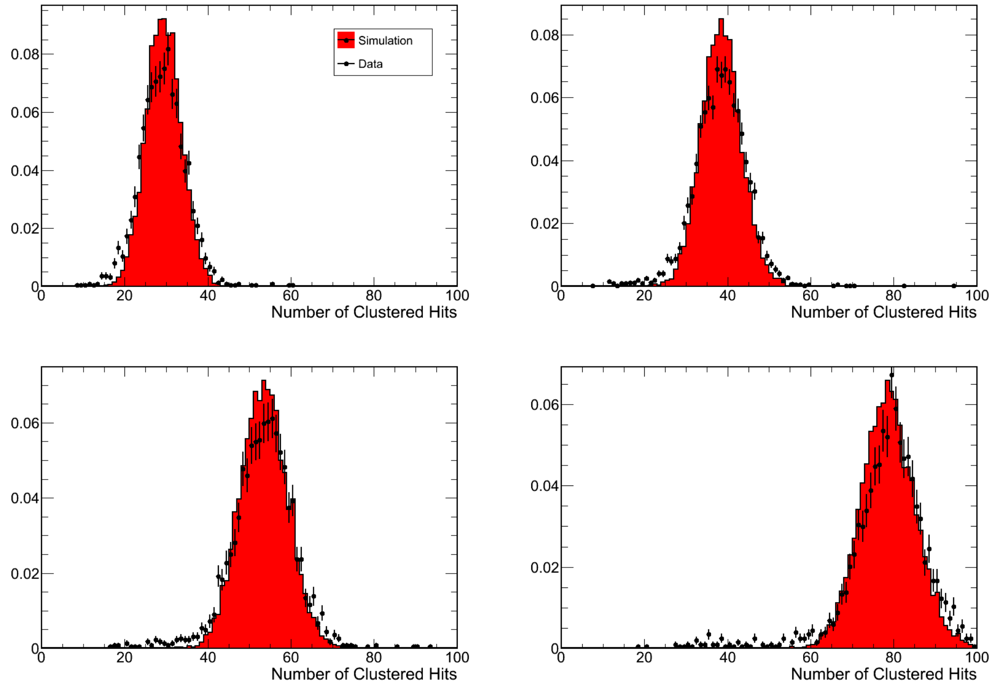

Figure 3.7: A comparison of the number of hits in a cluster between testbeam data and simulation for incident electrons at various energies: 400 MeV (top left), 600 MeV (top right), 1.0 GeV (bottom left) and 2.0 GeV (bottom right). The histograms are all normalised by area.

that the reconstruction performs well and matches the simulation expectation. The efficiency for reconstructing hits in a given layer was measured using cosmic ray muons and is shown in Figure 3.8 to be about 99% averaged across the layers.

The data consists of a series of fully reconstructed 3D clusters after the completion of the cluster matching algorithm. The remaining steps in the reconstruction chain are based on the manipulation of these 3D clusters to extract physics information such as the particle energy and particle type.

## 3.5 Electromagnetic Energy Measurement

The primary purpose of an electromagnetic calorimeter is to measure the energy of the showering particles. All of the reconstructed 3D clusters are passed into the energy fitting algorithm. The fit is actually an electromagnetic shower fit, so all objects are fitted under the hypothesis that they are electromagnetic showers, regardless of the actual event type. The energy measurement is performed by a likelihood fit using the three parameters listed below:

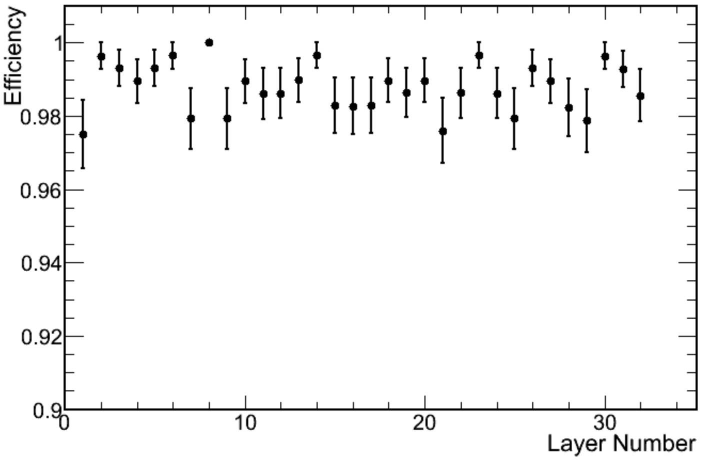

Figure 3.8: The efficiency of reconstructing hits in each layer of the DsECal measured using cosmic ray muons. The uncertainty on each point is from binomial statistics. No points are shown for the first and last layers because a layer was predicted to be hit if there were hits in the neighbouring layers, a criterion undefined for the front and back layers.

- The total charge of the cluster.
- The RMS of the charge divided by the mean of the charge.
- The skew of the charge distribution.

The fit was tuned on simulated particle gun photons at 53 different energies ranging from 75 MeV to 25 GeV. The coverage in energy is not uniform and concentrates on the region below 2 GeV but the higher energy events are included in the training to ensure that the likelihood is well described in the high energy tail. Each of the three parameters is measured from the simulation for the 53 energy points and smooth distributions are made by using a cubic spline. Each point is fitted with the neighbouring six points and the point is moved to the position returned by the fit, with the goal of removing statistical fluctuations from the distribution. The cubic spline interpolated distributions for the three parameters are used in the fit to calculate the likelihood.

### 3.5.1 Energy Response

The energy response for electrons was tested using data from the DsECal testbeam running. The testbeam was able to provide electrons with energies ranging from 400 MeV to 2.0 GeV. Above 2.0 GeV the fraction of electrons in the beam compared to other particles was very small and it was not possible to gain enough events to

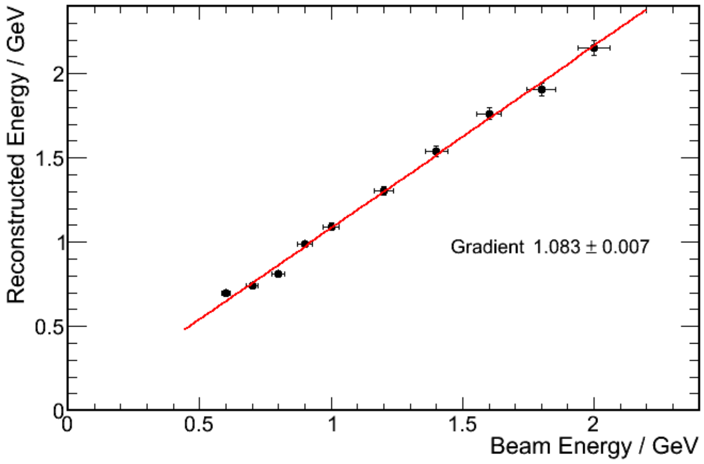

Figure 3.9: Reconstructed energy plotted as a function of the beam energy for testbeam electron data with a linear fit forced through the origin.

analyse. The current supplied to the beamline magnets was varied in order to select both the required energy and the sign of the charge of the particles.

The reconstructed energy of electrons was measured using the energy fit and compared to the beam energy. The energy was measured on a run by run basis by fitting the reconstructed energy with a truncated Gaussian distribution. The mean of the Gaussian distribution was taken as the energy measurement for that run and the width was taken as the uncertainty. Figure 3.9 shows the measured ECal energy $E_{reco}$ plotted as a function of the beam energy $E_{beam}$ with a linear line fit of the form:

$$E_{reco} = mE_{beam} + C \tag{3.4}$$

A free fit to the data measured a value of the constant term $C$ consistent with zero so the fit was repeated with the value of $C$ set to zero. The gradient was measured to be $m = 1.083 \pm 0.007$ meaning that the reconstructed energy overestimated the true energy by approximately 8 %. The inverse of $m$ provides the scaling factor between the reconstructed energy $E_{reco}$ and corrected energy $E_{final}$:

$$E_{final} = 0.923E_{reco} \tag{3.5}$$

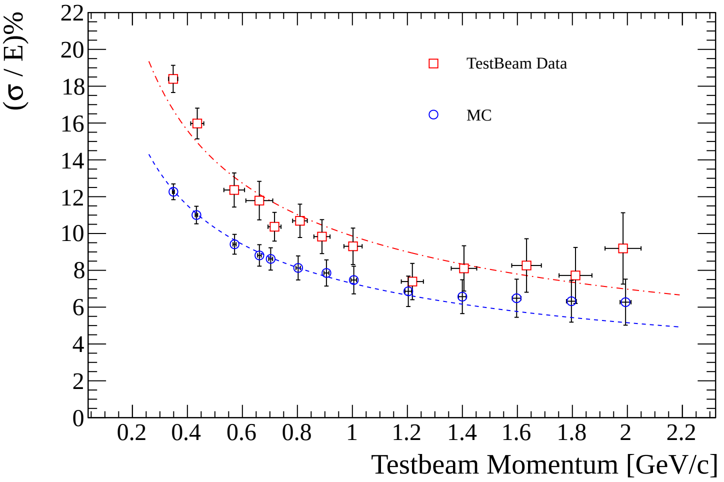

Figure 3.10: A comparison of the energy resolution for testbeam electron data and simulation. The dashed lines show the best fits using the function given in Equation 3.6. Figure from [72].

### 3.5.2 Energy Resolution

The energy resolution of a sampling calorimeter when considering only the stochastic term is given by[71]:

$$\frac{\sigma}{E} = \frac{A}{\sqrt{E}} \tag{3.6}$$

The energy resolution for testbeam data and simulation is shown in Figure 3.10 where the dashed curves show the fits of the function given in Equation 3.6. The fitted values of $A$ were $9.86 \pm 0.24\,\mathrm{GeV}^{-0.5}$ and $7.29 \pm 0.14\,\mathrm{GeV}^{-0.5}$ for data and simulation respectively, showing that the energy resolution is poorer in data than simulation. The energy resolution for data is therefore approximately $\frac{10\,\%}{\sqrt{E}}$, a complimentary result to the TPC momentum resolution that decreases at high momentum. A possible reason for the difference in resolution between the data and simulation comes from the spread of particle momenta in the testbeam data. The simulated particles were produced with identical momenta at the beam momentum value whereas in the data there would be some spread in the values, of the order of a few percent, and this would have the effect of making the energy resolution appear worse. In addition to this, there were large temperature variations at the testbeam and the energy measurement is dependent on the temperature as it depends on the hit charges.

## 3.6 Track and Shower Fitting

Particle interactions in sampling calorimeters fall into two broad geometrical categories: tracks and showers. Track-like particles such as muons tend to pass directly through the detector depositing energy uniformly along the length of the track. Showering particles, for example electrons, interact to produce a cascade of secondary particles, all depositing energy over a larger volume. All reconstructed 3D clusters are fitted under both track and shower hypotheses and the decision about which is the correct choice is made by the particle identification algorithm, described in section 3.7

### 3.6.1 The Shower Fitter

The shower shape is fitted using a 3D PCA method. The position of each hit in the cluster is added to the PCA an integer number of times depending on the charge of the hit. This method is used as it allows more weight to be given to the hits with the highest charges. The result of the PCA analysis is used to define the central position of the shower, the direction and the opening angle. The direction is stored in the form of three direction cosines derived from the three principal axes of the PCA. The shower angle $\theta$ is calculated from the relative sizes of the primary $p$ and secondary $s$ axes from the PCA in the following way:

$$\tan\theta = \frac{s}{p} \tag{3.7}$$

### 3.6.2 The Track Fitter

The track fitter separates the cluster hits into the two views and generates a single point per layer, called a *node*, that is defined as the charge weighted average of all of the hit positions in that layer. The algorithm fits the node points for each 2D view using a 2D linear fit. The fit moves incrementally through the nodes fitting each node with the four neighbouring nodes, updating the position of the node with the results from the fitting procedure. The 2D fitting procedure outputs two lists of fitted nodes, one for each 2D view.

The two sets of 2D nodes are then combined into a single set of 3D nodes. The 3D nodes are fitted using a 3D linear fit with each node fitted in turn with the ten neighbouring points. The fitted 3D nodes are stored as part of the track object, with each node having a position and direction defined by the fitting process. The position and direction of the track object are defined to be identical to the position and direction of the first track node.

## 3.7 Particle Identification

The ECal Particle Identification (PID) algorithm [73] returns a variable that is used to discriminate between the track-like and shower-like hypotheses. The algorithm used takes the form of a single hidden layer artificial neural network (ANN) implemented using the TMVA[74] package from ROOT[75]. The neural network takes five input variables, listed below, and combines them into a single output.

- AMR: The Axis Max Ratio gives the ratio of the primary and secondary components of a 2D PCA. The variable is calculated separately in each 2D view before being combined by averaging. For very narrow objects, the secondary axis component approaches zero meaning that the ratio can approach infinity. The variable is therefore defined to be within the range 0 to 300, where any values that would be greater than 300 are set to be 300. A shower-like event has a low AMR as showers have a high width whereas track-like events have a large AMR due to the small width of the object.
- Max Ratio: Max Ratio is a charge based variable where the total charge in each layer is calculated and ordered. The ratio is taken between the highest and lowest of these, excluding those layers with zero charge. Track-like events have a Max Ratio close to one because all of the hits should have the same deposited energy as tracks are generally formed by minimum ionising particles (MIPs). Showers have a high charge density core with lower charged hits on the edges of the shower, meaning the Max Ratio is larger than for tracks.
- EM Likelihood: This variable is the likelihood of an event being an electromagnetic shower and is calculated as part of the energy fit described in section 3.5. Values close to zero are measured for shower-like events and larger values for track-like events.
- ShowerAngle: The tangent of the shower angle is the ratio of the secondary and primary components of a 3D PCA. By construction, ShowerAngle is bounded between 0 and 1, where track-like objects have values close to 0 and shower-like objects have values further from 0.
- ShowerWidth: The tertiary component of a 3D PCA analysis. PCA components are normalised, hence ShowerWidth is bounded from 0 to 1. Shower-like events have a larger width than track-like events.

The neural network must be trained to identify the different types of events, as discussed in section 3.7.1. The neural network uses weights generated by the training process to combine the five input variables into a single output variable. The weights used depend on the event type as different weights are used for the different ECal modules and angles of incidence. Currently there are separate weights for the DsECal and the Barrel ECal and for five different angles of incidence: 0°, 20°, 40°, 60° and 80°. The ANN must be retrained whenever the distributions of the input variables are changed, for example when the charge calibration procedure was changed.

The ANN output parameter is an approximation to a likelihood, meaning that it is not strictly bounded to be between 0 and 1 so there is a small amount of leakage over the 0 and 1 boundaries. Shower-like events are defined to have a value close to 0 whereas track-like events have a value close to 1.

The value of the ANN output variable is used to define how the final objects from ecalRecon are stored. If the value is less than 0.5, a shower-like hypothesis is assumed and the shower object from the shower fitter is stored as the main constituent of the saved cluster. If the value is greater than 0.5 the track object is saved as the primary constituent. The object from the hypothesis that is not selected by the PID is also stored within the final cluster.

### 3.7.1 Training the Neural Network

The weight files used in the hidden layer were produced by training the ANN with Monte Carlo simulation data. The PID uses different sets of weight files for the DsECal and Barrel ECal modules and also for different angles of incidence. Simulated data were produced for electrons, muons and photons for the different detectors and required angles of incidence. The energy distribution of the particles was defined as the energy distribution of the different particles expected in the ECals from neutrino beam data. The electron and photon samples were combined to make a single showering sample and the muons were used to create the track sample. The shower and track samples for different angles were used by the ANN training to produce the weight files.

## 3.8 PID Performance

In order to quantify the performance of the PID it is required that the particle type is known from an independent source. The PID performance has been studied for electrons and muons. The data sample for electrons came from the DsECal testbeam run, described below. The muon sample considered was from ND280 data from the first running period.

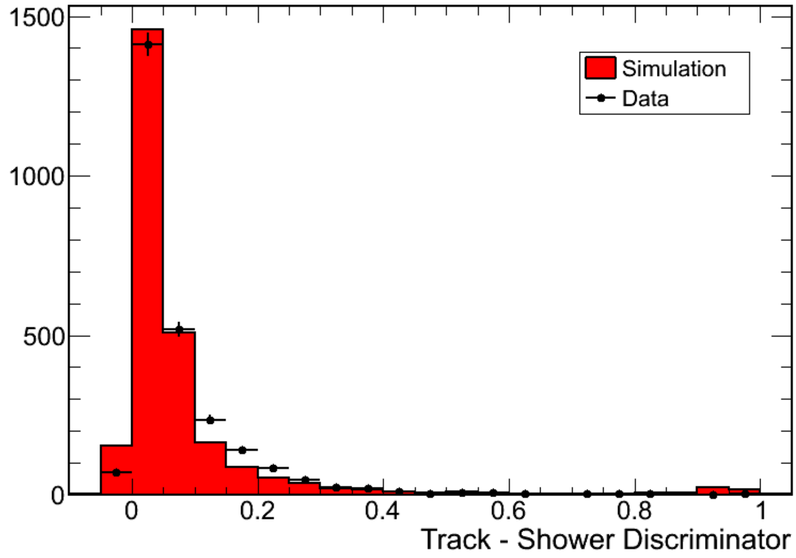

Figure 3.11: The output from the ECal PID shown for 600 MeV electrons fired into the DsECal at an incident angle of 30° at the CERN testbeam. The testbeam data events were from runs 20228 and 20241. The simulation shows particle gun electrons at the same energy and angle as the data.

### 3.8.1 Testbeam Electrons

The PID performance was tested using a sample of electrons from the DsECal testbeam program, described in Appendix A. The type of particle entering the DsECal at the testbeam was measured using two Čerenkov detectors and a time of flight (TOF) counter. These detectors were used to provide an external particle identification source that was used to obtain a pure sample of electrons that could then be used to test the ECal PID algorithm. Figure 3.11 shows the PID performance for the combined data from two negative polarity runs taken at the testbeam with an energy of 600 MeV and with the particles travelling at an angle of 30° to the face of the ECal. A thorough study of the electron selection efficiency in data and simulation for all of the testbeam data is presented in Chapter 4 as part of the study of systematic uncertainties.

### 3.8.2 Through-Going Muons

Unfortunately, the muons in the CERN testbeam data were indistinguishable from the track-like charged pions, so an alternate source of muons was required. Cosmic rays predominantly consist of muons, but there can be other particles such as electrons in cosmic showers so the decision was made to use muons that traverse all

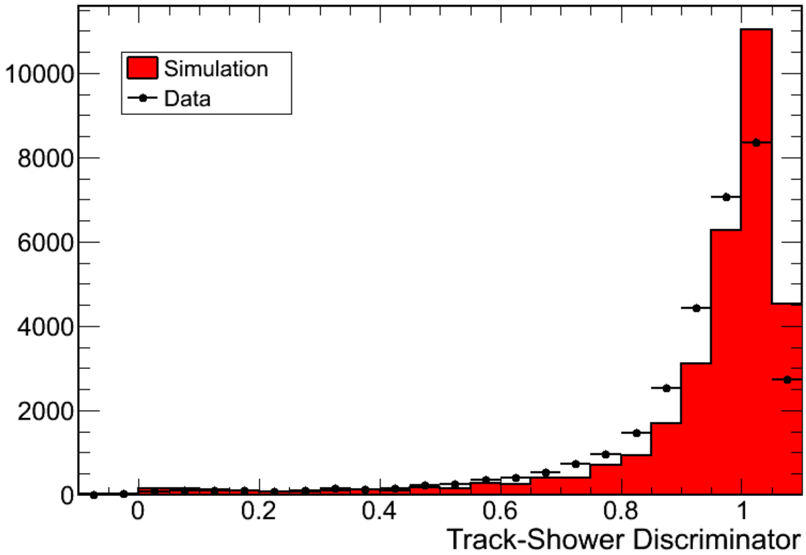

Figure 3.12: The output from the ECal PID shown for muons created in the sand upstream of the ND280 or in the P0D that pass through all three TPCs into the DsECal. Only tracks with muon-like PID signals from all three TPCs were selected. The simulation sample consists purely of muons created in the P0D.

three TPCs in the ND280 pit data. The sample therefore consisted of muons from CC $\nu_\mu$ interactions in the sand upstream of the near detector and within the P0D subdetector. It was then required that the muons had a muon-like PID in all three of the TPCs to ensure that a very pure sample of muons was obtained. At the time of the study there was no Monte Carlo simulation of the neutrino interactions in the sand upstream of the ND280, so the simulation sample consisted purely of CC $\nu_\mu$ interactions in the P0D. Figure 3.12 shows the comparison of the data sample to the simulation. The data peak is wider than the peak in the simulation, but the peak is still contained within the track-like half of the distribution so the effect of this discrepancy in terms of PID performance is not large, as discussed in 3.8.3. However, subsequent re-trainings of the ANN have improved the agreement in shape between data and simulation, but Figure 3.12 is presented here as the software version was the same as the one used for the analysis described in Chapter 4. It is also clear that the shape differences do not affect the region below 0.5, the region where cuts are applied in order to select electrons.

| Particle Type | | Efficiency / % |
|---|---|---|
| $e^-$ | Data | 98.8 ± 0.2 |
| | Simulation | 97.0 ± 0.3 |
| $\mu^-$ | Data | 96.09 ± 0.01 |
| | Simulation | 96.10 ± 0.04 |

Table 3.1: Efficiency for selecting electrons and muons using the ECal PID in the DsECal. The efficiency is calculated by dividing the number of objects passing the corresponding cut in Equation 3.8 by the total number of reconstructed objects. The quoted uncertainties are purely statistical. The data samples are described in section 3.8.

### 3.8.3 Summary

The basic definition for distinguishing between track-like and shower-like objects using the track-shower discriminator $D$ from the ANN is given below:

$$\text{Track: } D \geq 0.5 \quad \text{and} \quad \text{Shower: } D < 0.5 \tag{3.8}$$

The result of applying the criteria described in Equation 3.8 to the testbeam electron and through-going muon samples shown in Figures 3.11 and 3.12 are shown in Table 3.1. The efficiency was defined as the number of events selected by applying the cut divided by the total number of events in the sample. The efficiency for selecting the 600 MeV/c electrons is higher in data than in simulation but the muon selection efficiency agrees well between data and simulation. The results show that the ECals provide a powerful variable to efficiently separate electrons and muons. The value (1 − efficiency) gives the fraction of events incorrectly identified.

The ECal is currently used in a number of near detector analyses. An analysis using the ECal PID with respect to selecting electrons in the ND280 as part of a study of the $\nu_e$ component of the beam is presented in Chapter 4. The ECal PID is also used as part of the ND280 analysis of $\bar{\nu}_\mu$ interactions. The ECal reconstruction also plays a vital role in the identification of decay photons from $\pi^0$ decays as part of an analysis of NC $\pi^0$ production, an analysis that relies on the ECals to reconstruct both of the decay photons.

# Chapter 4

# Measurement of the Intrinsic $\nu_e$ Component of the Beam

## 4.1 Motivation

The two largest backgrounds to the $\nu_\mu \rightarrow \nu_e$ oscillation signal at Super-K are intrinsic beam $\nu_e$ interactions and misidentified NC $\pi^0$ events. The two backgrounds are approximately equal in size and hence it is vital that the $\nu_e$ component of the beam is well understood. A measurement of the $\nu_e$ component of the beam using the ND280 constrains the background at Super-K by reducing the dependence on the flux simulation. An analysis of NC $\pi^0$ events is currently being developed by ND280 collaborators and is not discussed here.

## 4.2 $\nu_e$ Production in the Beamline

A small fraction of the neutrinos produced at J-PARC are electron neutrinos. Electron neutrinos are generally produced by less common decays of the mesons that also produce the muon neutrino flux. The main processes that produce electron neutrinos were given in Section 2.2.1, but a complete list from the neutrino flux simulation is given in Table 4.1.

The $\mu^+$ shown in the table comes from the decay of mesons that produce the $\nu_\mu$ flux. Figure 4.1 shows the simulated neutrino flux at ND280: the left plot shows the relative sizes of the $\nu_\mu$ and $\nu_e$ fluxes and the plot on the right shows the contributions to the $\nu_e$ flux coming from the decays of kaons, muons and pions. The pion component is negligible compared to the muon and kaon components because the decay mode $\pi^+ \rightarrow \nu_e + e^+$ is suppressed by helicity with respect to the

| Parent Particle | Decay Process |
|---|---|
| $\mu^+$ | $\mu^+ \rightarrow \nu_e + e^+ + \bar{\nu_\mu}$ |
| $K^+$ | $K^+ \rightarrow \nu_e + e^+ + \pi^0$ |
| $K_L^0$ | $K_L^0 \rightarrow \nu_e + e^+ + \pi^-$ |
| $\pi^+$ | $\pi^+ \rightarrow \nu_e + e^+$ |

Table 4.1: A list of the four decay processes that produce $\nu_e$ considered in the T2K beam simulation [76].

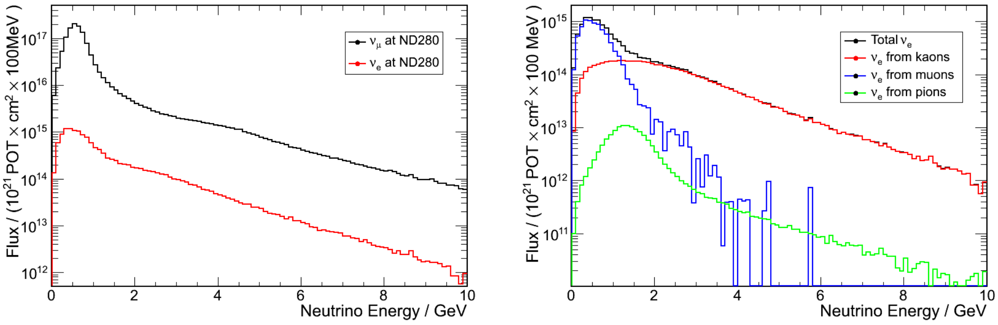

Figure 4.1: Left: Comparison of the $\nu_\mu$ and $\nu_e$ fluxes at ND280. Right: The ND280 $\nu_e$ flux broken down by parent type.

$\pi^+ \rightarrow \nu_\mu + \mu^+$ decay mode[1]. At neutrino energies below about 1.0 GeV the $\nu_e$ flux is dominated by the muon component and the kaon component dominates at higher energies.

## 4.3 Data Samples

### 4.3.1 ND280 Data

The analyses presented here used the total amount of data taken by the ND280 from February 2010 until the shutdown caused by the earthquake on March 11th 2011. There were two main data taking periods: Run 1 and Run 2. The Run 1 data came from the period between February 2010 to June 2010 with only the DsECal of the whole ECal suite installed. The Run 2 period lasted from October 2010 until the shutdown in March 2011 and had all of the Barrel and P0D ECal modules installed, and the number of bunches in the beam was increased from 6 to 8.

Only data that had correct data quality flags were used. The data quality

---

[1] It is more likely to have a right-handed chiral $\mu^+$ with left-handed helicity than a right-handed chiral $e^+$ with left-handed helicity, hence the branching fraction for $\pi^+ \rightarrow \nu_\mu + \mu^+$ is considerably larger than $\pi^+ \rightarrow \nu_e + e^+$.

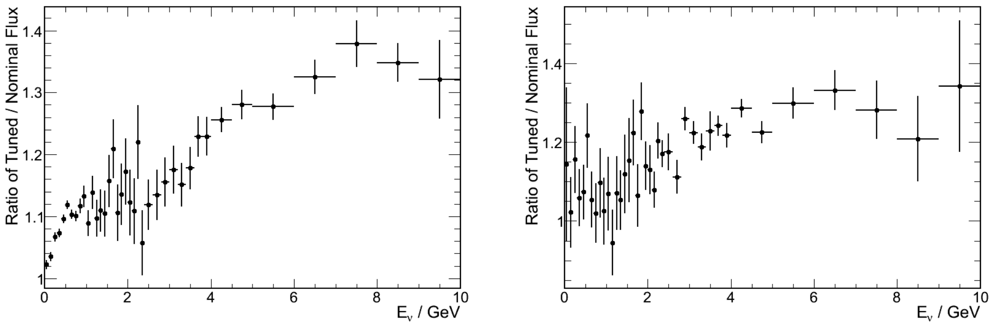

Figure 4.2: The ratio of the nominal flux and the re-tuned flux used to re-weight the simulation for the $\nu_\mu$ component (left) and the $\nu_e$ component (right).

flags are used to identify events that occurred during periods of detector instability or detector down-time. In this analysis the entire ND280 was required to be operational and working correctly, making the total amount of data $1.09 \times 10^{20}$ POT composed of $2.99 \times 10^{19}$ POT for Run 1 and $7.92 \times 10^{19}$ POT for Run 2.

### 4.3.2 Monte Carlo Simulation

The Monte Carlo simulation data used was produced using the GENIE[77] neutrino interaction generator. The particles are tracked through the full detector simulation using GEANT[60] before going through the electronics simulation. Separate simulation samples were used for Run 1 and Run 2 due to the differences in the detector geometry and the number of bunches in the beam. The simulation was re-weighted to update the beam flux to the most recent re-tuned values, as discussed in Section 2.2.1. Figure 4.2 shows the ratio of the re-weighted flux to the nominal flux that the simulation was produced with. The plot on the left is for the $\nu_\mu$ component and the plot on the right is for the $\nu_e$ component. The changes as a result of the re-tune are large for the higher energy neutrinos coming from kaon decay.

## 4.4 Inclusive CC $\nu_e$ Measurement at the ND280

An electron neutrino interaction in the ND280 can only be inferred by considering the final state particles produced by the interaction. The goal of the analysis was to select CC $\nu_e$ events. The most important part of the CC $\nu_e$ interaction signature in the ND280 is the electron track, hence the selection of $\nu_e$ interactions is based on the selection of electrons. The backgrounds to the CC $\nu_e$ selection are large and are described in the following section.

### 4.4.1 Backgrounds

The backgrounds to the inclusive CC $\nu_e$ measurement predominantly come from $\nu_\mu$ interactions. The backgrounds can be divided into four categories: Non-FGD, $\nu_\mu\gamma$, $\nu_\mu\mu$ and $\nu_\mu$-other. The $\nu_\mu\gamma$ background and the majority of the Non-FGD background events are those where the selected track is actually an electron or positron, meaning that the PID has successfully identified the track. The $\nu_\mu\mu$ and $\nu_\mu$-other backgrounds are caused by failures of the PID.

#### Non-FGD Component

The Non-FGD background encompasses all backgrounds where the true starting point of the selected track is not in the FGD fiducial volume. These events can be selected by the analysis when the end point of the track is within the FGD fiducial volume and the track has been reconstructed in the wrong direction. Tracks can be reconstructed in the wrong direction when the time difference between the start and end of the track is smaller than the time resolution, and hence it is not possible to determine which end of the track is the start. The majority of the electrons and positrons in this sample are produced in $\gamma$ conversions arising from $\nu_\mu$ interactions.

#### $\nu_\mu\gamma$ Component

The $\nu_\mu\gamma$ background consists of events produced by a $\nu_\mu$ interaction somewhere in the detector, outside the FGD fiducial volume, that produces a $\gamma$ that converts in the FGD fiducial volume to produce an electron that mimics the $\nu_e$ signal. An example of an interaction that contributes to this background is the NC $\pi^0$ process where a $\nu_\mu$ scatters on a nucleon $N$ to produce a $\pi^0$

$$\nu_\mu + N \rightarrow \nu_\mu + N + \pi^0 \tag{4.1}$$

and the subsequent decay of the $\pi^0$:

$$\pi^0 \rightarrow \gamma + \gamma \tag{4.2}$$

The photons can interact with an atomic nucleus to produce an $e^+e^-$ pair. The background can thus be reduced by searching for the positron and looking at the invariant mass of the two tracks.

| Bunch Number | Time / ns |
|---|---|
| 1 | 2847 |
| 2 | 3434 |
| 3 | 4014 |
| 4 | 4598 |
| 5 | 5174 |
| 6 | 5756 |
| 7 | 6351 |
| 8 | 6923 |

Table 4.2: The mean time of the bunches from the T2K beam as measured in the FGDs for Run 1 and the first part of Run 2.

### $\nu_\mu\mu$ and $\nu_\mu$-other Components

The $\nu_\mu\mu$ and $\nu_\mu$-other backgrounds are small in comparison with the other two background components. The samples consist of $\nu_\mu$ interactions in the FGD fiducial volume where the outgoing particles are misidentified as electrons. These events are therefore caused by failures in the PID algorithm in identifying muons for $\nu_\mu\mu$, and pions and protons for $\nu_\mu$-other.

## 4.4.2 Preselection

The ND280 software considers the entire spill, consisting of the 6 or 8 bunches fast-extracted from the beam, as a single event. The first task of the analysis is to separate the data into objects from each of the 6 or 8 bunches. The gaps in time between the bunches are sufficiently large that an event from one bunch is entirely separate from an event in the following bunch. Figure 4.3 shows the time of the starting point of all tracks from the FGDs used to measure the bunch times for data and simulation. The 6 or 8 peaks in the time distribution were fitted with Gaussian functions and the parameters from the Gaussian fits were used to define the criteria used to select events in time with the beam. A 100 ms offset was found between data and simulation which was corrected by shifting the time of the simulated events. There was an additional shift of $\sim 170$ ns in the time of data events caused by some changes in the beam timing for the second half of Run 2. Table 4.2 summarises the central position of the bunches before the shift in Run 2, showing that the bunches are separated by about 600 ns.

Tracks that occur within $5\sigma$ of the expected bunch time of any of the 6 or 8 bunches are considered in the analysis and stored in the corresponding list of tracks. After the event has been split into bunches, the rest of the analysis can be considered

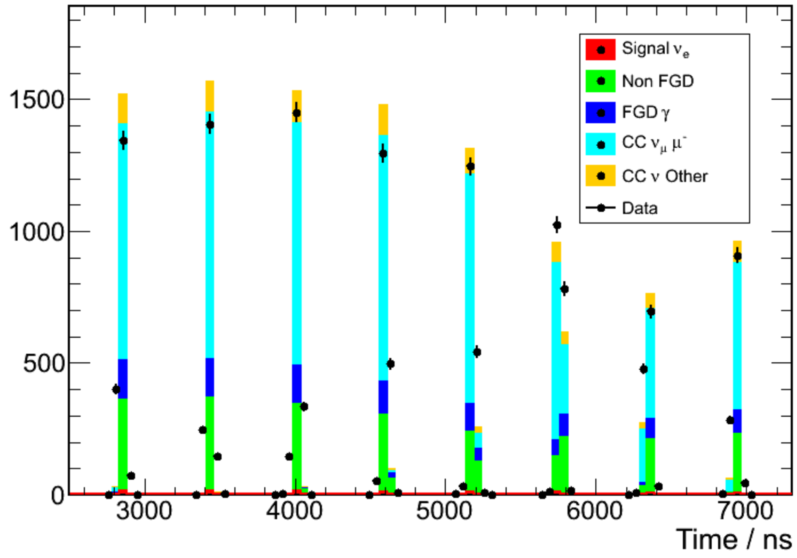

Figure 4.3: A comparison of track starting times for all tracks starting in the FGD fiducial volume for data and simulation where the simulation was scaled to have the same POT as the data sample.

in two main sections. The first section is the selection of the electron-candidate track and the second deals with vetoes coming from different parts of the ND280.

### 4.4.3 Electron Candidate Track Selection

The electron from a CC $\nu_e$ interaction should generally be the highest energy track with negative charge in the ND280, so this is the first of the track selection criteria. The selection does not simply use the track with the highest momentum because there are cases where the positive pion from a resonance event can have a higher reconstructed momentum than the electron. Track momentum is reconstructed in two different ways in the ND280: the momentum measured in the most upstream TPC ($p_{tpc}$) and the momentum measured using a Kalman filter to fit the entire track ($p_{global}$). The two momenta were compared to the true momentum $p_{true}$ from simulation and Figure 4.4 shows the values of $p_{global}-p_{true}$ plotted against $p_{tpc}-p_{true}$. The region in the red box shows events where $p_{tpc}$ agrees well with $p_{true}$ but $p_{global}$ is not in agreement with $p_{true}$. The plot does not have a region of events where $p_{global}$ out-performs $p_{tpc}$ so the decision was made to use the TPC momentum.

The track is then required to start within the fiducial volume of FGD1 or FGD2. The fiducial volume definition is the same as the one used in the ND280 $\nu_\mu$ analysis [78] and is detailed in Table 4.3. The fiducial volume is defined to ensure

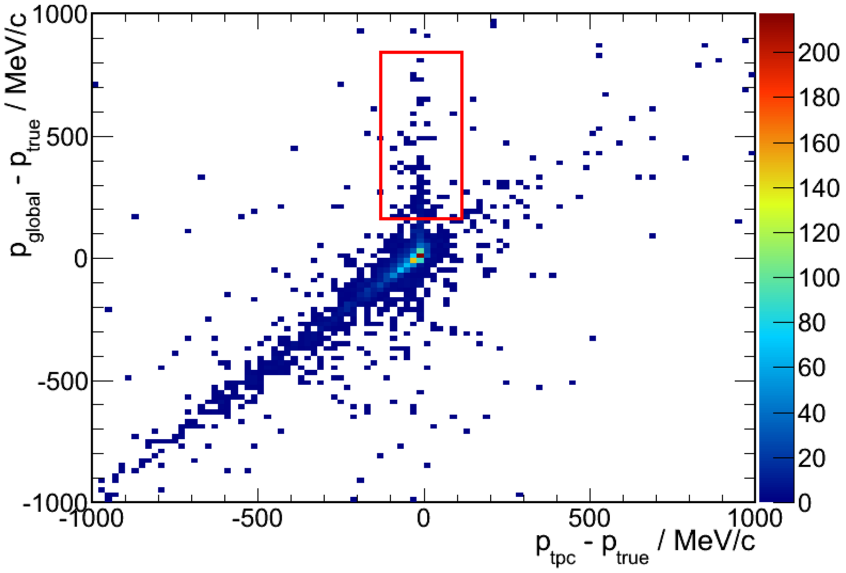

Figure 4.4: A plot of ($p_{global}$ - $p_{true}$) and ($p_{tpc}$ - $p_{true}$) for simulation. The region in the red box shows events where the TPC momentum agrees well with truth but the global momentum varies significantly from the true value.

| Coordinate | Minimum / mm | Maximum / mm |
|---|---|---|
| $X$ | -832.2 | 832.2 |
| $Y$ | -777.2 | 887.2 |
| $Z$ (FGD1) | 123.45 | 446.95 |
| $Z$ (FGD2) | 1481.45 | 1807.95 |

Table 4.3: The boundaries of the FGD fiducial volume. The FGDs are centred at (0 mm,55 mm) in the ($X$,$Y$) plane so the $X$ and $Y$ constraints are both symmetric about the centre point.

that the track starting point is properly reconstructed within the FGD and does not occur very close to the edge of the detector. In the $X$ and $Y$ coordinates the fiducial volume has a clearance of 100 mm from the edges of the total active volume and in $Z$ the fiducial volume does not include the first layer. Figure 4.5 shows the $X$ (top left), $Y$ (top right), and $Z$(bottom left) components of the track starting point for all selected tracks passing the fiducial cut and the number of events in FGD1 and FGD2 (bottom right). The T2K beam axis passes underneath the ND280, meaning that the shape of the events in $Y$ is expected as the event rate is higher at the bottom of the detector.

A momentum cut is applied to the track requiring that $p > 50$ MeV/c in order

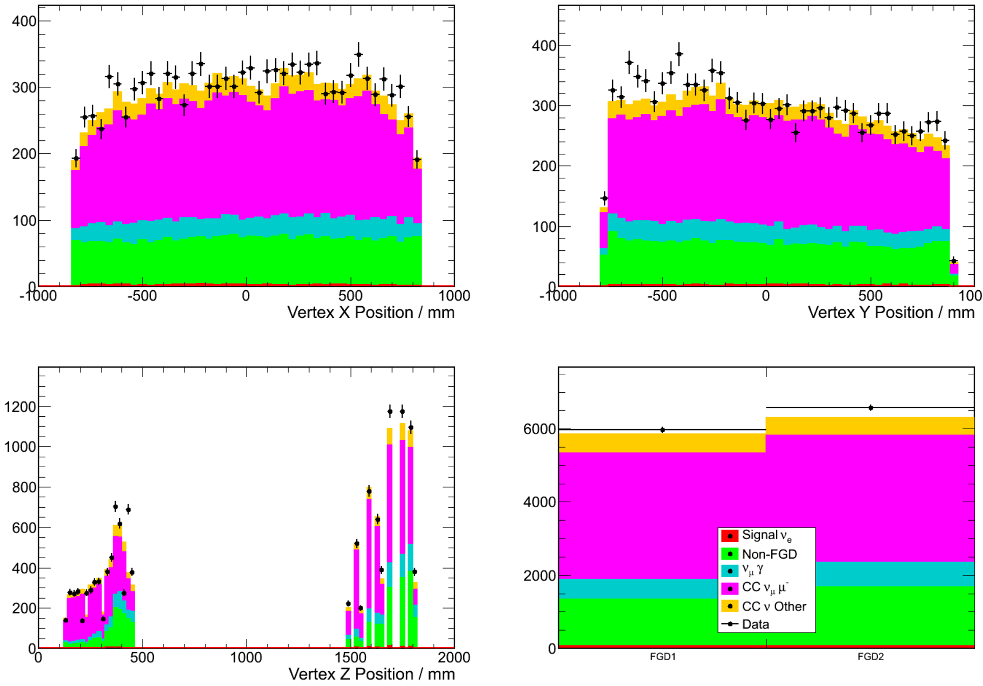

Figure 4.5: The distribution of events in the FGD fiducial volume for data and simulation. The three spacial coordinates, $X$, $Y$ and $Z$ are shown in the top left, top right and bottom left plots respectively. The bottom right plot shows the total number of events reconstructed in the fiducial volume of FGD1 and FGD2.

to reject the very low momentum events. Approximately 2 % of signal events have a momentum less than 50 MeV/c and the very low momentum range is susceptible to noise and delta rays in the TPC that can cause differences between data and the simulation.

**Track Quality Cuts**

Three cuts are applied to the selected track to ensure that the track is of good quality:

i The track is required to be reconstructed as travelling downstream from the interaction point, such that the reconstructed start position is at a smaller $Z$ coordinate value than the end position, where the start and end positions are defined by time. Neutrino interactions predominantly produce particles travelling in the downstream direction so the cut is applied to reject any backward going events.

ii The track is then checked for the number of hits in the TPC. It is required that the track contains a TPC segment with at least 36 hits, ensuring that the momentum can be measured accurately. The value of 36 hits is used as it requires the particle to have traversed a distance equal to an entire MicroMegas readout board.

iii Finally, an explicit cut on the track momentum uncertainty is applied to ensure that the momentum of the selected track is well defined:

$$\frac{\sigma_p}{p} \leq 1 \tag{4.3}$$

A comparison of the momentum resolution for data and simulation after the application of the cut, normalised to POT, is shown in Figure 4.6. Very good agreement is seen between data and simulation and the majority of tracks have momentum uncertainties of less than 20 %.

### 4.4.4 Particle Identification (PID)

The global reconstruction objects do not have an associated PID. The analyser is free to decide which PID information to use and the way in which to combine it. In this analysis, three sources of PID information were considered from the following detectors: TPC2, TPC3 and DsECal.

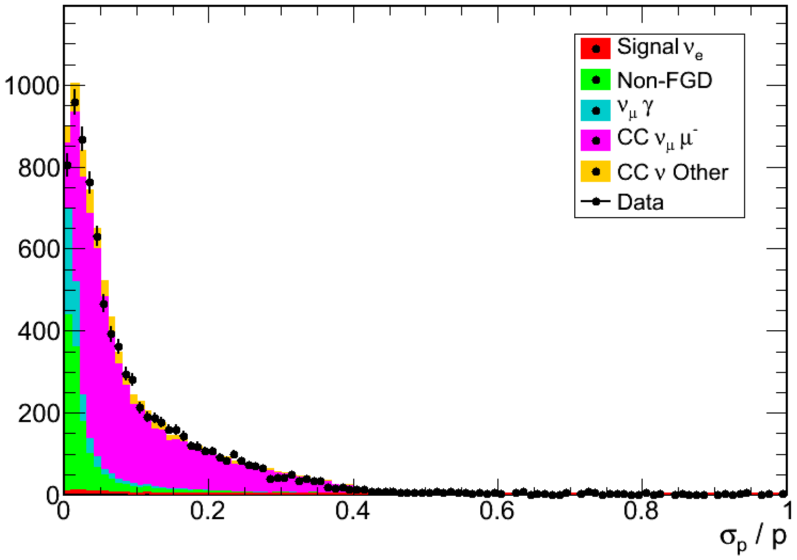

Figure 4.6: A comparison of the fractional uncertainty on the TPC momentum measurement for data and simulation, normalised to the POT of the data, for all tracks passing the criterion defined in Equation 4.3.

A given track must have at least one TPC PID and may also have a DsECal PID. The TPC PID information is used if the number of hits in the TPC is greater than 36 and the DsECal component is used if it has more than 10 hits. The Barrel ECal, although present in the Run 2 data, was not considered to be physics-ready as it was not yet fully calibrated so no PID information was used from the Barrel ECal.

### TPC PID

The TPC uses a measurement of the energy loss per unit length that is truncated to the central 70 % of values, $C_T$, to provide information about particle type. Using the expected $C_T$ values for different particle hypotheses allows for the construction of pull variables, $P_h$, in the following way for each particle hypothesis:

$$P_h = \frac{C_{T,measured} - C_{T,expected}}{\sigma_{C_{T,expected}}} \tag{4.4}$$

The $P_h$ distribution for particles of type $h$ follow the Normal distribution given that $C_T$ is Gaussian distributed. This means that an ideal particle of type $h$ should have a value of $P_h = 0$. The pulls are calculated for 5 particle hypotheses: electron, muon, pion, proton and kaon. Figure 4.7 shows the pull distributions for the muon (top), pion (middle) and electron (bottom) hypotheses. The muon and pion pulls are used to reject background events and the electron pull is used to select the electrons. The cut values used are summarised below:

- $|P_\mu| > 2.5$
- $-1.0 < P_e < 2.0$
- $|P_\pi| > 2.0$

Figure 4.8 shows the electron selection efficiency for different cut values (top) and the two bottom plots show the probability of identifying a muon as an electron using the cut values shown in the top plot. The decision was made to use the above cuts as they give a balance between electron selection efficiency and muon rejection. The selection range in $P_e$ is asymmetric due to the large number of muons in the region $-2 < P_e < -1$. It is important to note that each pull distribution should only be used to either select or reject particles of the given type of the pull distribution hypothesis. For example, applying a cut to the muon pull in order to select electrons can cause a large momentum bias due to the behaviour of the underlying $\frac{dE}{dx}$ curves. The pion pull cut is applied to reject low momentum pions that are not rejected by the muon pull cut. No tracks are selected in the momentum range 110 MeV/c to 150 MeV/c because the energy loss curves for electrons and muons cross in this region. An electron candidate would not pass the PID cut because it would have a pull of zero for both the electron and muon hypotheses.

### DsECal PID

The reconstruction in the ECal provides a single PID output parameter, $D$, that distinguishes between track-like and shower-like objects, described in detail in Section 3.7. Figure 4.9 shows the DsECal track-shower discriminator for data and simulation for all tracks passing the cuts up until the PID. The agreement between data and simulation is fairly good, but the track-like peak in data is lower than the simulation peak, as also shown in Chapter 3 in Figure 3.12. The showering particles show better agreement and a value of $D < 0.2$ was used to select electrons in the DsECal as it maximised the figure of merit $\frac{S}{\sqrt{B}}$, where $S$ is the number of signal events and $B$ is the number of background events.

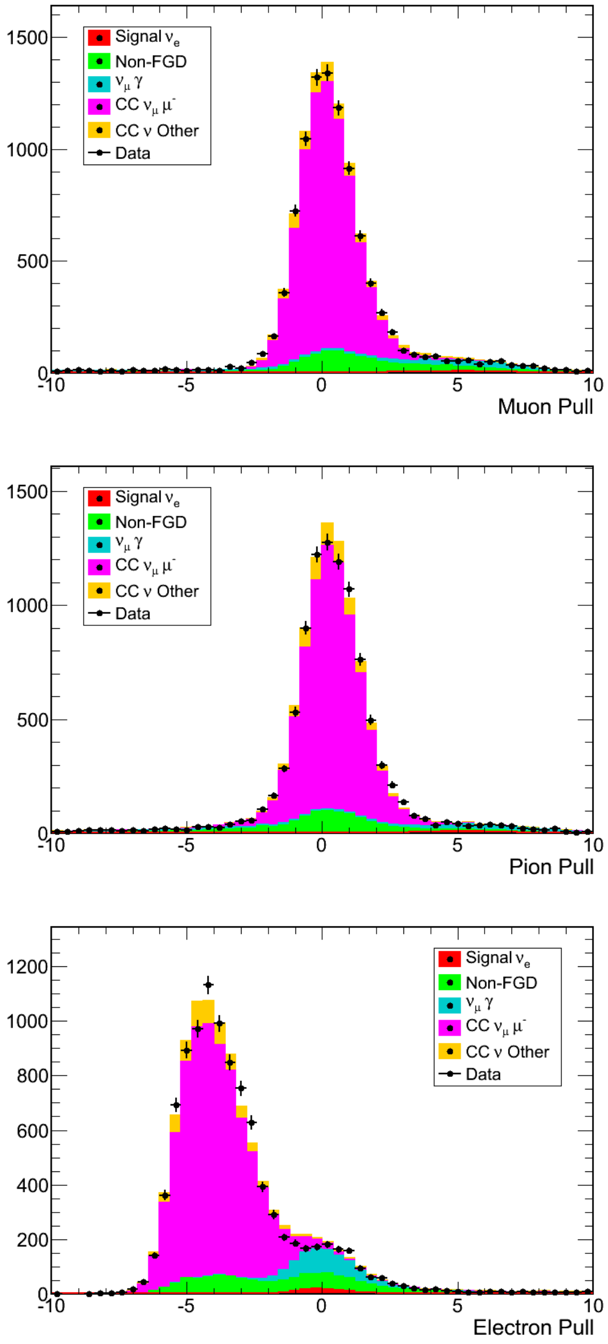

Figure 4.7: TPC $C_T$ pull distributions for data and simulation for all particles passing the prior selection cuts for different hypotheses: muon pull (top), pion pull (middle) and electron pull (bottom). In all plots the simulation has been scaled to the data POT and all events shown are those that passed the selection criteria up to the PID.

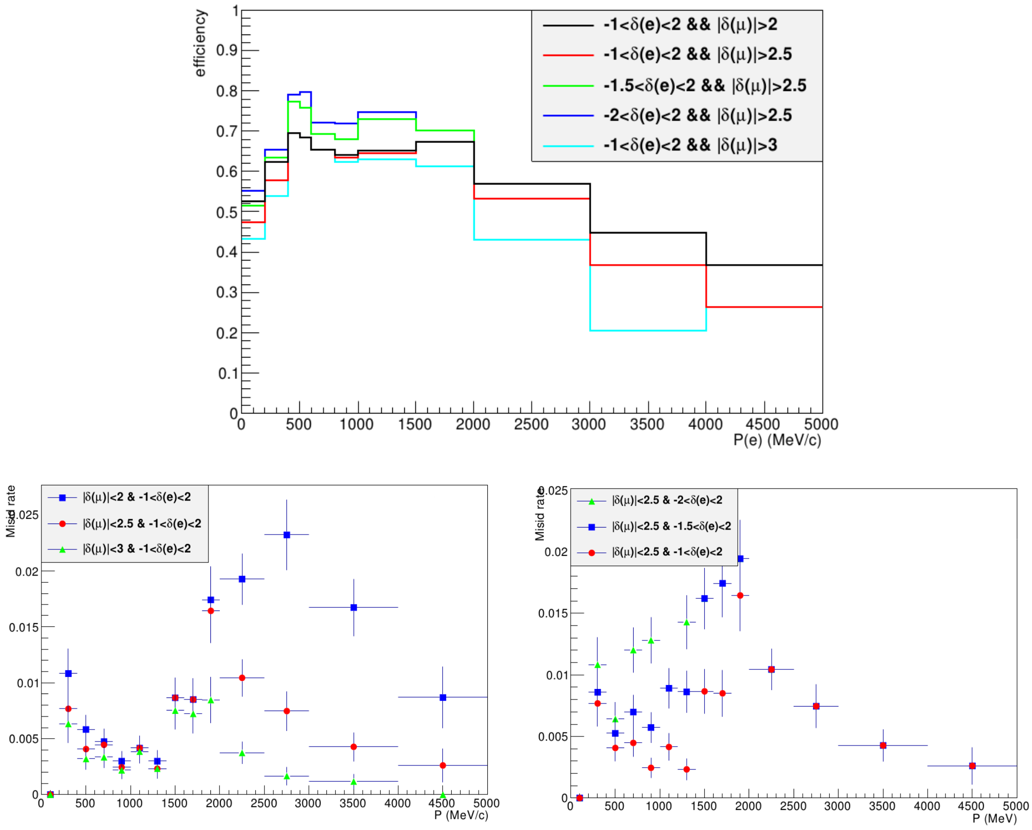

Figure 4.8: Top: the electron selection efficiency in the TPC for different values of muon and electron pull cuts as a function of momentum. Bottom: The muon misidentification probability as a function of momentum for a fixed electron pull cut (left) and a fixed muon pull cut (right). The red points in each figure are the chosen cut values. Figures adapted from [79].

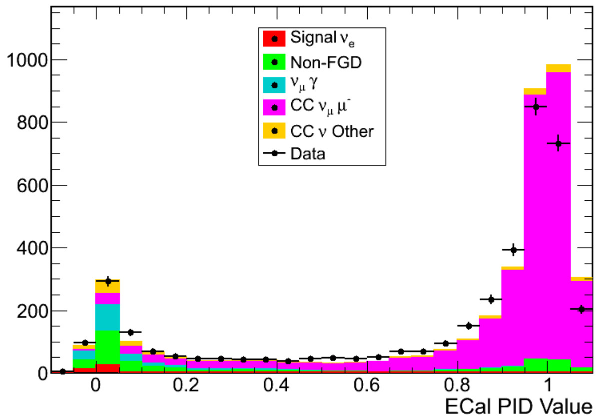

Figure 4.9: The DsECal track-shower discriminator shown for data and simulation after the application of the prior cuts. The simulation sample was scaled to the same POT as the data.

### Combining Detector Information

Tracks can have up to three sources of PID information in the analysis that are combined to form a global PID. The subdetector PIDs are calculated by applying the cuts for either TPC or DsECal PID to determine whether the object is an electron or not. The boolean PID decisions from TPC2, TPC3 and the DsECal are then combined in the following way:

- 3 PIDs:
  - All 3 PIDs agree: The PID becomes the global PID.
  - If 2 PIDs agree: The agreed PID becomes the global PID.
  - Otherwise, global PID is not defined.
- 2 PIDs:
  - If they agree, use as the global PID.
  - If not in agreement, global PID is not defined.
- 1 PID from TPC2 or TPC3: Use as the global PID. [2]

The percentages of events in data and simulation falling into the different PID combinations are summarised in Table 4.4 and show that agreement is seen between data and simulation in all of the PID categories.

---

[2] The requirement for all selected tracks to have at least 36 hits in either TPC2 or TPC3 means that all tracks have at least one TPC PID, meaning that the single PID can not be the DsECal PID information.

| Number of PIDs | Detectors | Percentage of Events | |
|---|---|---|---|
| | | Data | Simulation |
| 1 | TPC2 | $40.0 \pm 2.8$ | $42.7 \pm 0.8$ |
| | TPC3 | $33.7 \pm 2.7$ | $31.1 \pm 0.8$ |
| 2 | TPC3 + DsECal | $19.7 \pm 2.2$ | $20.4 \pm 0.7$ |
| | TPC2 + TPC3 | $1.3 \pm 0.6$ | $1.3 \pm 0.2$ |
| 3 | TPC2 + TPC3 + DsECal | $5.4 \pm 1.3$ | $4.6 \pm 0.4$ |

Table 4.4: The percentage of events in data and simulation that fall into the different PID categories. The given uncertainties are statistical only.

#### Performance

The PID of the track is calculated as described above and required to be electron-like for an object to be selected. The PID selects both electrons and positrons as it does not consider the charge of the particle because all selected particles were initially selected as being reconstructed as negative. The PID algorithm therefore purifies the sample in both electrons and positrons, increasing the purity with respect to those particles from 15 % to 89 %.

### 4.4.5 Background Vetoes

After the application of the PID cut, the selection is pure with respect to electrons and positrons. The cuts described in the following section aim to purify the sample with respect to electrons from CC $\nu_e$ interactions by rejecting events from the sources of background that produce electrons and positrons discussed in Section 4.4.1.

#### Veto for Electrons from Photon Conversions

Selecting electron-like particles only purifies the sample in terms of particle type, it does not address the large background coming from electrons from photon conversions. The photons can come from a variety of processes and the photons can produce an $e^-e^+$ pair.

The fact that the invariant mass of a photon conversion to an electron-positron pair is zero can be used as a method to identify the background events. The invariant mass is calculated with all tracks in the event that pass the following criteria:

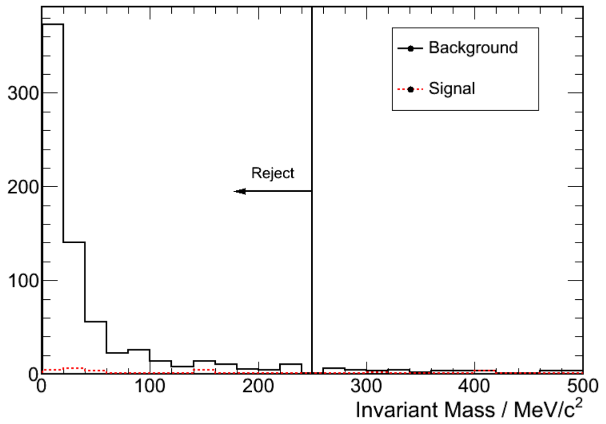

Figure 4.10: A plot showing the minimum invariant mass of the selected electron-candidate track with an electron-like track starting within 10 cm of the candidate track vertex point. The background component in black has a clear peak at low values such that events with and invariant mass greater than 250 MeV/c$^2$ are selected.

- Starting position is within 10 cm of the starting point of the candidate track.
- Opposite charge to the electron-candidate track.
- The track passes a loose electron-like PID in the TPC: The electron pull $P_e$ is in the range $-3 < P_e < 3$.

The invariant mass is calculated using the assumption that both tracks are particles with the electron mass. Figure 4.10 shows the distribution of the invariant mass for all electron-candidates with a second track passing the above criteria. Events that do not have any other tracks at the vertex do not have an assigned invariant mass and hence do not appear in the figure. Events with invariant mass greater than 250 MeV/c$^2$ are selected for further analysis. The position of the cut was set at the value that gave the best value of $\frac{S}{\sqrt{B}}$. Any events where the electron candidate track did not have any other tracks passing the above criteria are not considered by the invariant mass cut.

The spectrum of events rejected by the invariant mass cut is shown in Figure 4.11 for simulation and data. As expected, the majority of events rejected by the invariant mass cut are electrons or positrons coming from $\gamma$ conversions. The fraction of all events rejected in the simulation coming from the $\nu_\mu\gamma$ background category is 79 % and the total fraction of background events rejected is 17 %.

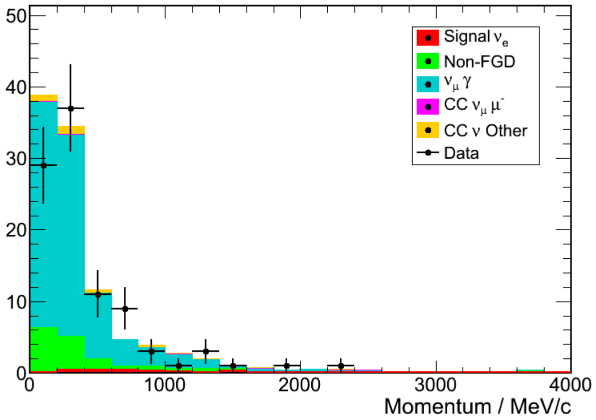

Figure 4.11: The number of events rejected by the invariant mass cut as a function of momentum and shown for simulation and data, scaled to the data POT.

### Detector Vetoes

A neutrino interaction in the FGD fiducial volume should be a clean event, meaning that the detectors upstream of the interaction point should not contain any tracks within the same time bunch as the selected lepton track. Other electron-like tracks selected in the FGD fiducial volume are likely to have been caused by interactions upstream of the FGDs. These events can be vetoed by requiring that no tracks are reconstructed in the upstream detectors within the time bunch. A veto is applied to the following subdetectors: P0D, TPC1, and the combination of FGD1 + TPC2 if the selected electron candidate track starts in FGD2.

The events rejected by the different vetoes are shown in Figure 4.12 for data and simulation. The P0D veto is shown in the top left, the TPC1 veto in the top right and the FGD1 + TPC2 veto in the bottom left. The plot in the bottom right contains the sum of the other three plots, showing the rejection of events for all of the detector vetoes. The combined effect of the detector vetoes is to reject 42 % of the background events remaining after the invariant mass cut with the loss of only 5 % of signal events.

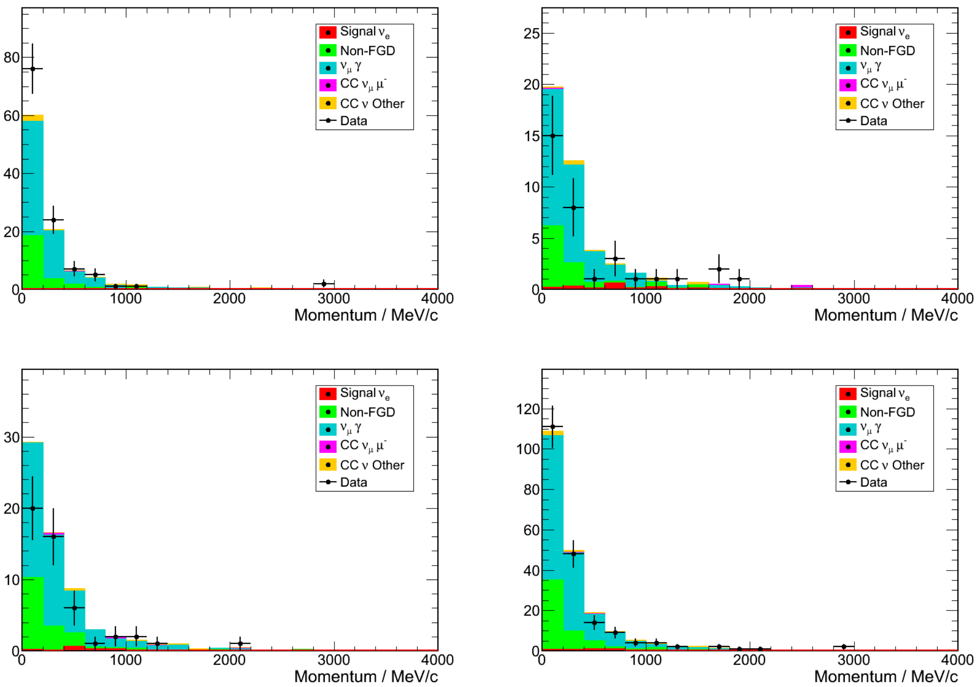

Figure 4.12: Momentum spectra of events rejected by the detector vetoes: P0D (top left), TPC1 (top right), TPC2 and FGD1 (bottom left) and the combination of the three vetoes (bottom right). The number of simulation events is scaled to the same POT as the data.

### 4.4.6 Summary of Selection Criteria

The summary of the selection criteria applied to the highest momentum negative track in each bunch is given below:

i Require that the starting point of the track is within the FGD fiducial volume.

ii Apply a momentum cut to select tracks with momentum $p > 50\,\mathrm{MeV/c}$.

iii Require than the track contains at least 36 hits in at least one of the TPCs.

iv Accept only forward-going tracks, since tracks should be boosted in the forward direction.

v Require that the uncertainty on the momentum measurement is less than 100 %.

vi Require an electron-like response from the PID.

vii If other tracks are present at the vertex, require that invariant mass $m > 250\,\mathrm{MeV/c^2}$.

viii Veto event if there are objects in the P0D.

ix Veto event if there are objects in TPC1.

x Veto events with the vertex in FGD2 if there is activity in TPC2 or FGD1.

### 4.4.7 Results

The efficiency of the selection applied to the simulation is shown on the left plot in Figure 4.13 as a function of true neutrino energy where the efficiency $\epsilon$ is defined as:

$$\epsilon = \frac{\text{Number of selected CC } \nu_e \text{ events}}{\text{Total number of CC } \nu_e \text{ interactions in the FGD fiducial volume}} \tag{4.5}$$

The right plot in Figure 4.13 shows the purity of the simulation selection as a function of the selected lepton momentum, showing that the low momentum region is background dominated and above about 300 MeV/c the purity rises sharply and levels off at about 50 % above 800 MeV/c. Table 4.5 gives a summary of the number of events selected in data and simulation for all of the selection criteria. The efficiency and purity of the simulation is also shown, with the total average efficiency of the selection of CC $\nu_e$ events equal to 37 % with a purity of 20 %.

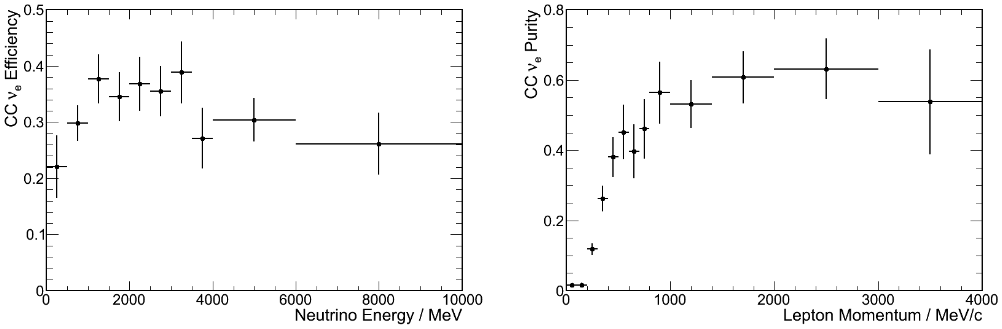

Figure 4.13: The CC $\nu_e$ efficiency (left) plotted as a function of true neutrino energy and purity (right) plotted as a function of lepton momentum from the simulation shown with statistical uncertainties.

Table 4.5 also shows that the total number of events selected with momenta in the range 50 MeV/c to 4.0 GeV/c from the data was

$$N_{data} = 315 \pm 18(stat)$$

corresponding to a ratio between the number of data and simulated events of

$$\frac{N_{data}}{N_{sim}} = 0.92 \pm 0.06(stat)$$

after the application of all the selection criteria, where the quoted uncertainty is statistical only. The final selection is shown in Figure 4.14 and compares the data to the simulation, broken up between signal and the background categories. Within the statistical uncertainties shown, a good level of agreement is seen between data and simulation.

## 4.5 Positive Analysis

An additional analysis, the Positive Analysis, was performed in order to constrain the Non-FGD and $\nu_\mu\gamma$ backgrounds in the CC $\nu_e$ analysis. The Non-FGD and $\nu_\mu\gamma$ backgrounds consist primarily of particles produced from $\gamma$ conversions meaning that an equal number of electrons and positrons are created. The positive analysis should therefore contain analogous components, selecting on the positrons instead of the electrons.

The positive analysis proceeds in exactly the same way as the CC $\nu_e$ analysis but the selection is made on the highest momentum track with positive charge. The

| Cut | $N_{data}$ | $N_{sim}$ |  |  | Efficiency | Purity | $\frac{N_{data}}{N_{sim}}$ |
|---|---|---|---|---|---|---|---|
|  |  | Total | Signal | Bkg |  |  |  |
| i | $12539 \pm 112$ | 12155 | 122 | 12033 | 0.69 | 0.01 | $1.03 \pm 0.01$ |
| ii | $10942 \pm 105$ | 10813 | 119 | 10694 | 0.66 | 0.01 | $1.01 \pm 0.01$ |
| iii | $9020 \pm 95$ | 9088 | 111 | 8977 | 0.62 | 0.01 | $0.99 \pm 0.01$ |
| iv | $8717 \pm 93$ | 8885 | 110 | 8774 | 0.62 | 0.01 | $0.98 \pm 0.01$ |
| v | $8663 \pm 93$ | 8841 | 110 | 8731 | 0.61 | 0.01 | $0.98 \pm 0.01$ |
| vi | $609 \pm 25$ | 648 | 76 | 572 | 0.41 | 0.12 | $0.94 \pm 0.04$ |
| vii | $513 \pm 23$ | 546 | 73 | 473 | 0.39 | 0.13 | $0.94 \pm 0.05$ |
| viii | $397 \pm 20$ | 449 | 72 | 377 | 0.39 | 0.16 | $0.88 \pm 0.05$ |
| ix | $364 \pm 19$ | 406 | 71 | 335 | 0.38 | 0.17 | $0.90 \pm 0.05$ |
| x | $315 \pm 18$ | 342 | 69 | 273 | 0.37 | 0.20 | $0.92 \pm 0.06$ |

Table 4.5: Summary of the number of events selected in data and simulation by the analysis for lepton momenta up to 4 GeV/c where the simulation values have been scaled to the same number of POT as the data. Uncertainties given are purely statistical.

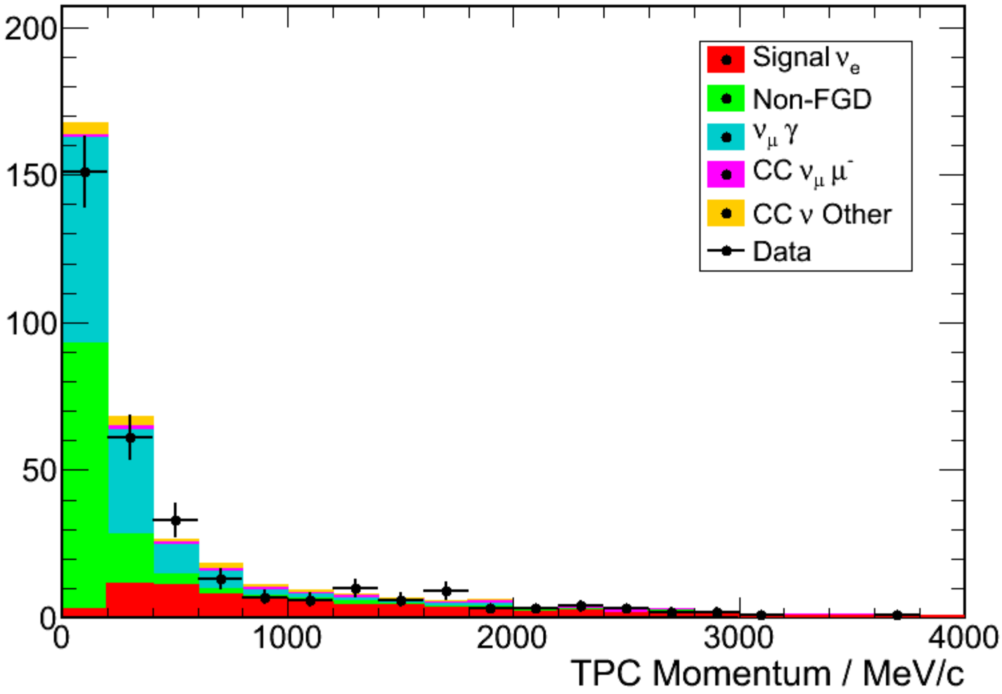

Figure 4.14: The electron-candidate momentum distribution after all cuts have been applied comparing data and simulation. The uncertainties are statistical and the simulation has been scaled to match the data POT.

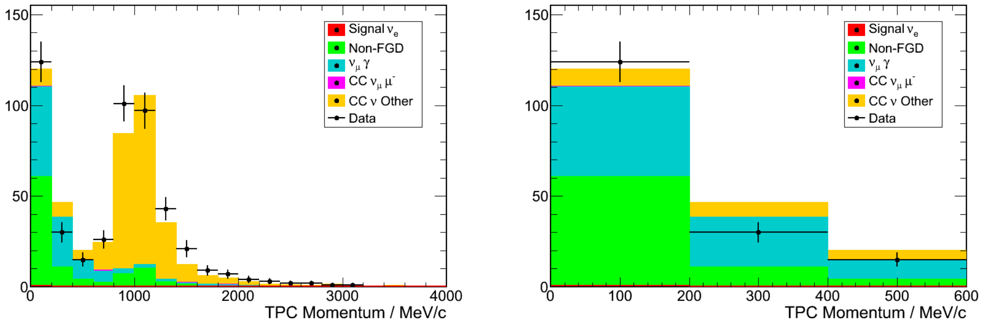

Figure 4.15: The selected lepton momentum for events selected by the positive analysis for data and simulation for momenta up to 4.0 GeV/c (left) and up to 600 MeV/c (right).

positive analysis should provide a similar sample to the CC $\nu_e$ analysis but without the CC $\nu_e$ interactions and a negligible contribution from CC $\bar{\nu}_e$ events, because the $\bar{\nu}_e$ flux is an order of magnitude smaller than the $\nu_e$ flux.

Figure 4.15 shows the lepton momentum distribution plotted from 50 MeV/c to 4.0 GeV/c on the left and on the right, a zoomed in version from 50 MeV/c to 600 MeV/c. It is clear that above 600 MeV/c there is a large contamination in the sample from the $\nu_\mu$-other background. The peak primarily consists of protons because the proton and electron energy loss curves in the TPC cross at about 1 GeV/c, meaning that the TPCs can not separate electrons and protons in this region. This does not present a problem for constraining the Non-FGD and $\nu_\mu\gamma$ backgrounds because these events occur primarily in the low momentum region. It was therefore decided to use the positive analysis only in the range 50 MeV/c to 600 MeV/c.

Table 4.6 provides a summary of the positive analysis on a cut-by-cut basis for the lepton momentum range 50 MeV/c to 600 MeV/c, where the cuts are those defined for the CC $\nu_e$ analysis in Section 4.4.6. The final number of events selected in the positive analysis is:

$$N^{pos} = 169 \pm 13(stat)$$

corresponding to a ratio between data and simulation of

$$\frac{N^{pos}_{data}}{N^{pos}_{sim}} = 0.91 \pm 0.08(stat)$$

that is consistent within the statistical uncertainty with the ratio of data and simulation obtained in the negative analysis.

| Cut | $N_{data}$ | $N_{sim}$ | $\frac{N_{data}}{N_{sim}}$ |
|---|---|---|---|
| i | $8813 \pm 94$ | 7505 | $1.17 \pm 0.01$ |
| ii | $6071 \pm 78$ | 6051 | $1.00 \pm 0.01$ |
| iii | $4584 \pm 68$ | 4805 | $0.95 \pm 0.02$ |
| iv | $4510 \pm 67$ | 4702 | $0.96 \pm 0.02$ |
| v | $4505 \pm 67$ | 4696 | $0.96 \pm 0.02$ |
| vi | $388 \pm 20$ | 405 | $0.96 \pm 0.05$ |
| vii | $319 \pm 18$ | 327 | $0.98 \pm 0.06$ |
| viii | $246 \pm 16$ | 253 | $0.97 \pm 0.07$ |
| ix | $221 \pm 15$ | 228 | $0.97 \pm 0.07$ |
| x | $169 \pm 13$ | 186 | $0.91 \pm 0.08$ |

Table 4.6: Summary of the number of events selected in data and simulation by the positive analysis for events with lepton momentum in the range 50 MeV/c to 600 MeV/c where the simulation values have been scaled to the same number of POT as the data. Uncertainties given are statistical only.

## 4.6 Signal Extraction

A binned maximum likelihood fit was developed using the RooFit[80] package in ROOT to extract the number of signal events from the electron-candidate momentum distribution. The fit was designed to simultaneously fit the momentum spectra from the negative and positive analyses, such that the positive analysis is used as a control region to help constrain the low momentum backgrounds in the negative analysis.

The selected particle momentum distribution from the simulation for the negative analysis was divided into four different interaction types to be used as template probability distribution functions (PDFs) for the likelihood fit. The four categories are given below:

- Signal: true electrons from CC $\nu_e$ interactions in the FGD fiducial volume.
- Non-FGD and $\nu_\mu\gamma$: a combination of the backgrounds as described separately in Section 4.4.1.
- $\nu_\mu\mu$: misidentified $\mu$ from $\nu_\mu$ interactions.
- $\nu_\mu$-other: misidentified $p$ and $\pi$ from $\nu_\mu$ interactions.

The Non-FGD and $\nu_\mu\gamma$ categories were combined due to the large correlation between the samples. Approximately 73 % of the Non-FGD category are electrons or positrons from $\gamma$ conversions outside of the FGD fiducial volume. This gives rise to

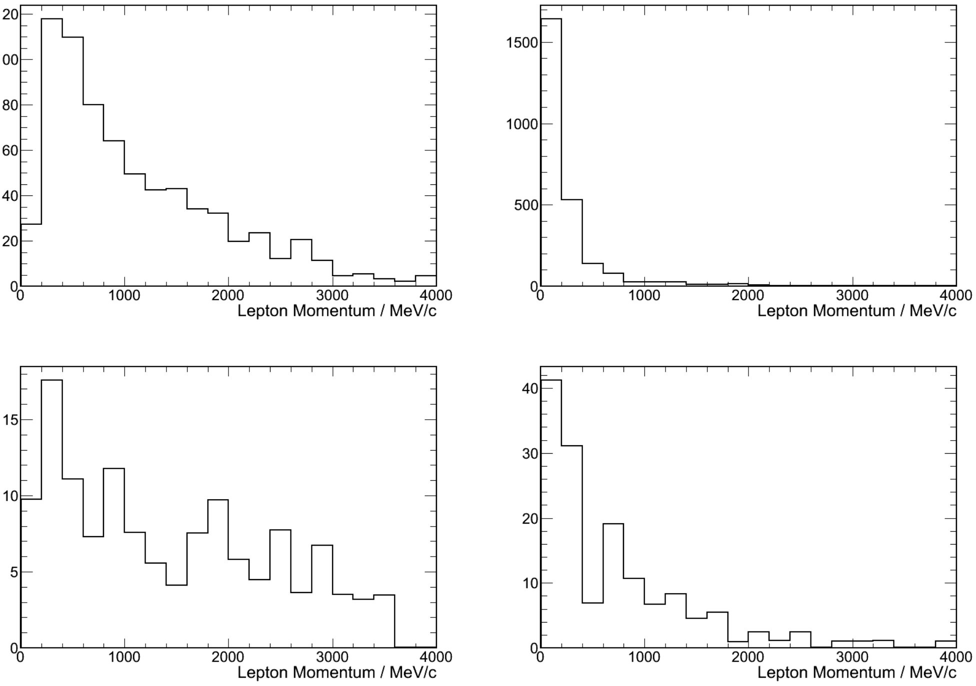

Figure 4.16: The four histogram templates for the likelihood fit from the simulation: Signal $\nu_e$ electrons (top left), Non-FGD and $\nu_\mu$ $\gamma$ (top right), $\nu_\mu \mu$ (bottom left) and $\nu_\mu$-other (bottom right).

a large correlation between the samples because the momentum spectra of $\gamma$ conversion electrons and positrons should be similar regardless of where the $\gamma$ conversion occurred.

The template histograms were produced as binned histograms using 200 MeV/c bins covering the range from 0.0 GeV/c to 4.0 GeV/c and are shown in Figure 4.16. The binning was chosen in order to maximise the number of bins whilst ensuring that there were no empty bins when considering the sum of the four templates. The $\nu_\mu \mu$ and $\nu_\mu$-other samples have fairly low statistics so their normalisation was fixed in the fit to the number of events expected in the simulation given a sample size equal to that of the data. The effect of fixing the normalisation was considered as a systematic uncertainty, described in Section 4.7.2.

The positive analysis simulation was divided up into two interaction type templates for all events with $p < 600$ MeV/c as listed below:

- Non FGD and $\nu_\mu \gamma$ combined.
- Other: Combination of all other selected events, predominantly $p$ and $\pi$ from $\nu_\mu$ interactions.

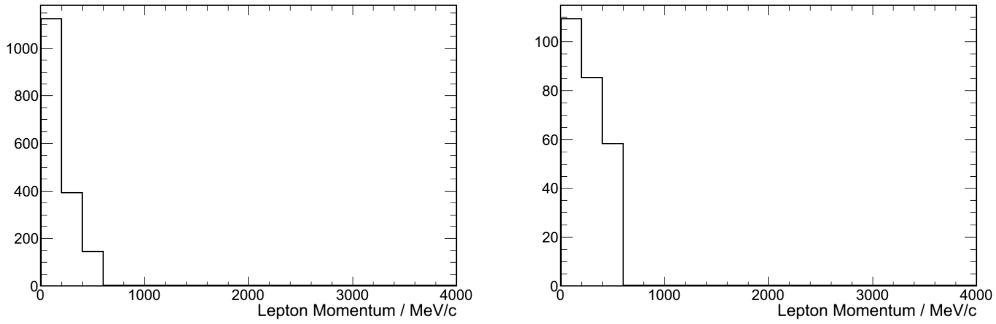

Figure 4.17: The two histogram templates for the likelihood fit from the simulation for the positive analysis: Non FGD and $\nu_\mu$ $\gamma$ (left) and all other interaction types (right).

The histograms contain three 200 MeV/c bins and are shown in Figure 4.17. The combined Non-FGD and $\nu_\mu$ $\gamma$ sample is analogous to the component in the negative analysis and hence provides additional data points to constrain the background. The $\nu_\mu$-other category in the positive sample is not comparable to the $\nu_\mu$-other component in the negative analysis due to the abundance of protons in the positive selection. The $\nu_\mu$-other component for the positive analysis was fitted with a fixed normalisation value in the same way as the $\nu_\mu\mu$ and $\nu_\mu$-other components of the negative analysis.

The overall normalisation scale of the positive analysis is lower than the negative analysis, so a weight parameter $w$ was used to link the number of Non-FGD and $\nu_\mu\gamma$ background events in the negative ($N^-_{bkg}$) and positive ($N^+_{bkg}$) analyses:

$$N^+_{bkg} = wN^-_{bkg} \tag{4.6}$$

where $w$ was allowed to float in the fit in the range 0 to 1.

### 4.6.1 Toy Simulation Studies

Ten thousand toy simulation samples were generated from the simulation histogram templates with the number of events in the samples matched to the number of events measured in data: 315 and 169 for the negative and positive analyses respectively. Fits were made to the generated samples using the standard simulation templates to check the stability of the fitting procedure and to check for biases in the extracted number of signal events.

The left plot in Figure 4.18 shows the number of extracted signal $\nu_e$ events $N(\nu_e)$ for the 10,000 toy samples. The plot on the right of Figure 4.18 shows the corresponding distribution for the combined Non-FGD and $\nu_\mu\gamma$ background

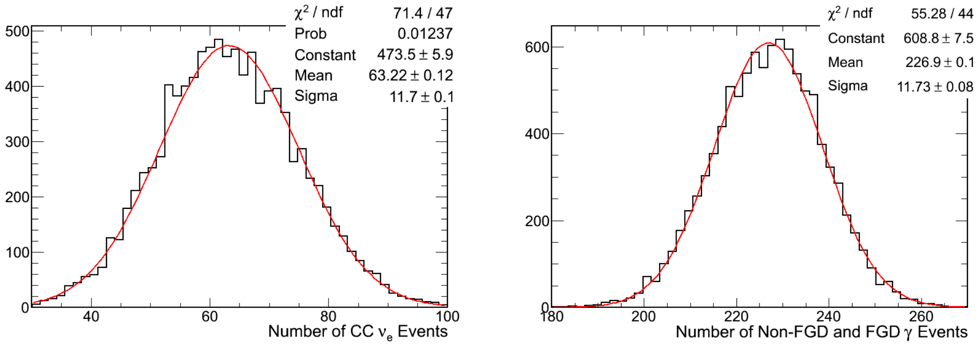

Figure 4.18: Histograms of the number of signal (left) and combined Non-FGD and $\nu_\mu\gamma$ background (right) events extracted from 10,000 toy simulation fits. The expected numbers of events were 63.4 and 226.8 respectively.

| Event Type | Expected | Measured |
|---|---|---|
| Signal | 63.4 | 63.2 ± 0.1 |
| Combined Background | 226.8 | 226.9 ± 0.1 |

Table 4.7: Number of events expected and measured from the toy simulation studies for the $\nu_e$ signal and the combined Non-FGD and $\nu_\mu\gamma$ background. The number of expected events was calculated by scaling the total number of simulation events to the actual number of events measured in data: 315 and 169 for the negative and positive analyses respectively.

component. Table 4.7 gives a summary of the expected number of events for the signal and combined background categories and the values measured from the toy simulation. The fit returns the expected number of events for both components.

### 4.6.2 Results

The electron-candidate momentum distribution from the combined Run 1 and Run 2 data was fitted using the simulation templates. The relative sizes of the fitted components are shown compared to data in Figure 4.19. The top plot shows the negative analysis and the bottom plot shows the positive analysis. Comparing the negative analysis fit with Figure 4.14 shows that the fit has reduced the Non-FGD & $\nu_\mu\gamma$ component and slightly increased the signal component. Table 4.8 summarises the number of events extracted from the fit and shows that the number of signal events measured was

$$N(\nu_e) = 67.7 \pm 12.9(stat)$$

| Sample | Category | Measured Value | Data/Simulation Ratio |
|---|---|---|---|
| Negative | Signal | $67.7 \pm 12.9$ | $0.983 \pm 0.191$ |
| | Non-FGD & $\nu_\mu\gamma$ | $223.1 \pm 17.5$ | $0.906 \pm 0.073$ |
| | $\nu_\mu\mu$ | 11.7 (fixed) | 1 (fixed) |
| | $\nu_\mu$ Other | 13.0 (fixed) | 1 (fixed) |
| Positive | Non-FGD & $\nu_\mu\gamma$ | $148.6 \pm 20.9$ | $0.921 \pm 0.132$ |
| | Other | 22.3 (fixed) | 1 (fixed) |

Table 4.8: Number of events measured for the $\nu_e$ signal and the different background components from a fit to the Run 1 and Run 2 data.

with a corresponding ratio between data and simulation of

$$\frac{N(\nu_e)_{Data}}{N(\nu_e)_{Sim}} = 0.983 \pm 0.191(stat)$$

showing that agreement is seen between data and simulation within the statistical uncertainty given. The number of events and the data to simulation ratio for the other components are also given in Table 4.8. It also shows that there is a small excess of the Non-FGD & $\nu_\mu\gamma$ events in the simulation. All uncertainties are purely statistical at this stage and the study of systematic uncertainties is presented in Section 4.7.

## 4.7 Study of Systematics

The study of systematic uncertainties is broken down into uncertainties coming from four different sources:

i Detector systematics

ii Simulation statistics

iii Beam flux

iv Cross-sections

### 4.7.1 Detector Systematics

The detector systematic uncertainties arise from differences between the data and simulation, and effectively mean that there is an efficiency difference. These uncertainties were studied by determining the data and simulation difference and then the difference was accounted for by changing the simulation. For example, if a process

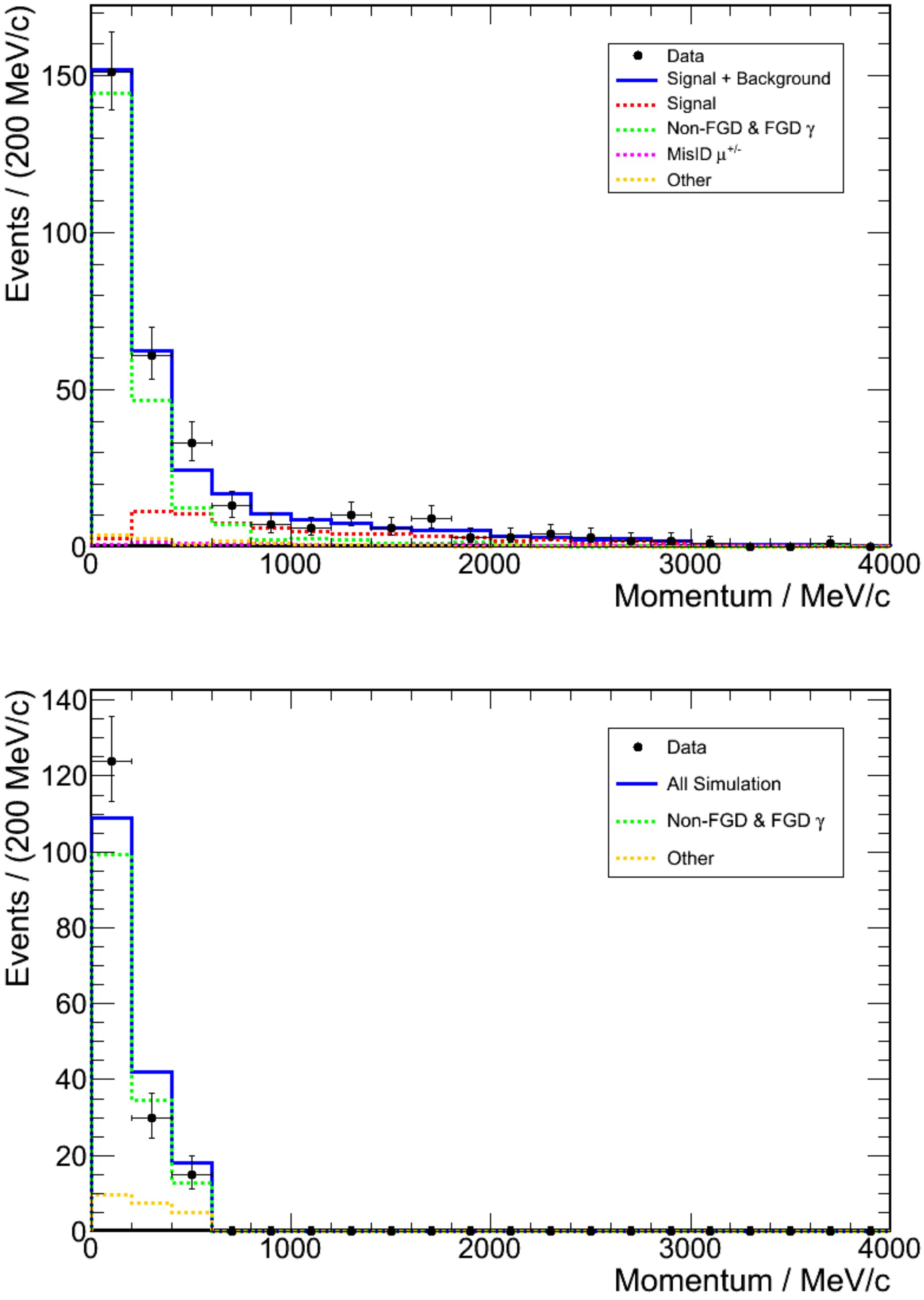

Figure 4.19: The result of fitting the simulation template histograms to the Run 1 and Run 2 data for the negative (top) and positive (bottom) analyses.

was found to be more efficient in the simulation by 1 % compared to the data then a random 1 % of simulation objects were rejected from the analysis. The random rejection procedure was then repeated a number of times to produce a series of simulation samples that were used to fit the data. The number of signal events extracted from the data for each sample was plotted and fitted with a Gaussian. The difference in the mean of the Gaussian and the nominal number of events extracted from the fit provides the systematic uncertainty arising from the process.

### Track Quality Cuts

The three track quality cuts discussed in Section 4.4.3 are applied to ensure that the reconstructed object is well defined. The effect of the cuts on the analysis was studied by turning off all three of the cuts and re-running the simulation to produce a simulation sample without quality cuts. The data were then fitted using the standard likelihood fit and the systematic uncertainty due to the quality cuts was measured by the change in the number of extracted events:

$$\delta N(\nu_e) = \pm 0.32$$

### Momentum Resolution

The momentum resolution was studied in data and simulation in [81] for muons. Using the assumption that the resolution does not differ for electrons, the momentum resolution was found to be better in simulation than in data. The difference vaired between TPC2 and TPC3 and was accounted for by increasing the simulated momentum resolution by the factor $(1 + S)$ for the following values of $S$:

$$S_{TPC2} = (2.8 \pm 0.6) \times 10^{-5} \quad \text{and} \quad S_{TPC3} = (4.3 \pm 0.7) \times 10^{-5}$$

The small values of the smearing meant that the momentum resolution difference had a negligible effect on the analysis, and hence no systematic uncertainty was assigned due to the difference in momentum resolution. This uncertainty was expected to be negligible because the momentum resolution was shown to agree well between data and simulation in Figure 4.6.

### TPC Efficiency

The TPC reconstruction efficiency was studied in [82] and it was found that there was a difference of 2.2 % between data and simulation. The efficiency was actually smaller in the simulation than in data but it is not trivial to increase the efficiency in the simulation. For this reason, the difference was accounted for by rejecting a random 2.2 % of tracks from the simulation based on the assumption that an increase of 2.2 % would produce an analogous shift in the number of extracted signal events in the opposite direction. The standard process was performed to produce 100 simulation datasets that were fitted to the data to give a systematic uncertainty of:

$$\delta N(\nu_e) = \pm 0.14$$

### TPC-FGD Association

The difference in the efficiency for associating tracks between the TPC and FGD using the global reconstruction for data and simulation was found to be 2.1 %[79]. As stated with the TPC efficiency systematic, the efficiency measured for associating TPC and FGD objects was lower for simulation and hence a similar process to the one described in the previous section was performed and the systematic uncertainty was measured to be:

$$\delta N(\nu_e) = \pm 0.13$$

### TPC-ECal Matching and Reconstruction Efficiency

The analyses used objects that pass from TPC3 into the DsECal and the individual objects in the subdetectors are matched together by the global reconstruction. The efficiency to reconstruct an object in the DsECal given a track that exited TPC3 in a position where an ECal object would be expected was studied in data and simulation. The details of the study are given in [79] and the difference in efficiency of data compared to simulation was found to be

$$\epsilon_{data} - \epsilon_{sim} = -0.03 \pm 0.04$$

The result is consistent with zero so the uncertainty was used to give a systematic difference between data and simulation of 4 %. The analysis was repeated 100 times on the simulation data where the DsECal component of random TPC3-DsECal tracks were ignored 4 % of the time. The result of fitting the data with the samples is shown in Figure 4.20. The effect of the systematic was found to be small and produced an uncertainty of:

$$\delta N(\nu_e) = \pm 0.04$$

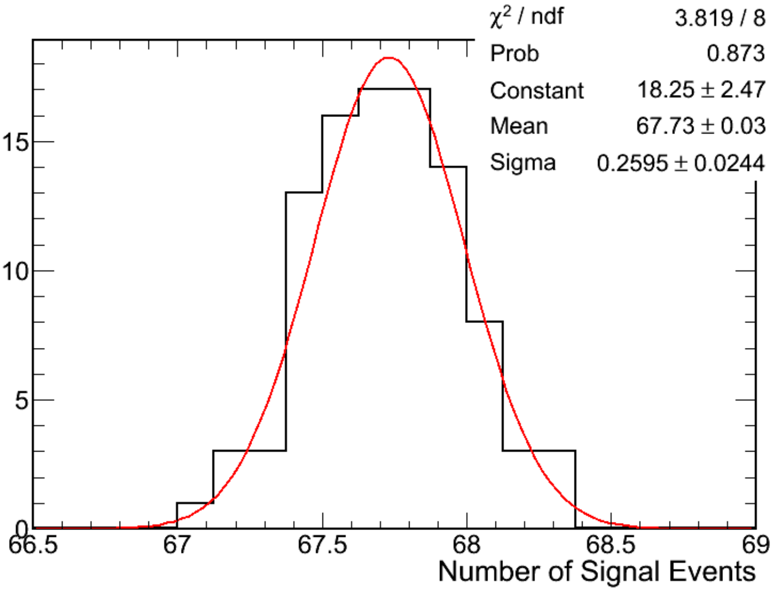

Figure 4.20: The number of extracted signal events from 100 simulation data sets where the TPC-ECal matching efficiency was reduced by 4 %

### TPC PID

The TPC PID systematic uncertainty is dominated by the differences between data and simulation in the electron pull distribution, $P_e$. Figure 4.21 shows the electron pull for data (left) and simulation (right). The samples shown have had the analysis pre-selection cuts up to the PID applied and then the cuts on the muon and pion pulls. The two distributions were fitted with Gaussian distributions and the difference between the fit parameters for data and simulation were used to calculate the systematic uncertainties on the difference in mean and width:

- Difference in mean: shift $P_e$ in the simulation by $0.13 \pm 0.09$.
- Difference in width: smear $P_e$ in the simulation by a factor $1.20 \pm 0.06$.

The two differences between data and simulation defined above were implemented in the analysis and 100 simulation data samples were created by applying the correction within the uncertainty given and then using the samples to fit the data. The systematic uncertainties from the two corrections were measured as

$$\delta N(\nu_e)_{P_e\,shift} = \pm 0.15 \quad \text{and} \quad \delta(N\nu_e)_{P_e\,smear} = \pm 0.23$$

The effect of data and simulation differences in the muon pull $P_\mu$ were studied in a similar way but applying the inverse of the pion and electron selection criteria.

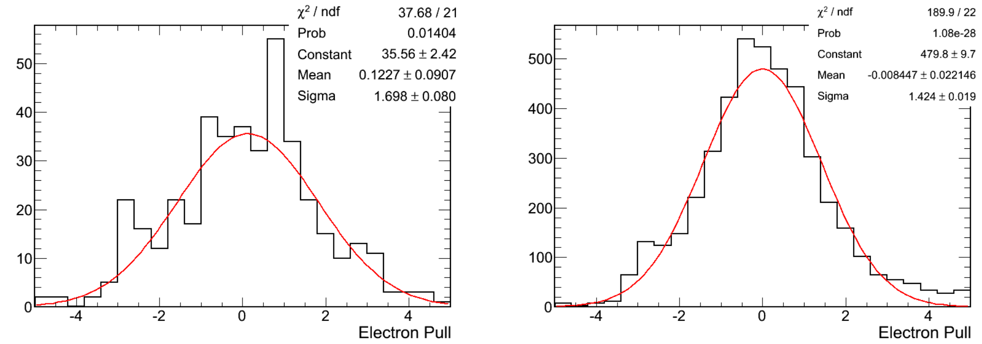

Figure 4.21: The electron pull in data (left) and simulation (right) for all events passing the analysis cuts up to the PID, and also passing the TPC muon and pion rejection cuts.

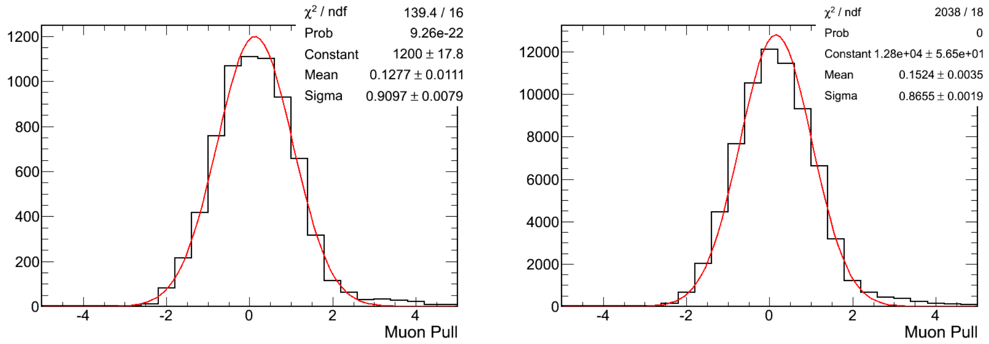

Figure 4.22: The muon pull in data (left) and simulation (right) for all events passing the analysis cuts up to the PID, and also passing the inverted electron selection and pion rejection cuts.

The muon pull distribution is shown in Figure 4.22 for data (left) and simulation (right), showing very small differences compared to the $P_e$ distributions. However, the number of muons is very large so even a small difference could have a significant effect on the analysis. The systematic uncertainty was calculated for both the shifting and smearing of the muon pull:

$$\delta N(\nu_e)_{P_\mu \, shift} = \pm 0.18 \quad \text{and} \quad \delta(N\nu_e)_{P_\mu \, smear} = \pm 0.07$$

and hence, the total systematic uncertainty from the TPC PID was measured to be:

$$\delta N(\nu_e) = \pm 0.34$$

### ECal Electron Selection Efficiency

The electron selection systematic uncertainty from the DsECal was calculated using data from the CERN testbeam run, described in Appendix A. The testbeam data was used as it provided an independent data sample to the neutrino beam data. A high purity sample of electrons was obtained using particle identification information from two Čerenkov detectors and a time of flight counter. Data were collected over a momentum range of 300 MeV/c to 4.0 GeV/c and at three different angles of incidence: 0°, 30° and 60°.

For each data run a bespoke simulation run was produced such that the electron selection efficiency could be compared between data and simulation. The electron selection criterion for the DsECal in the $\nu_e$ analysis is that the reconstructed object should have a track-shower discriminator value of less than 0.2. This selection criterion was applied to all of the data and simulation runs and the selection efficiency $\epsilon$ was calculated in the following way:

$$\epsilon = \frac{N_p}{N_t} \tag{4.7}$$

where $N_p$ is the number of events passing the selection criterion and $N_t$ is the true number of electrons. $N_t$ was obtained from truth information for the simulated data, and for data was based on the assumption of a 100 % pure sample. In the case that multiple runs were taken at the same momentum and angle then the efficiencies were combined using a weighted average.

The assumption of a 100 % pure sample is good for the low momentum data, but becomes less accurate at higher momentum. The number of electrons in the testbeam with respect to the number of pions decreases at high momentum, meaning that any contamination is likely to be larger at high momentum. This would have the effect of generating an efficiency that was lower in data that it should be, since the denominator in the efficiency calculation is artificially high. Events that were clearly track-like were removed from the data samples for momentum points above 1 GeV, as it was clear that these events were pions.

Figure 4.23 shows the selection efficiency as a function of momentum for data and simulation at 0° angle of incidence. The selection efficiency is systematically lower in data than in the simulation, hence the difference can be used to provide a systematic uncertainty.

The efficiencies shown in Figure 4.23 were averaged using the weighted average shown in Equation 4.8 over the momentum range for both data and simulation. The same procedure was applied to the efficiencies for the other angles of incidence

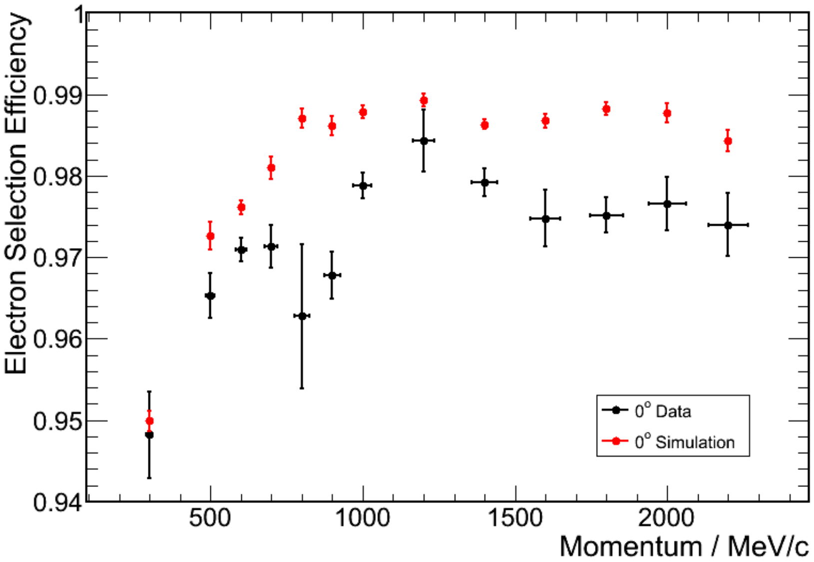

Figure 4.23: Electron selection efficiency in the DsECal for testbeam data and simulation at 0° angle of incidence plotted as a function of particle momentum. The efficiency axis has been zoomed in to the range 0.94 to 1.00.

such that a single efficiency was calculated for each angle of incidence.

$$\bar{\epsilon} = \frac{\sum_{i=1}^{n} \frac{\epsilon_i}{\sigma_i^2}}{\sum_{i=1}^{n} \frac{1}{\sigma_i^2}} \quad \text{with uncertainty} \quad \sigma_\epsilon = \sqrt{\frac{1}{\sum_{i=1}^{n} \frac{1}{\sigma_i^2}}} \tag{4.8}$$

The efficiencies are shown in Table 4.9 where the 'Total' entry gives the efficiency averaged over the angles using a weighted average. Few particles in the T2K neutrino beam data or simulation enter the DsECal at 60° due to the geometry of the ND280 so this average provides a conservative estimate of the systematic uncertainty. The difference in the selection efficiency for data and simulation is taken to be the systematic uncertainty for the DsECal electron selection of 1.6 %.

The effect of the 1.6 % difference in selection efficiency in data and simulation was studied by randomly setting the ECal PID decision as failed for 1.6 % of events in the simulation. This process was repeated to produce 100 sets of reweighted simulation which were used to fit the data. Figure 4.24 shows the number of extracted signal events, $N(\nu_e)$, for the 100 fits to the data fitted with a Gaussian distribution. The difference between the mean of the Gaussian and the nominal

| Sample | Electron Selection Efficiency (%) | | |
|---|---|---|---|
| | Data | Simulation | Difference |
| 0° | $97.42 \pm 0.07$ | $98.42 \pm 0.03$ | $1.00 \pm 0.08$ |
| 30° | $96.87 \pm 0.07$ | $97.73 \pm 0.03$ | $0.86 \pm 0.08$ |
| 60° | $92.45 \pm 0.09$ | $95.96 \pm 0.04$ | $3.51 \pm 0.10$ |
| Total | $96.05 \pm 0.04$ | $97.61 \pm 0.02$ | $1.56 \pm 0.04$ |

Table 4.9: The DsECal electron selection efficiency for testbeam data and simulation. The total entry was calculated using an uncertainty weighted average of the three angle entries.

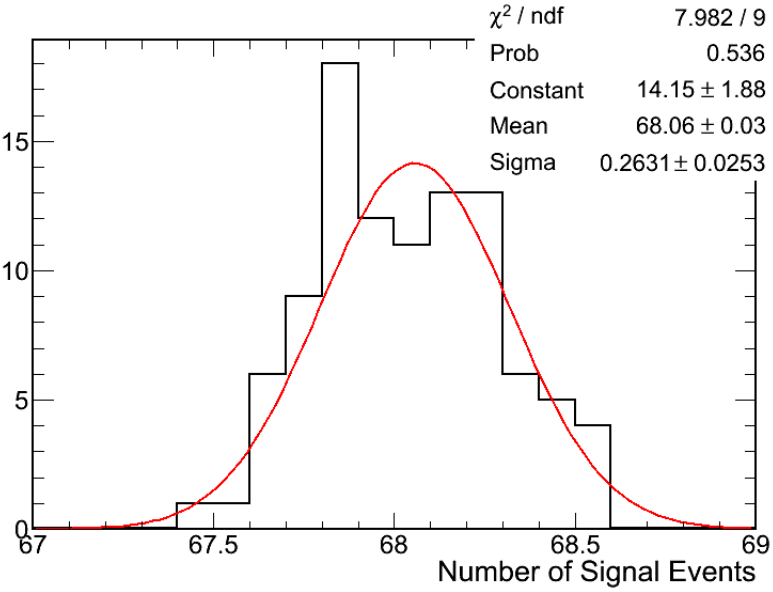

Figure 4.24: The number of extracted signal events for 100 sets of simulation data where a random 1.6 % of events had the ECal PID decision set to false.

number of extracted signal events provides the systematic uncertainty:

$$\delta N(\nu_e) = \pm 0.37$$

### Invariant Mass

The invariant mass calculation is affected by some of the processes accounted for in other detector systematic uncertainties. However, it was decided to vary the position of the cut on the invariant mass distribution from the nominal 250 MeV/$c^2$ to 200 MeV/$c^2$ and 300 MeV/$c^2$. The data were fitted using the two samples with different invariant mass cuts and the fit that produced the largest variation in the number of signal events was used as the systematic uncertainty:

$$\delta N(\nu_e) = \pm 0.43$$

### Detector Vetoes

The statistics available in the CC $\nu_e$ analysis were not high enough to investigate any difference in efficiency between the data and simulation for the detector vetoes for electrons. However, a study was performed using muons from the beam data and simulation, based on a simple CC $\nu_\mu$ selection that was designed to be similar to the CC $\nu_e$ selection. The negative track with the highest momentum was selected and subjected to the following selection criteria:

i Cuts i to iv from the CC $\nu_e$ analysis, listed in Section 4.4.6.

ii Require a muon-like PID ($-2.5 < P_\mu < 2.5$) in the TPC downstream of the FGD where the interaction occurred.

iii P0D Veto.

iv TPC1 Veto.

v FGD1+TPC2 Veto for interactions in FGD2.

The numbers of tracks rejected by each of the three vetoes was counted and calculated as a percentage of all of the tracks passing the muon-like PID selection criterion and are shown in Table 4.10. Some difference between data and simulation for the P0D veto is expected due to the simulation not including interactions in the sand upstream of the ND280. The table shows that the numbers of events rejected by the TPC1 and FGD1+TPC2 vetoes were consistant between data and simulation but that a $4.7 \pm 0.3\,\%$ difference was measured for the P0D veto. An additional 4.7% of events were rejected from the simulation to account for this difference and produced a systematic uncertainty of:

$$\delta N(\nu_e) = \pm 0.25$$

### Charge Confusion

The probability of incorrectly reconstructing the track charge was studied in [83] and showed that for tracks with a momentum in the range 0 GeV/c to 4 GeV/c the number of misidentified tracks was larger in simulation than data by approximately 0.6 %. The reconstructed charges of a random 0.6 % of tracks in the simulation

| Veto | Tracks Rejected (%) | | |
|---|---|---|---|
| | Data | Simulation | Difference |
| P0D | $8.4 \pm 0.3$ | $3.7 \pm 0.1$ | $4.7 \pm 0.3$ |
| TPC1 | $2.0 \pm 0.2$ | $2.2 \pm 0.1$ | $0.2 \pm 0.2$ |
| FGD1+TPC2 | $2.5 \pm 0.2$ | $2.6 \pm 0.1$ | $0.1 \pm 0.2$ |

Table 4.10: The percentage of tracks rejected due to the detector vetoes from the simple CC $\nu_\mu$ selection for data and simulation.

were switched to the opposite polarity to produce 100 simulation data sets. The systematic uncertainty extracted from fitting the number of extracted signal events with a Gaussian was:

$$\delta N(\nu_e) = \pm 0.49$$

### Magnetic Field

The nominal simulation of the magnetic field assumes a uniform field inside the magnet. A study was performed to investigate the systematic uncertainty induced by this simplification and is presented in [84]. The bias in the momentum was found to vary linearly with momentum allowing for a correction to the TPC momentum to be applied:

$$p_c = p(1 + bp) \tag{4.9}$$

where $p_c$ is the corrected TPC momentum, $p$ is the reconstructed TPC momentum and $b$ is the gradient of the bias with respect to momentum. The value of $b$ is considerably larger in TPC3 than in TPC2 due to the end effects of the magnetic field and was measured by fitting the data presented in [84], yielding values of $b = (8.53 \pm 1.10) \times 10^{-6}$ for TPC2 and $b = (2.12 \pm 0.12) \times 10^{-5}$ for TPC3.

The correction was applied to the simulated data within the given uncertainties to produce 100 simulation samples and the data were then refitted, measuring the systematic uncertainty from the magnetic field simulation to be:

$$\delta N(\nu_e) = \pm 0.57$$

| Source of Uncertainty | $\delta N(\nu_e)$ |
|---|---|
| Track Quality Cuts | 0.32 |
| TPC Efficiency | 0.14 |
| TPC-FGD Association | 0.13 |
| TPC-ECal Association | 0.04 |
| TPC PID | 0.34 |
| ECal PID | 0.37 |
| Invariant Mass | 0.43 |
| P0D Veto | 0.25 |
| Charge Confusion | 0.49 |
| Magnetic Field | 0.57 |
| Total | 1.10 |

Table 4.11: A summary of the systematic uncertainties coming from the detector.

### Summary

Various sources of systematic uncertainty resultant from the detector and the way in which different detectors were used in the analysis were studied and the contributions of each source is summarised in Table 4.11. The total systematic uncertainty resultant from detector systematics was calculated by summing the individual systematic uncertainties in quadrature:

$$\delta N(\nu_e)_{detector} = \pm 1.10$$

## 4.7.2 Simulation Statistics

The statistics of the simulation can cause systematic uncertainties in the analysis in two ways and are discussed below:

i Statistical uncertainty from bin variations.

ii Overall normalisation for fixed components.

Systematic uncertainties in the neutrino flux and interaction cross-sections can change the shape of the simulation distributions and these uncertainties are discussed in Sections 4.7.3 and 4.7.4.

### Statistical Fluctuations

The number of events in each bin for each of the template histrograms was varied according to the Poisson distribution. The nominal number of events in the bin was

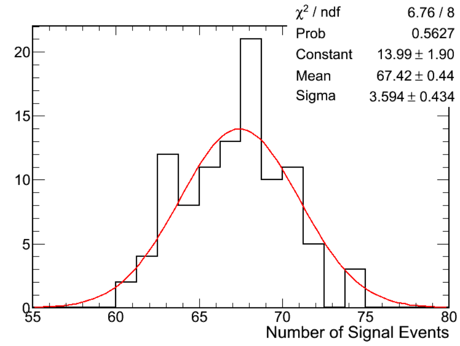

Figure 4.25: The number of signal events extracted for 100 fits varying the simulation PDFs within statistical uncertainty.

used to generate a Poisson distribution and then a random value was taken from the distribution and used as the shifted value for the bin. This was repeated for each bin and then the entire process was repeated 100 times and the result of fitting the number of signal events is shown in Figure 4.25. The width of the Gaussian gives the systematic uncertainty to be:

$$\delta N(\nu_e) = \pm 3.59$$

### Normalisation Uncertainty

The normalisation of three components of the fit were kept constant: $\nu_\mu\mu$ and $\nu_\mu$-other from the negative analysis and $\nu_\mu$-other from the positive analysis. The value chosen for the normalisation was the fraction of the given type of event from the simulation and had an associated statistical uncertainty. The normalisation and uncertainty as a percentage of the total number of events are listed below for the three components:

- $\nu_\mu\mu$ from the negative analysis: $3.72 \pm 0.33\,\%$.
- $\nu_\mu$-other from the negative analysis: $4.14 \pm 0.34\,\%$
- $\nu_\mu$-other from the positive analysis: $13.22 \pm 0.83\,\%$

A random number $n$ was extracted from a Normal distribution and the normalisation of the component was varied by $n\sigma$ where $\sigma$ is the statistical uncertainty of the component. The data were then fitted using the simulation with the different normalisation and the procedure was repeated 100 times. Figure 4.26 shows the

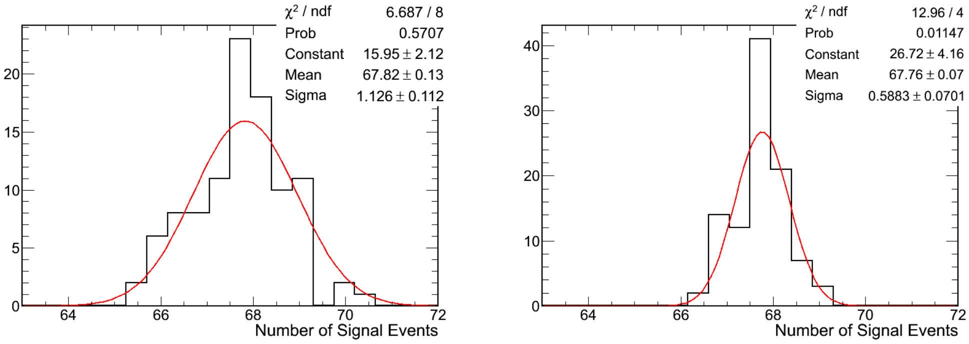

Figure 4.26: The number of extracted signal events after varying the normalisation of the $\nu_\mu\mu$ (left) and $\nu_\mu$ other (right) components in the negative analysis by the statistical uncertainty.

number of extracted signal events after varying the $\nu_\mu\mu$ normalisation (left) and the $\nu_\mu$-other normalisation (right) for the negative analysis. The effect of varying $\nu_\mu$-other from the positive analysis was negligible and hence no systematic uncertainty was measured. The total systematic uncertainty from the normalisation of these components is given by the quadrature sum of the widths of the Gaussians:

$$\delta N(\nu_e) = \pm 1.27$$

Combining the uncertainty from the statistical fluctuations within bins and the normalisation of the fixed components gives the total systematic uncertainty due to the simulation statistics as:

$$\delta N(\nu_e)_{MCstat} = \pm 3.81$$

### 4.7.3 Flux Systematics

The flux systematic uncertainty was calculated using the T2K simulation re-weighting tool [85]. The flux is re-weighted by varying the 22 different flux bin weights, listed in terms of the bin boundaries in GeV/c below:

- $\nu_\mu$: 0.0, 0.4, 0.5, 0.6, 0.7, 1.0, 1.5, 2.5, 3.5, 5.0, 7.0 and 30.0.
- $\nu_e$: 0.0, 0.5, 0.7, 0.8, 1.5, 2.5, 4.0 and 30.0.
- $\bar{\nu}_\mu$: 0.0, 1.5 and 30.0.
- $\bar{\nu}_e$: 0.0, 2.5 and 30.0.

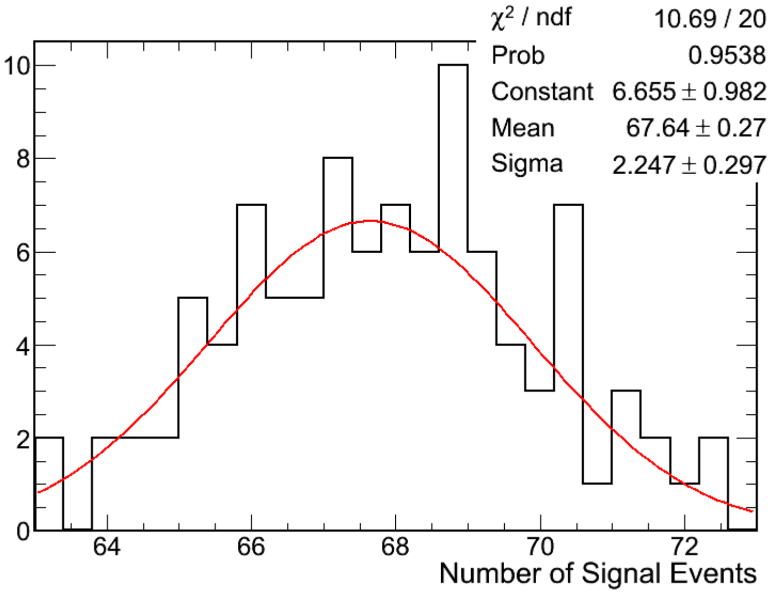

Figure 4.27: The number of extracted signal events for 100 sets of simulation data where the neutrino flux was varied within uncertainty according to the flux covariance matrix.

The flux bin weights are not independent variables and their correlations are described by the flux covariance matrix. The standard matrix produced by the beam group was reduced in binning to match the binning provided by the re-weighting package. A twenty two dimensional Gaussian function was constructed with a mean of zero in each dimension using the RooFit package in ROOT. The correlations of the 22 dimensions were provided by the flux covariance matrix. One hundred random points in the 22 dimensional space were generated to provide the weight to vary the flux bins. The hundred points were used to produce 100 samples of independent re-weighted simulation samples that were then fitted to the data in the likelihood fit. Figure 4.27 shows the number of signal $\nu_e$ events extracted from the data sample for the 100 re-weighted simulation samples. The mean of the distribution is consistent with the nominal number of $\nu_e$ events extracted, as expected, and the width of the distribution provides the systematic uncertainty associated with the beam flux uncertainties:

$$\delta N(\nu_e)_{\text{flux}} = \pm 2.25$$

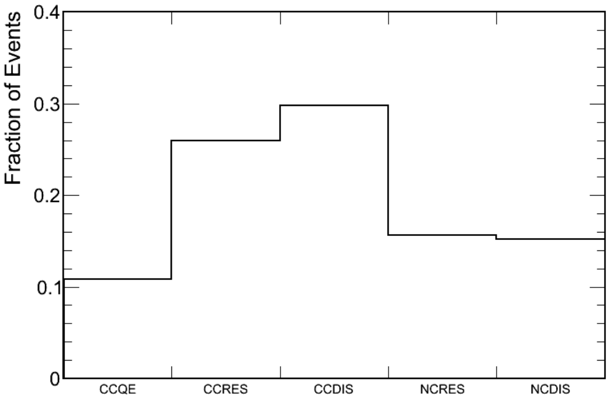

Figure 4.28: The fractional number of events in the analysis arising from the five cross-section categories.

### 4.7.4 Cross-section Systematics

The breakdown of the simulation sample into the different interaction processes is shown in Figure 4.28. It shows that the sample is made up of about 70 % of events from CC processes and 30 % from NC processes, where events have been categorised according to the GENIE generator. All five of the categories have significant contributions to the analysis and so the uncertainties on the cross-sections for the different processes need to be accounted for. The procedure for calculating the individual systematics for each process is given below:

i Throw a random number $n$ from a Normal distribution.

ii Vary the cross section parameter $x$ by $n\sigma_x$ where $\sigma_x$ is the fractional uncertainty on parameter $x$.

iii Re-weight the simulation according to the parameter variation using the T2K-ReWeight package [85].

The procedure was repeated 100 times to produce 100 re-weighted simulation samples that were used to fit the data sample. The width of the extracted number of signal events $N(\nu_e)$ provides the systematic uncertainty associated with the varied cross-section parameter. Table 4.12 shows the measured systematic uncertainty for each of the cross-section parameters considered.

| Process | Parameter | Uncertainty (%) | $\delta N(\nu_e)$ |
|---|---|---|---|
| CCQE | CCQE axial mass $M_A$ | 20 | 0.08 |
|  | Pauli suppression | 30 | 0.13 |
| CCRES | CC Resonance axial mass $M_A$ | 20 | 0.03 |
|  | CC Resonance vector mass $M_V$ | 10 | 0.03 |
| NCRES | NC Resonance axial mass $M_A$ | 20 | 0.16 |
|  | NC Resonance axial mass $M_V$ | 10 | 0.01 |
| COH $\pi$ | Coherent pion production axial mass $M_A$ | 40 | 0.06 |
| Soft DIS | Rate CC $\nu n \to 1\pi$ | 50 | 0.07 |
|  | Rate CC $\nu n \to 2\pi$ | 50 | 0.06 |
|  | Rate CC $\nu p \to 1\pi$ | 50 | 0.12 |
|  | Rate CC $\nu p \to 2\pi$ | 50 | 0.29 |
|  | Rate NC $\nu n \to 1\pi$ | 50 | 0.06 |
|  | Rate NC $\nu n \to 2\pi$ | 50 | 0.00 |
|  | Rate NC $\nu p \to 1\pi$ | 50 | 0.01 |
|  | Rate NC $\nu p \to 2\pi$ | 50 | 0.12 |
| DIS | Parameter A from Bodek-Yang | 25 | 0.18 |
|  | Parameter B from Bodek-Yang | 25 | 0.18 |
|  | Parameter CV1u from Bodek-Yang | 30 | 0.17 |
|  | Parameter CV2u from Bodek-Yang | 40 | 0.18 |
|  | Total | - | 0.56 |

Table 4.12: The measured systematic uncertainty for each of the cross-section parameters. The uncertainty on the cross-section parameters are those from GENIE[77]. The Bodek-Yang parameters are described in [23]. Soft DIS events are defined as DIS interactions with an invariant hadronic mass less than $2\,\mathrm{GeV/c^2}$.

### Final State Interactions

Final state interactions (FSI) describe the interaction of particles within the atomic nucleus. The probability that a nucleon or pion can escape the nucleus is dependent on the mean free path of the particle inside the nucleus. GENIE provides two sets of parameters to investigate the systematic uncertainty as a result of FSI, the mean free path and the fate parameters. The mean free path describes how likely the particle is to interact in the nucleus and the fate parameters give the relative probability of five different interaction processes, given that the nucleon or pion has interacted in the nucleus and are listed below:

- Inelastic
- Elastic
- Charge exchange
- Absorption
- Pion production

The parameters are described separately for nucleons and pions and since the mean free path and fate parameters are independent they were treated as individual sources of uncertainty. The five fate parameters are clearly correlated with each other because they must sum to one. The mean free paths for nucleons and pions were varied separately using the method described for the other cross section parameters. The fate parameters were all varied concurrently, with all the parameters varied within their uncertainties apart from the parameter controlling the elastic probability. The elastic probability was not varied explicitly, but was varied by the re-weighting package to keep the total interaction probability equal to one. The systematic uncertainty for FSI of pions and nucleons was measured to be:

$$\delta N(\nu_e)_{FSI,\pi} = \pm 2.38 \quad \text{and} \quad \delta N(\nu_e)_{FSI,N} = \pm 0.82$$

### Summary of Cross-Section Systematics

The cross-section systematic uncertainties were measured using a simulation reweighting technique to give a total cross-section systematic uncertainty of:

$$\delta N(\nu_e)_{xsec} = \pm 2.58$$

| Source of Uncertainty | $\delta N(\nu_e)$ |
|---|---|
| Detector | 1.10 |
| Simulation Statistics | 3.81 |
| Flux | 2.25 |
| Cross-Section | 2.58 |
| Total | 5.24 |

Table 4.13: A summary of the systematic uncertainties coming from the detector, simulation statistics, flux and cross-sections.

### 4.7.5 Summary of Systematics

A summary of the systematic uncertainties coming from the detector, simulation statistics, flux and cross-sections is given in Table 4.13. The total systematic uncertainty on the number of CC $\nu_e$ events was measured to be ±5.24, compared to the statistical uncertainty of ±12.9 events. The dominant systematic effect is from the simulation statistics so in future it will be necessary to have larger Monte Carlo simulation productions to reduce the systematic uncertainty.

## 4.8 Conclusions

A measurement of the $\nu_e$ component of the T2K beam was made using the ND280. The number of CC $\nu_e$ events measured using the Run 1 and Run 2 data was

$$N(\nu_e) = 67.7 \pm 12.9(stat) \pm 5.2(syst)$$

and with a corresponding ratio between data and simulation equal to

$$\frac{N(\nu_e)_{Data}}{N(\nu_e)_{Sim}} = 0.983 \pm 0.191(stat) \pm 0.076(syst)$$

Agreement is seen between the data and simulation, providing evidence that the $\nu_e$ flux is correctly modelled within the uncertainties. This provides good evidence that the background from intrinsic beam $\nu_e$ in the $\nu_\mu \rightarrow \nu_e$ oscillation analysis was correctly estimated and did not underestimate the true size of the intrinsic $\nu_e$ component of the beam. It is clear that at this stage the uncertainty on the measurement is dominated by statistical uncertainty so further data are required to provide a more precise measurement. A study of how the measurement of the $\nu_e$ component of the beam can be used to constrain the neutrino flux uncertainties is presented in Chapter 5.

Future analyses will go beyond the method of simply comparing the number of events measured in data and simulation. This analysis measured the electron momentum distribution but ideally it is the $\nu_e$ energy distribution that requires measurement. With a greater number of data the possibility of performing an exclusive CCQE measurement arises. This is a particularly interesting measurement because the simple kinematics of the CCQE process means that the neutrino energy can be easily reconstructed from the electron momentum, and hence provide a direct measurement of the $\nu_e$ energy spectrum. Improvements will also be made in the analysis, with the addition of the Barrel ECal modules to aid the detection of electrons and updated timing measurements between the subdetectors to reduce the size of the Non-FGD background component.

# Chapter 5

# Neutrino Flux Systematic Uncertainty Minimisation

## 5.1 Introduction

The first oscillation analyses used the ND280 $\nu_\mu$ analysis as a measure of the data to simulation ratio. It is clear that the ND280 can be used to provide much more information to the oscillation analyses. A study [86] was performed to investigate how well the ND280 $\nu_\mu$ analysis could constrain the neutrino flux uncertainties and cross-section parameters. The goal of the study described in this chapter was to investigate how the ND280 CC $\nu_e$ analysis described in Chapter 4 can be used in addition to the ND280 $\nu_\mu$ analysis to constrain the neutrino flux parameters. At the time of the study the detector and cross-section effects were not sufficiently studied for inclusion, hence it is an idealised study where only the systematic uncertainties from the neutrino flux and the statistical uncertainty on the simulation samples are considered.

### 5.1.1 Overview of the Study

The analyses in the ND280 measure the lepton momentum but the flux is described by neutrino energy, hence a method to convert between lepton momentum and neutrino energy was developed. The simulated lepton momentum distribution from each ND280 analysis was divided into components, called templates, where all events in the same template were initiated by neutrinos from the same neutrino energy bin. The templates allow the relative number of events from a given flux bin to be varied independently.

This method allows a lepton momentum distribution $d_i$ to be constructed from $i$ templates $t_i$ with a weight $w_i$ applied to each of the templates in the following way

$$d_i = \sum_i w_i t_i \tag{5.1}$$

where $i$ is the number of neutrino energy bins.

Equation 5.1 provides the key to the analysis because it can be used to both generate toy data samples with varying weights and fit an unknown sample to measure the weights. This is a generic equation for any given distribution and the following sections provide the details on the data samples, weights and templates used in this analysis.

## 5.2 Flux Parameters

The neutrino flux, both $\nu_\mu$ and $\nu_e$, was binned in neutrino energy and used the same bins as described in [86] where the binning was optimised according to the following criteria:

- Fine binning around the oscillation maximum.
- Fine binning for regions with high contributions in the data samples.
- Uniform flux uncertainty within a given bin, stable within about 2 %.
- Highly correlated bins should be combined.

The result of the optimisation was that 11 energy bins were used for $\nu_\mu$ flux components and 7 energy bins for $\nu_e$ components. Two bins were defined for the corresponding anti-neutrino fluxes but these components are not considered here. The flux binning used was the same for the ND280 and Super-K fluxes and the bin edges are given below in GeV.

$\nu_\mu$: 0.0, 0.4, 0.5, 0.6, 0.7, 1.0, 1.5, 2.5, 3.5, 5.0, 7.0 and 30.0

$\nu_e$: 0.0, 0.5, 0.7, 0.8, 1.5, 2.5, 4.0 and 30.0

Each flux bin has an associated weight parameter that can be varied to change the weight in a particular flux bin. The flux bin parameters are not independent and the correlations between them are parameterised by the flux covariance matrix. Figure 5.1 shows a graphical representation of the flux covariance matrix where the flux bin numbers correspond to the flux components in the following order: 11 ND280 $\nu_\mu$, 7 ND280 $\nu_e$, 11 Super-K $\nu_\mu$ and 7 Super-K $\nu_e$. The bins are ordered from lowest energy to highest energy within each component.

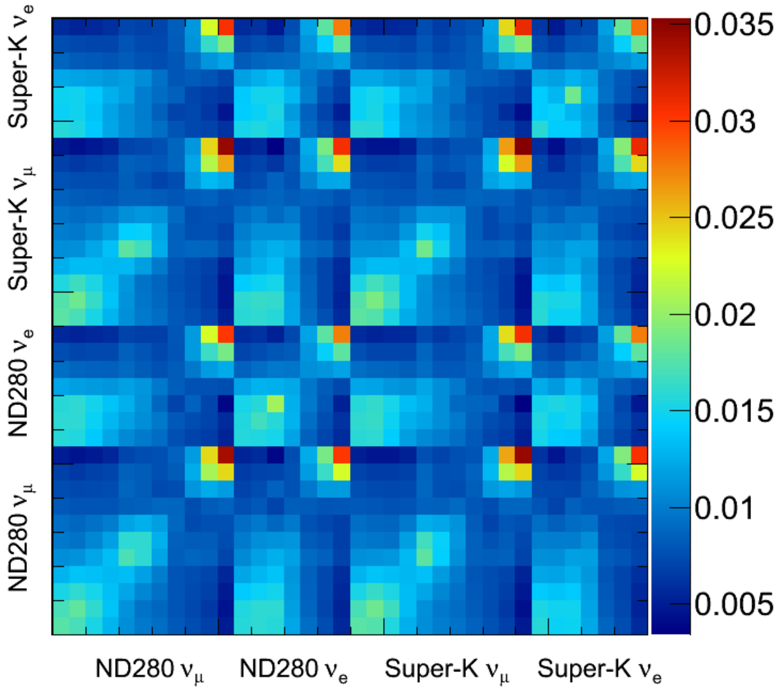

Figure 5.1: A graphical representation of the fractional covariance matrix between the four sets of flux parameters using the flux energy binning given in Section 5.2.

## 5.3 Fit Samples

The study used the results from the simulation of two main analyses from the ND280: the ND280 CC $\nu_\mu$ analysis and the ND280 CC $\nu_e$ analysis.

### 5.3.1 ND280 $\nu_\mu$ Samples

The ND280 $\nu_\mu$ analysis [78] provides two independent samples for the study. The first sample is the $\nu_\mu$ CCQE enhanced sample that contains all events selected by the ND280 $\nu_\mu$ analysis that have a single track in TPC2. The second sample contains all the other selected $\nu_\mu$ CC-non-QE events and is called the $\nu_\mu$ CCnQE sample. The two samples each consist of 20 $(p, \cos\theta)$ bins, where $p$ is the muon momentum and $\theta$ is the angle of the muon with respect to the neutrino direction, where the neutrino direction is assumed to be along the $Z$ axis of the ND280. The bins are defined in the following way:

- Momentum bin edges (GeV/c): 0.0, 0.4, 0.5, 0.7, 0.9 and 5.0
- $\cos\theta$ bin edges: 0.0, 0.84, 0.90, 0.94 and 1.0

The samples are considered to depend only on the ND280 $\nu_\mu$ flux because the CCQE and CCnQE samples are over 99 % and 97 % pure with respect to $\nu_\mu$ interactions.

### 5.3.2 ND280 $\nu_e$ Samples

The ND280 $\nu_e$ analysis, described in Chapter 4, adds two further samples to the study. The first of the samples is the CC $\nu_e$ selection and the second sample is the positive analysis selection. The positive analysis sample consists of a single bin in $(p, \cos\theta)$ space where only the momentum range from 0 GeV/c to 0.6 GeV/c was considered.

Different binning schemes for the $\nu_e$ sample were considered, both consisting of a single $\cos\theta$ bin and either 1 or 2 momentum bins:

- Single momentum bin with edges (GeV/c): 0.0 and 10.0
- Two momentum bins with edges (GeV/c): 0.0, 0.6 and 10.0

The bins for the two momentum bin case were chosen so that the low momentum bin matched the width of the positive analysis bin. The total number of bins is considerably lower than for the $\nu_\mu$ samples because the $\nu_e$ samples contain far fewer events.

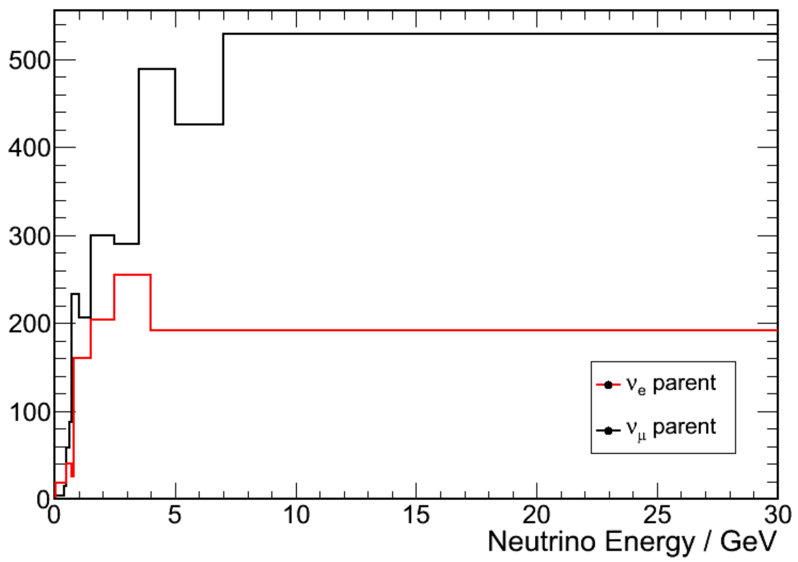

Figure 5.2: The selected simulated events from the ND280 $\nu_e$ analysis plotted as a function of true neutrino energy split between interactions from $\nu_\mu$ and $\nu_e$. The binning differs between the two flux components as described in Section 5.2.

Figure 5.2 shows the breakdown of the ND280 CC $\nu_e$ selection by the true parent neutrino type. It shows that the backgrounds to the CC $\nu_e$ signal events are caused by high energy $\nu_\mu$ events. The CC $\nu_\mu$ interactions measured by the ND280 CC $\nu_\mu$ analysis are generally of considerably lower energy meaning that the ND280 CC $\nu_e$ selection should be able to help constrain the high energy $\nu_\mu$ flux parameters in addition to the $\nu_e$ flux parameters. The $\nu_\mu$ and $\nu_e$ flux components are binned differently in the plot such that they match the flux binning defined in Section 5.2.

## 5.4 Simulation Templates

The simulated events from each of the analyses described in Section 5.3 were used to produce a series of simulation templates. A series of simulation templates were produced from each simulation sample where each template contained events from a single true neutrino energy flux bin. The simulation templates used the same $(p, \cos\theta)$ binning as defined for the given sample. A template was created for each flux bin to allow the fraction of events in the sample from each flux bin to be independently controlled by a weight parameter.

The $\nu_\mu$ CCQE, $\nu_\mu$ CCnQE and positive analysis samples were divided into 11 templates, one for each of the ND280 $\nu_\mu$ flux bins. The CC $\nu_e$ analysis was divided into 18 templates, 11 for the ND280 $\nu_\mu$ flux bins and 7 for the ND280 $\nu_e$ bins.

## 5.5 Toy Simulation Samples

A set of 1000 toy simulation datasets were produced for each of the samples given in Section 5.3. These were produced by throwing a set of flux weight parameters according to the flux covariance matrix and then building the sample by adding together contributions from each flux bin $i$ to give the number of events in a $(p, \cos\theta)$ bin, $N_{p,\cos\theta}$:

$$N_{p,\cos\theta} = \sum_i f_i (M_{p,\cos\theta})_i \tag{5.2}$$

where the $f_i$ are the thrown flux weights and the $(M_{p,\cos\theta})_i$ are the corresponding simulation templates. Equation 5.2 describes the ND280 $\nu_\mu$ samples because only a single flux component is considered. The CC $\nu_e$ sample is described by the following equation, considering both the ND280 $\nu_\mu$ and ND280 $\nu_e$ flux components, where the superscript denotes the neutrino flavour:

$$N^e_{p,\cos\theta} = \sum_i f^\mu_i (M^\mu_{p,\cos\theta})_i + f^e_i (M^e_{p,\cos\theta})_i \tag{5.3}$$

Statistical variations are applied to the simulation templates using Poisson statistics to account for the statistical uncertainty of the simulation in each bin. The total number of events in each sample was scaled to match the number of events expected in the data.

## 5.6 Fitting Procedure

A binned $\chi^2$ function was used to fit the simulation templates to the toy simulation samples. The predicted number of events in a given $(p, \cos\theta)$ bin for a given sample was calculated by using the simulation templates to sum the contributions from each flux bin. Equations 5.2 and 5.3 show how the number of predicted events was calculated for the different samples. The number of predicted events in the $(p, \cos\theta)$ bins depended only on the values of the flux parameters $f_i$, meaning that the fitting procedure was used to fit the values of the $f_i$. The exact functional form of the expression minimised by the fit is given below.

### 5.6.1 Functional Form

The function $X$ defined in Equation 5.4 was minimised by the ROOT MINUIT package to fit the values of the ND280 neutrino flux weight parameters $f_i$:

$$X = \sum_i \frac{(n_i - N_i)^2}{\sigma_{n_i}^2 + \sigma_{N_i}^2} + \sum_j \sum_k (1 - f_j)(1 - f_k) F_{jk} \tag{5.4}$$

The term on the left is the standard $\chi^2$ term that measures how well the number of events $n_i$ in a given $(p, \cos\theta)$ bin $i$ is described by the number of predicted events $N_i$ from Equations 5.2 and 5.3. The second term is the flux constraint term that considers the flux parameters as nuisance parameters in the fit, where the $f_i$ are the flux parameters and $F$ is the flux fractional covariance matrix.

## 5.7 Results: ND280 Flux Parameters Only

The first set of fits that were performed only considered the ND280 flux parameters. The ND280 flux parameters are mostly constrained directly by the ND280 samples but the correlations between the flux bins also constrain those flux bins where few data points exist. The results described in this section are from the fitting of 1000 toy simulation datasets. The plots shown in the following sections all show the fractional uncertainty on a given flux bin $\sigma_i$, calculated using the diagonal terms of the fitted covariance matrix $C$

$$\sigma_i = \sqrt{C_{ii}} \tag{5.5}$$

where $C$ describes the covariance of the fitted flux parameters.

### 5.7.1 ND280 $\nu_\mu$ samples only

The ND280 $\nu_\mu$ CCQE and $\nu_\mu$ CCnQE samples were fitted simultaneously to provide the baseline for studying the effect of also fitting the $\nu_e$ samples. Figure 5.3 shows the fractional uncertainty of the ND280 $\nu_\mu$ (left) and $\nu_e$ (right) fluxes. The solid black line shows the flux uncertainties calculated from the flux covariance matrix and represents the flux uncertainty before any fits and the points show the uncertainty after the fitting procedure. The plots show clearly that the ND280 $\nu_\mu$ CCQE and CCnQE samples constrain the flux parameters and reduce the uncertainties of both the $\nu_\mu$ flux and the $\nu_e$ flux. The samples do not directly constrain the $\nu_e$ flux but some constraining power is obtained through the correlation of the flux parameters.

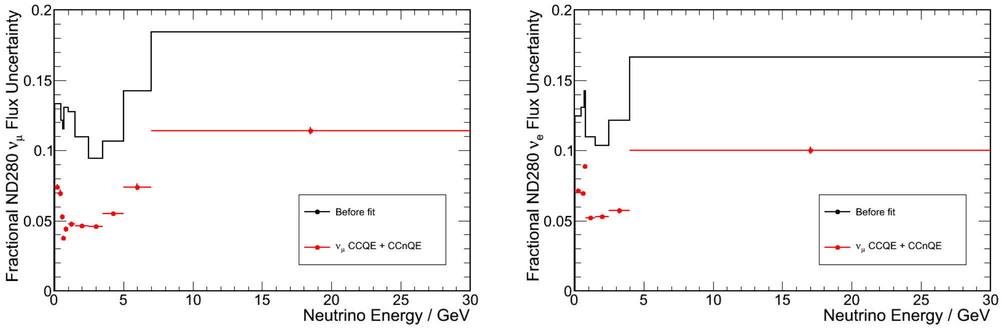

Figure 5.3: The fractional uncertainty of the ND280 $\nu_\mu$ (left) and $\nu_e$ (right) flux. The solid black line shows the uncertainties before the fit and the points represent the uncertainties after the ND280 $\nu_\mu$ CCQE and CCnQE fits.

### 5.7.2 ND280 $\nu_\mu$ and ND280 $\nu_e$

The ND280 $\nu_\mu$ CCQE, $\nu_\mu$ CCnQE and CC $\nu_e$ samples were simultaneously fitted using both 1 bin and 2 bin samples for the $\nu_e$ sample. Figure 5.4 shows the fractional uncertainty of the ND280 $\nu_\mu$ (top) and $\nu_e$ (bottom) flux parameters for the fit with 1 bin (blue) and 2 bin (red) $\nu_e$ samples and the $\nu_\mu$ only fit shown in black as a reference. It is clear from the plots that the addition of the $\nu_e$ sample to the fit reduced the flux uncertainties, with relatively large reductions in the flux uncertainties at high energy for both the ND280 $\nu_e$ and $\nu_\mu$ flux components. The reduction in the uncertainty is seen in the $\nu_e$ flux for neutrino energies over 1.5 GeV and in the $\nu_\mu$ flux from 3.0 GeV. The improvement at high energies was expected from Figure 5.2 because the ND280 CC $\nu_e$ sample contains many high energy neutrino interactions. As expected, a small improvement is seen in considering a 2 bin $\nu_e$ sample over a single bin because it adds an additional data bin to constrain the flux parameters.

#### $\nu_e$ Positive Analysis

The further addition of the $\nu_e$ positive analysis to the fit gives a small reduction in the high energy flux uncertainties. Figure 5.5 shows the difference in the flux uncertainties for the ND280 $\nu_\mu$ (top) and $\nu_e$ (bottom) fluxes, considering the 2 bin $\nu_e$ fit with (red) and without (blue) the positive analysis and the $\nu_\mu$ only fit for reference (black).

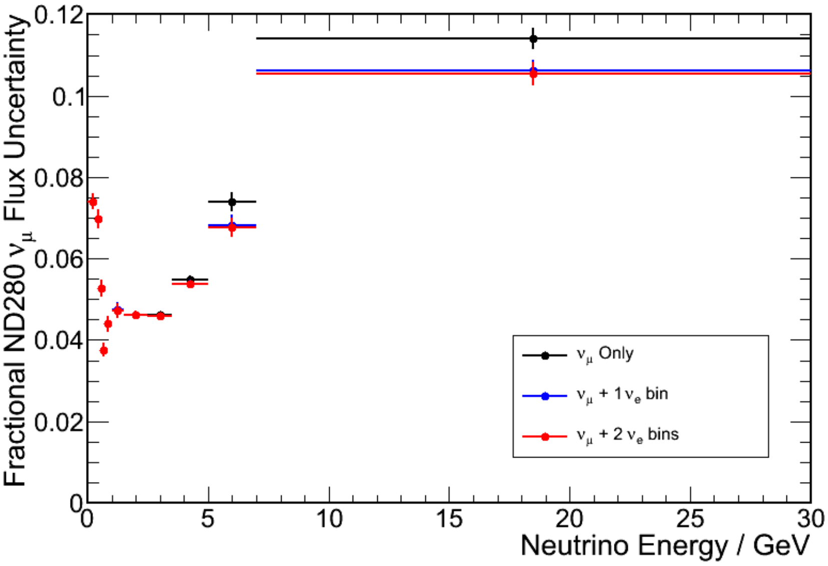

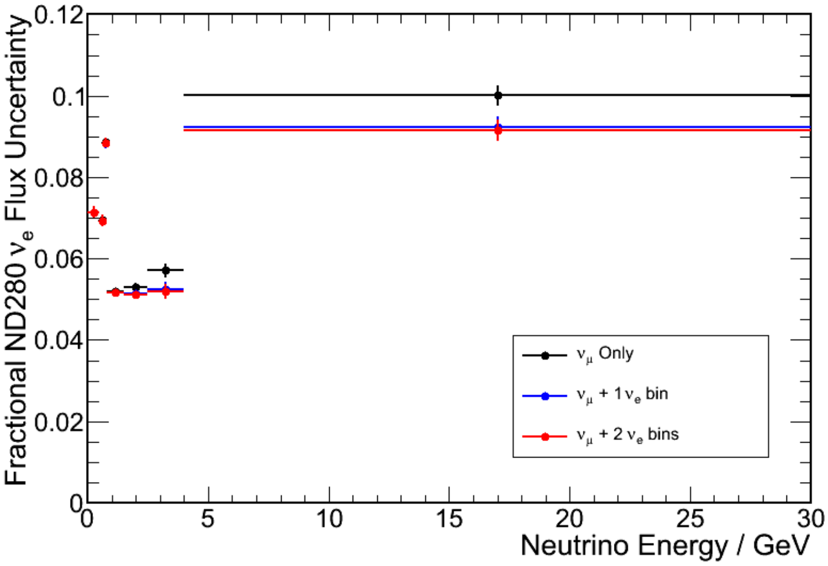

Figure 5.4: The fractional uncertainty of the ND280 $\nu_\mu$ (top) and $\nu_e$ (bottom) flux. The flux uncertainties are shown for the ND280 $\nu_\mu$ CCQE and CCnQE (black) and with the further addition of the 1 bin $\nu_e$ sample (blue) and the 2 bin $\nu_e$ sample (red).

### 5.7.3 Fit Stability

It was decided to use the 2 bin $\nu_e$ sample over the 1 bin sample because of the better performance in terms of reducing the flux uncertainties. The positive analysis was also used as it also made a good contribution to the reduction of the uncertainties. The stability of the fit when fitting all four toy simulation data sets was investigated by studying the pull distributions for each of the parameters in the fit. The pull values of the flux bin weight parameters for 8 different flux bins are shown in Figure 5.6 with Gaussian fits. The pull distributions are expected to follow the Normal distribution and the plots show that the means of the pull distributions are all very close to zero and the widths of the distributions are all close to 1. The plots show that the fitting mechanism behaves as expected and that the fit results are not biased.

### 5.7.4 Increased Statistics

The effect of increased statistics, analogous to increasing the amount of data taken were studied by increasing the size of the samples generated in the toy simulations. Sample sizes were studied in integer multiples of the nominal size ranging from 1 to 5 times the current data sample size for the $\nu_\mu$ CCQE and CCnQE, CC $\nu_e$ and the positive analysis samples. Figure 5.7 shows the effect of increasing the statistics by a factor of 2 and a factor of 5 compared to the nominal size on the flux uncertainties at the ND280 for $\nu_\mu$ flux (left) and the $\nu_e$ flux (right). As expected, increasing the statistics improves the knowledge of the flux parameters but the bottom plot shows that gain from statistical increase gives diminishing returns after about 5 times the current data.

### 5.7.5 Summary

It has been shown that the ND280 CC $\nu_e$ analysis can be used in conjunction with the ND280 $\nu_\mu$ analyses to constrain the uncertainty on the ND280 neutrino flux bins. As expected, the best constraining power came from using the 2 binned $\nu_e$ templates and the positive analysis and the constraints improve with further data taking up to about 5 times the current data. Table 5.1 gives an average uncertainty for the ND280 $\nu_\mu$ and $\nu_e$ fluxes for each of the considered cases, showing that the uncertainty on the flux parameters was reduced by over 50 %. The last row in the table gives the minimum achievable uncertainties of the ND280 $\nu_\mu$ and $\nu_e$ fluxes to be 4.0 % and 5.0 % respectively, using the samples discussed.

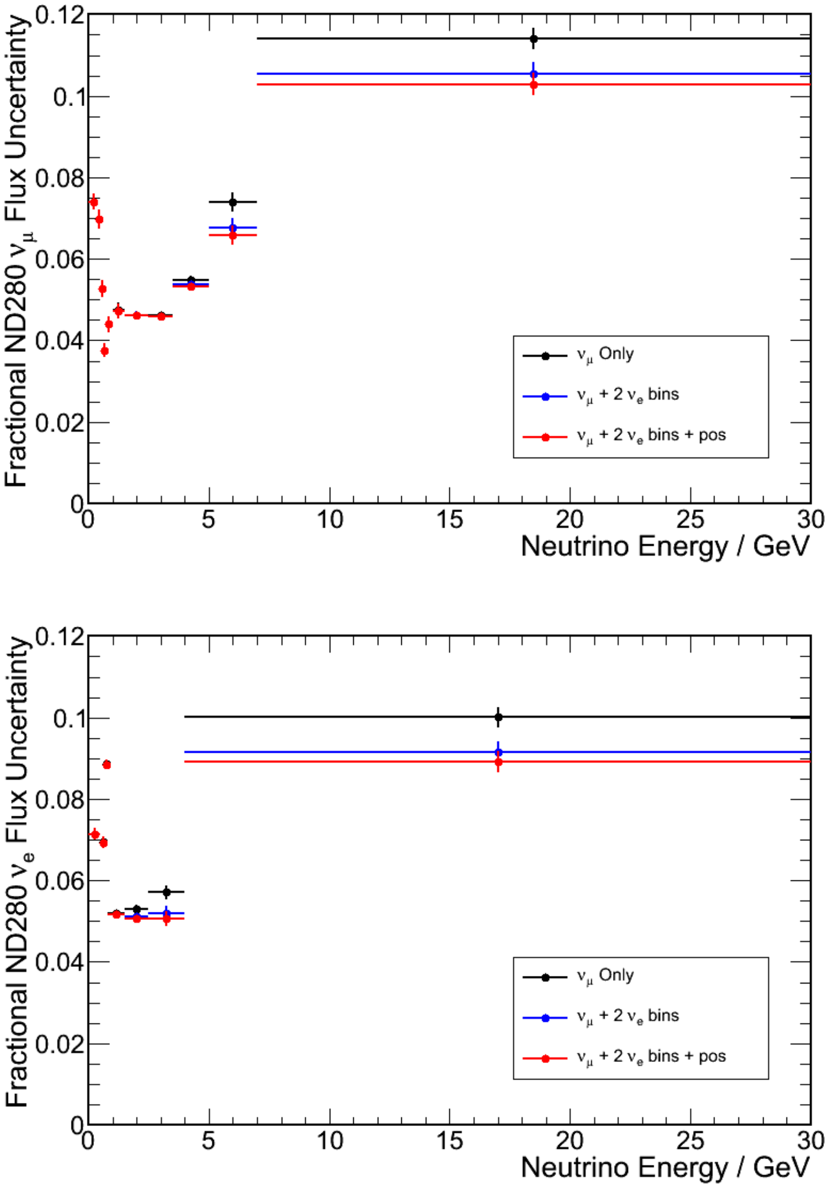

Figure 5.5: The fractional uncertainty of the ND280 $\nu_\mu$ (left) and $\nu_e$ (right) flux. The flux uncertainties are shown for the ND280 $\nu_\mu$ CCQE and CCnQE (black) and with the further addition of the 2 bin $\nu_e$ sample (blue) and finally the addition of the $\nu_e$ positive analysis sample (red).

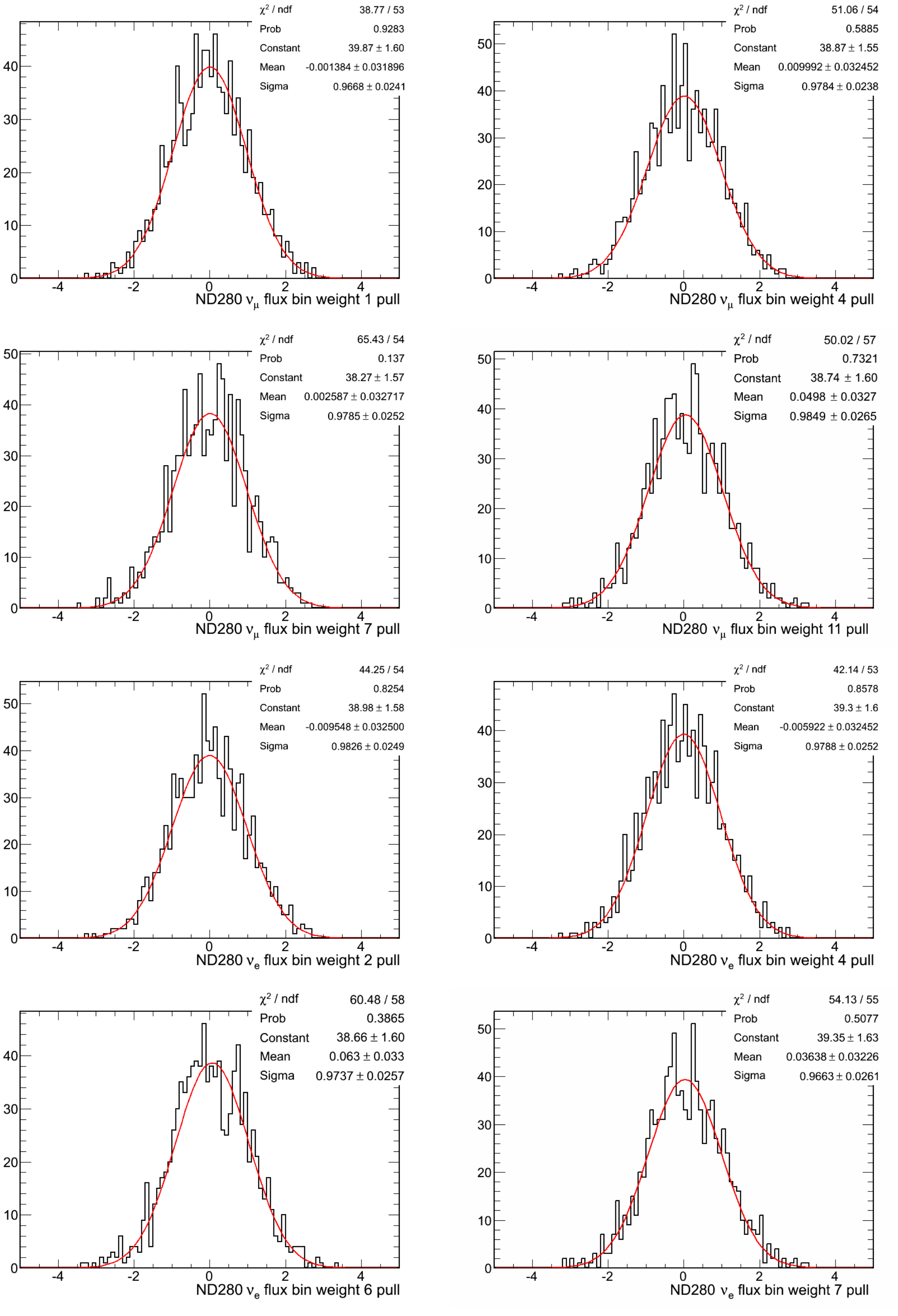

Figure 5.6: Fitted values of flux parameters from the fit to the ND280 $\nu_\mu$ CCQE, $\nu_\mu$ CCnQE, CC $\nu_e$ and positive analyses. The flux parameters shown are the first, fourth, seventh and final flux bins of the ND280 $\nu_\mu$ flux and the first, third, fifth and final flux bins of the ND280 $\nu_e$ flux.

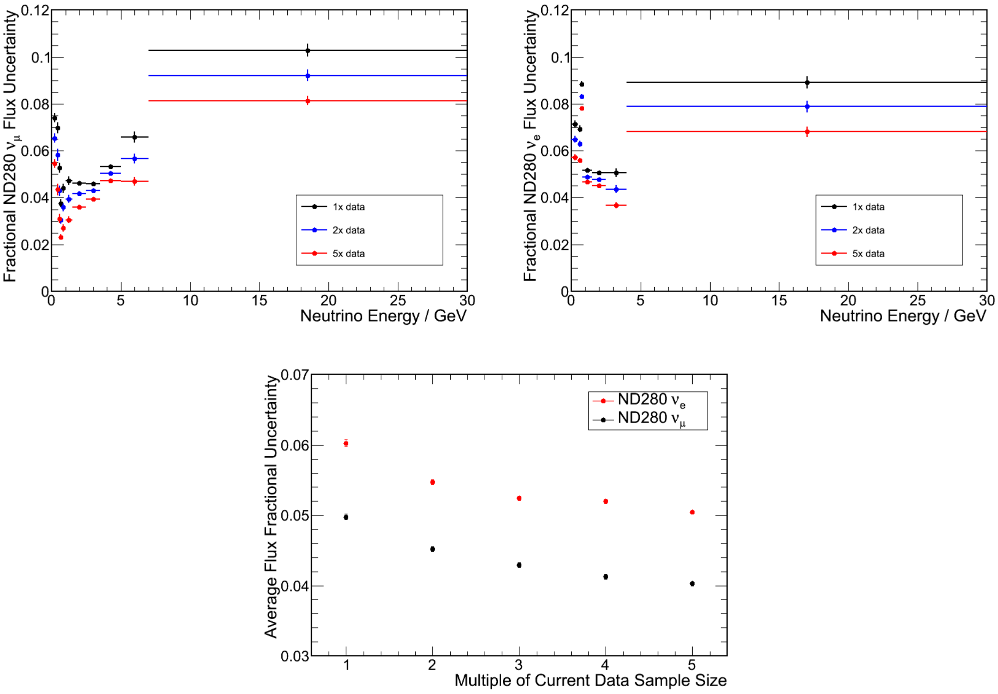

Figure 5.7: The uncertainty on the ND280 $\nu_\mu$ (top left) and $\nu_e$ (top right) fluxes after performing toy simulation fits with 1, 2 and 5 times the current data for all four of the samples. The bottom plot shows the average uncertainty of the ND280 $\nu_\mu$ and $\nu_e$ fluxes as a function of data sample size.

| Sample | Average Flux Uncertainty (%) | |
|---|---|---|
| | ND280 $\nu_\mu$ | ND280 $\nu_e$ |
| Unfitted | 12.72 | 12.84 |
| $\nu_\mu$ | $5.19 \pm 0.04$ | $6.24 \pm 0.04$ |
| $\nu_\mu$ and 2 $\nu_e$ bins | $5.11 \pm 0.04$ | $6.10 \pm 0.04$ |
| $\nu_\mu$, 2 $\nu_e$ bins and positive | $5.08 \pm 0.04$ | $6.03 \pm 0.04$ |
| $\nu_\mu$, 2 $\nu_e$ bins and positive (5× data) | $4.03 \pm 0.03$ | $5.04 \pm 0.03$ |

Table 5.1: Summary of the average flux uncertainties obtained by fitting different combinations of toy simulation samples. The average is taken as the error-weighted average of all the flux bins and is not weighted by the expected flux in each bin.

| Sample | Average Flux Uncertainty (%) | |
|---|---|---|
| | Super-K $\nu_\mu$ | Super-K $\nu_e$ |
| Before fit | 12.78 | 12.62 |
| $\nu_\mu$ | $5.27 \pm 0.04$ | $6.30 \pm 0.04$ |
| $\nu_\mu$, 2 bin $\nu_e$ and positive | $5.18 \pm 0.04$ | $6.08 \pm 0.04$ |
| $\nu_\mu$, 2 $\nu_e$ bins and positive ($5\times$ data) | $4.24 \pm 0.03$ | $5.12 \pm 0.03$ |

Table 5.2: The average uncertainty of the Super-K flux components after fitting the different samples. The average was calculated using weighted uncertainties and does not account for the expected flux in each bin.

## 5.8 Results: Inclusion of Super-K Flux Parameters

The fits performed in Section 5.7 only considered the ND280 flux parameters. In order to constrain the flux for oscillation measurements then the flux at Super-K needs to be constrained. The ND280 data can not directly constrain the flux at Super-K but the second term in Equation 5.4 provides the mechanism through which the Super-K flux parameters are constrained. The Super-K flux was binned in an identical way to the ND280 flux.

The reduction in the uncertainty of the Super-K flux bins is shown in Figure 5.8 for the $\nu_\mu$ flux (top) and $\nu_e$ flux (bottom). As seen with the ND280 flux components, a significant reduction is seen in the flux uncertainties after fitting the ND280 $\nu_\mu$ samples. The inclusion of the ND280 $\nu_e$ data clearly further reduces the uncertainty on the flux parameters and, as expected, has a larger effect on the Super-K $\nu_e$ flux than on the Super-K $\nu_\mu$ flux. The average uncertainty for each of the fits shown in Figure 5.8 is shown in Table 5.2. The table shows that the minimum achievable uncertainty on the Super-K $\nu_\mu$ and $\nu_e$ flux components are 4 % and 5 % respectively, using the data samples discussed.

## 5.9 Conclusions

It has been shown that the ND280 data can be used to constrain the uncertainty of the ND280 flux parameters and also the Super-K flux parameters using toy simulation fits and that the ND280 CC $\nu_e$ analysis can make an important contribution to this process. The reduction in the uncertainties presented here represents the best case scenario as only statistical uncertainties and the flux systematic uncertainties have been considered in the study. The effect of further data taking will improve the constraint of the flux parameters up until about five times the current amount of data after which further data provide diminishing returns to the reduc-

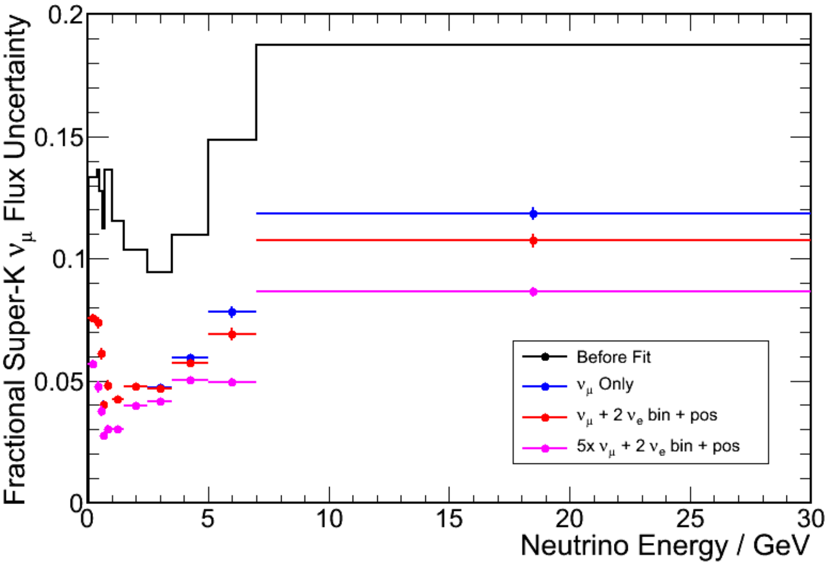

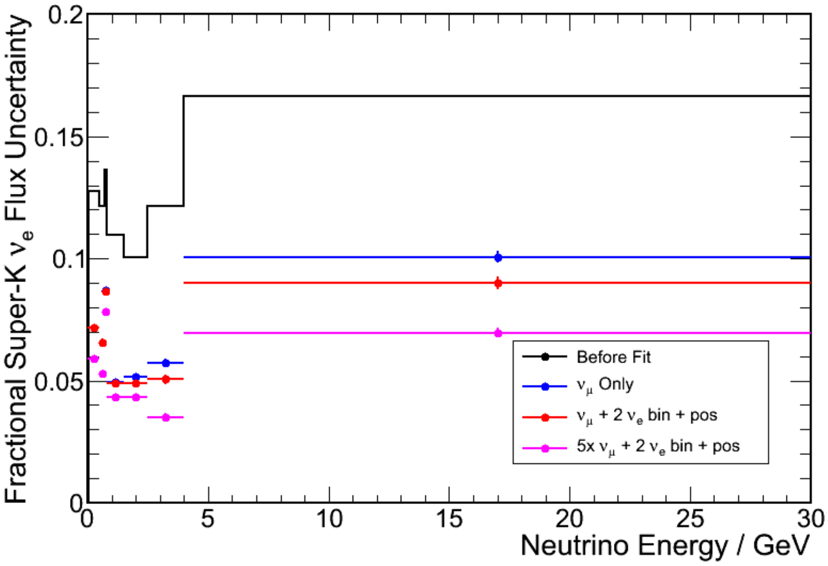

Figure 5.8: The flux uncertainty for the Super-K $\nu_\mu$ (top) and the $\nu_e$ (bottom) flux components. The black line shows the uncertainty before any fits were performed as a reference.

tion of the flux uncertainties. The method of using the ND280 data to constrain the flux parameters will give a minimum uncertainty on the ND280 and Super-K flux components of 4 % and 5 % for the $\nu_\mu$ and $\nu_e$ components respectively. In reality, the constraint will likely be less stringent due to the systematic uncertainties that were neglected in this study, associated with the interaction cross-sections and the detector.

As mentioned in Chapter 4, a flux constraint measurement could be replaced by a $\nu_e$ neutrino energy distribution measurement from the ND280, most likely for CCQE interactions. The uncertainty associated with this method would come from both the statistics in the energy distribution and from the systematic uncertainties associated with the ND280 measurement. When the amount of data is sufficient to bring this uncertainty down to a value that is lower than the uncertainty on the constrainted flux at Super-K then the energy distribution method could be adopted.

# Chapter 6

# Conclusions

A measurement of the intrinsic $\nu_e$ component of the T2K beam was made using the ND280 Tracker and DsECal. The ratio between data and simulation for the number of selected CC $\nu_e$ interactions was:

$$\frac{N(\nu_e)_{Data}}{N(\nu_e)_{Sim}} = 0.983 \pm 0.191(stat) \pm 0.076(syst)$$

The selection from the simulation was then used with the ND280 CC $\nu_\mu$ analysis to constrain the neutrino flux uncertainty. It was shown that even in the ideal case of no detector or cross-section systematic uncertainties that the minimum uncertainty on the neutrino flux was of the order of 4-5 %.

The recent measurements that show $\sin^2 2\theta_{13} \approx 0.1$ allow for the neutrino physics community to start to plan for measuring $\delta$. Three examples of proposed super-beam experiments are CERN to Pyhäsalmi[87], Hyper-Kamiokande[88] and LBNE[89]. These proposed experiments have coverage of approximately 70 % of the $\delta$ phase-space at the 90 % confidence level. These experiments plan to use beams with power of at least 1 MW and very massive far detectors. The far detector technology differs between the proposals, with LBNE and the CERN experiment prefering liquid Argon and Hyper-Kamiokande opting for water Čerenkov. However, the experiments all share the need to minimise the systematic uncertainties, hence the neutrino flux and the cross-sections need to be very well understood.

A new generation of detectors will be required to minimise the cross-section uncertainties as this will rely on detectors with a very high energy resolution. Liquid Argon detectors could prove to be vital in measuring neutrino interaction cross-sections to a high degree of accuracy. ArgoNeuT at Fermilab provided the first measurement of the neutrino cross-section on Argon in 2011[90], a measurement that is vital in relation to planned experiments such as GLADE[91] that would consist of a 5 kt liquid Argon detector at the NO$\nu$A far detector site. The GLADE detector would then act as a prototype for the very large scale liquid Argon detectors required for future measurements.

However, it was shown in Chapter 5 that even with zero cross-section uncertainties there was still a significant uncertainty on the neutrino flux. In the near future experiments such as NA61/SHINE will help to reduce these uncertainties with improved measurements of proton-target interactions. In the longer term, both the flux uncertainties and the $\nu_e$ beam contamination will become a limiting factor to conventional neutrino beam experiments so to further reduce flux uncertainties a different neutrino production mechanism will be required.

Muons always decay to produce neutrinos so they could be used provide the neutrino flux for an oscillation experiment. The proposed experiments of this type are called Neutrino Factories and store muons in a storage ring with two long, straight sections where the muons decay to produce a beam consisting of $\nu_\mu$ and $\bar{\nu}_e$ in equal proportion. The neutrino flux in this case could be known very accurately due to the relatively simple nature of the production mechanism. A second alternative is to use a Beta-Beam where radioactive ions circulate in the storage ring to produce a pure beam of $\bar{\nu}_e$ with a very well understood flux. The combination of a Neutrino Factory or a Beta-Beam with a liquid Argon far detector would allow for very high precision measurements to be made and is now becoming the focus of the global neutrino physics community.

# Appendix A

# DsECal at the CERN T9 Testbeam

The DsECal was taken to CERN in May 2009 to run in the T9 testbeam. The T9 testbeam is one of a series of testbeams originating from the proton synchrotron. The DsECal was placed inside a metal shipping frame in order to transport it first to CERN and then on to Japan. The shipping frame was not removed at the testbeam as it enabled the module to stand up. Unfortunatly, the frame was built in such a way that there was a lot of material in front of the front face of the DsECal. In order to minimise the effect of the shipping frame the detector was positioned so that the testbeam particles were incident on the back face. This was not a major problem because placing the detector backwards meant that the only difference for the particles was that they first traversed a layer of scintillator bars and then a layer of lead. Data were taken throughout May and June 2009 and the running period represented the first major running of the DsECal.

## A.1 The Beamline

A series of magnets were used to select particles of the desired charge and momentum. The current supplied to the magnets was reversed to switch the beam polarity from negative to positive and the magnitude of the current was used to control the momentum of the particles. The particle types present in the beam in negative and positive polarities are summarised in Table A.1.

| Beam Polarity | |
|---|---|
| Negative | Positive |
| $e^-$ | $e^+$ |
| $\pi^-$ | $\pi^+$ |
| | $p^+$ |

Table A.1: Particles in the T9 beamline at CERN.

## A.2 Beamline Particle Identification

There were two $CO_2$ filled Čerenkov detectors provided by CERN in the T9 beamline that were used to identify the particles in the beam. The two Čherenkov detectors were set up in such a way that electrons and positrons produced a signal but pions and protons did not.

In addition to the Čerenkov detectors, a Time-of-Flight (TOF) detector was positioned in front of the DsECal. The TOF was used to both trigger the detector and provide another source of particle identification. The time taken for a particle to travel between the two TOF paddles allowed the lighter particles (electrons, positrons and pions) to be distinguished from protons. This was possible because all particles in the beam have the same momentum and a proton travels more slowly than an electron for a given momentum. Figure A.1 shows the TOF signal for a positive polarity run at 600 MeV/c where the events are separated into two clear peaks, one for positrons and pions (left) and the other for protons (right).

Table A.2 shows how the information from the two Čerenkovs, TOF and beam polarity was combined to identify the particle. The table demonstrates that the Čerenkovs were used to separate the electrons and positrons from the hadronic particles and that the TOF was then used to distinguish between the pions and protons.

A special software package was written that extracted the information from the Čerenkovs and the TOF so that it could be used in the analysis of the testbeam data.

## A.3 Data Samples

Data were taken at a series of angles and momenta, consisting of three main running periods where the angle of the detector was changed between periods. The angles of indicence were: 0°, 30° and 60°. The angle was changed by lifting up the DsECal with a crane until it was just off of the ground and rotating it before placing it back

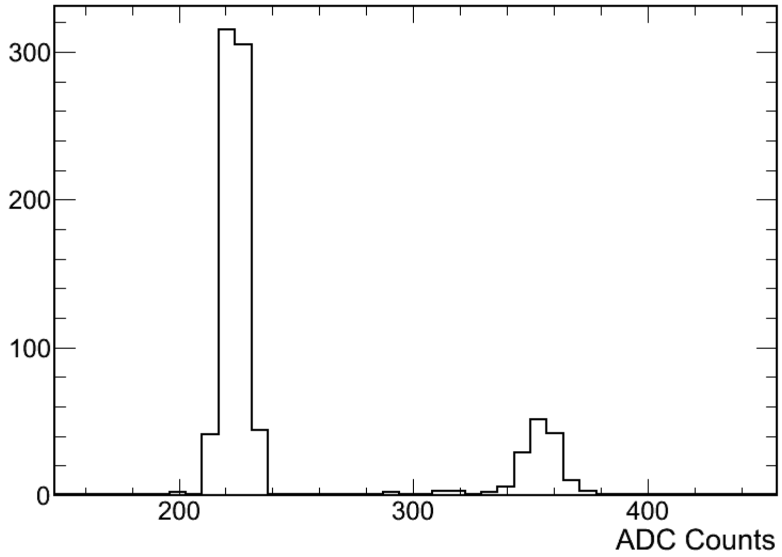

Figure A.1: The signal from the TOF for particles of 1GeV/c and positive charge. The left peak contains positrons and pions and the right peak contains protons.

| Particle | Čerenkov Signal<br>Čerenkov 1 | <br>Čerenkov 2 | TOF | Beam Polarity |
|---|---|---|---|---|
| $e^-$ | Yes | Yes | EM Peak | - |
| $e^+$ | Yes | Yes | EM Peak | + |
| $\pi^-$ | No | No | EM Peak | - |
| $\pi^+$ | No | No | EM Peak | + |
| $p$ | No | No | Proton Peak | + |

Table A.2: A summary of the beamline particle identification at the T9 Testbeam.

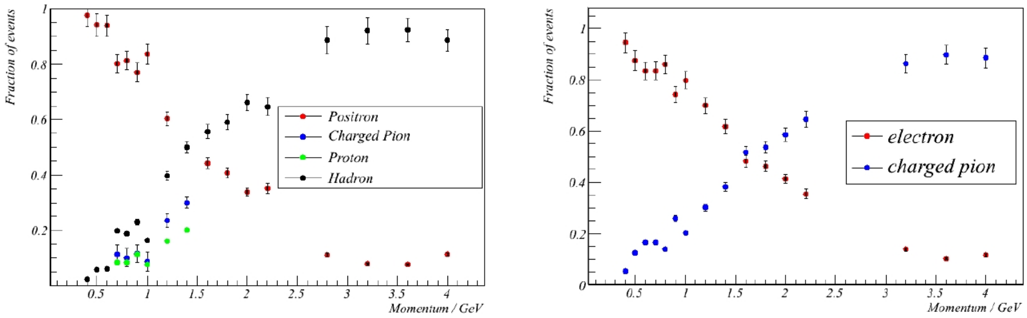

Figure A.2: The particle composition of the CERN T9 beam as a function of momentum for positively (left) and negatively (right) charged particles measured using the Čerenkov and TOF information. Figure taken from [92].

down. Data were taken at momenta ranging from 400 MeV/c to 4 GeV/c for both negative and positive beam polarity. Figure A.2 shows the fraction of each particle type as a function of momentum for both positive (left) and negative (right) beam polarities. The TOF was not able to distinguish protons from the other particle species[1] above 1.8 GeV/c and hence the pions and protons are labelled together as hadrons in the positive polarity figure for momenta above 1.8 GeV/c.

Figure A.2 also shows that the contents of the beam varied significantly with the beam momentum. For example, in the negative polarity runs the fraction of electrons is very large at low beam momentum but drops off until it is a fairly negligable component above approximately 2 GeV/c. It is hence clear that the number of electrons in the testbeam data is large for low momenta and becomes increasingly scarce as the momentum increases.

### A.3.1 Simulation

A simple Monte Carlo simulation was produced for each angle, momentum and particle type combination. The simulation did not include any simulation of the T9 beamline but simply fired particles of a given momentum into the back face of the DsECal.

---

[1] Above 1.8 GeV/c the protons were sufficiently relativistic that their time of flight was indistinguishable from that of the other particles in the beam.

# Bibliography

[1] D. Griffiths. *Introduction to Elementary Particles.* Wiley and Sons, Moerlenbach, Germany, 1987.

[2] E. Fermi. An attempt of a theory of beta radiation. 1. *Z. Phys.*, 88:161–177, 1934.

[3] H. Bethe and R. Peierls. The Neutrino. *Nature*, 133:532, 1934.

[4] F. Reines, C. L. Cowan, F. B. Harrison, A. D. McGuire, H. W. Kruse. Detection of the Free Antineutrino. *Phys. Rev. Lett.*, 117(1), 1960.

[5] G. Danby, J-M. Gaillard, K. Goulianos, L. M. Lederman, N. Mistry, M. Schwartz, and J. Steinberger. Observation of high-energy neutrino reactions and the existence of two kinds of neutrinos. *Phys. Rev. Lett.*, 9(1):36–44, 1962.

[6] K. Kodama et al. Observation of tau neutrino interactions. *Physics Letters B*, 504(3):218 – 224, 2001.

[7] K. Kodama et al. Final tau-neutrino results from the DONuT experiment. *Phys. Rev. D*, 78(5):052002, 2008.

[8] J.N. Bahcall, A.M. Serenelli and S. Basu. New Solar Opacities, Abundances, Helioseismology and Neutrino Fluxes. *ApJ*, 621(1), 2005.

[9] R. Davis, D. S. Harmer, and K. C. Hoffman. Search for Neutrinos from the Sun. *Phys. Rev. Lett.*, 20(21), 1968.

[10] Y. Fukuda et al. Solar Neutrino Data Covering Solar Cycle 22. *Phys. Rev. Lett.*, 77(9), 1996.

[11] Y. Fukuda et al. Measurements of the Solar Neutrino Flux from Super-Kamiokande's First 300 Days. *Phys. Rev. Lett.*, 81(6), 1998.

[12] K. Zuber. *Neutrino Physics*. Taylor and Francis, Oxon, United Kingdom, 2004.

[13] T.A. Kirsten et al. GALLEX solar neutrino results and status of GNO. *Physics Letters B*, 447(1), 1999.

[14] V.N. Gavrin et al. Solar neutrino results from SAGE. *Physics Letters B*, 447 (1), 1999.

[15] Q.R. Ahmad et al. Direct Evidence for Neutrino Flavor Transformation from Neutral-Current Interactions in the Sudbury Neutrino Observatory. *Phys. Rev. Lett.*, 89(1), 2002.

[16] Y. Fukuda et al. Evidence for Oscillation of Atmospheric Neutrinos. *Phys. Rev. Lett.*, 81(8), 1998.

[17] M. Apollonio et al. Search for neutrino oscillations on a long base-line at the chooz nuclear power station. *The European Physical Journal C - Particles and Fields*, 27:331–374, 2003. ISSN 1434-6044.

[18] F. Boehm et al. Final results from the Palo Verde neutrino oscillation experiment. *Phys. Rev. D*, 64(11):112001, 2001.

[19] N. Agafonova et al. Observation of a first nu-tau candidate in the opera experiment in the cngs beam. *arXiv*, hep-ex(1006.1623), 2010.

[20] P. Lipari, M. Lusignoli, and F. Sartogo. The Neutrino Cross Section and Upward Going Muons. *Phys. Rev. Lett.*, 74:4384–4387, 1995.

[21] G.T. Jones et al. Measurement of the neutral to charged current cross section ratios for neutrino and antineutrino interactions on protons. *Physics Letters B*, 178(23):329 – 334, 1986.

[22] C.H. Llewellyn Smith. Neutrino Reactions at Accelerator Energies. *Phys. Rept. 3*, 261(5):261–379, 1972.

[23] A. Bodek and U. Yang. Axial and Vector Structure Functions for Electron- and Neutrino- Nucleon Scattering Cross Sections at all $q^2$ using Effective Leading order Parton Distribution Functions. *arXiv*, hep-ex(1011.6592v1), 2010.

[24] B. Kayser. On the quantum mechanics of neutrino oscillation. *Phys. Rev. D*, 24(1):110–116, 1981.

[25] L.L. Chau and W.Y. Keung. Comments on the Parametrization of the Kobayashi-Maskawa Matrix. *Phys. Rev. Lett.*, 53(19):1802–1805, 1984.

[26] B. Pontecorvo. Electron and muon neutrinos. *Sov. Phys. JETP*, 10:1236–1240, 1960.

[27] Z. Maki, M. Nakagawa, and S. Sakata. Remarks on the unified model of elementary particles. *Progress of Theoretical Physics*, 28(5):870–880, 1962.

[28] Y. Itow et al. The JHF-Kamioka neutrino project. *arXiv*, hep-ex(0106019v1), 2001.

[29] K. Nakamura et al. (Particle Data Group). *J.Phys. G*, 37(075021), 2010.

[30] L. Wolfenstein. Neutrino oscillations in matter. *Phys. Rev. D*, 17:2369–2374, 1978.

[31] S. Mikheyev and A. Smirnov. Resonant Amplification of $\nu$ Oscillations in Matter and Solar-Neutrino Spectroscopy. *Il Nuovo Cimento C*, 9:17–26, 1986.

[32] B. Kayser. Neutrino Oscillation Phenomenology. *arXiv*, hep-ph(0804.1121v3), 2003.

[33] E. Majorana. Teoria simmetrica dellelettrone e del positrone. *Il Nuovo Cimento*, 14:171–184, 1937.

[34] P. Minkowski. $\mu \rightarrow e\gamma$ at a rate of one out of $10^9$ muon decays? *Physics Letters B*, 67(4):421 – 428, 1977.

[35] M. H. Ahn et al. Measurement of neutrino oscillation by the K2K experiment. *Phys. Rev. D*, 74(7):072003, 2006.

[36] Alec Habig and the Minos collaboration. Current MINOS neutrino oscillation results. *Journal of Physics: Conference Series*, 203(1):012102, 2010.

[37] D.G. Michael et al. The magnetized steel and scintillator calorimeters of the MINOS experiment. *Nucl. Inst. Methods Phys. Res. A*, 596(2-3):190 – 228, 2008.

[38] P. Adamson et al. Measurement of the Neutrino Mass Splitting and Flavor Mixing by MINOS. *Phys. Rev. Lett.*, 106(18):181801, 2011.

[39] P. Adamson et al. New constraints on muon-neutrino to electron-neutrino transitions in MINOS. *Phys. Rev. D*, 82(5):051102, 2010.

[40] P. Adamson et al. First Direct Observation of Muon Antineutrino Disappearance. *Phys. Rev. Lett.*, 107:021801, 2011.

[41] K. Abe et al. Indication of Electron Neutrino Appearance from an Accelerator-Produced Off-Axis Muon Neutrino Beam. *Phys. Rev. Lett.*, 107:041801, 2011.

[42] D. Ayres et al. NOvA Proposal to Build a 30 Kiloton Off-Axis Detector to Study Neutrino Oscillations in the Fermilab NuMI Beamline. *arXiv*, hep-ex (0503053v1), 2005.

[43] P. Vahle. The NOvA Experiment. In *Fermilab Users' Meeting*, 2011.

[44] S. Abe et al. Precision Measurement of Neutrino Oscillation Parameters with KamLAND. *Phys. Rev. Lett.*, 100(22):221803, 2008.

[45] H. De Kerret. First Results from the Double Chooz Experiment. In *LowNu, Seoul, Korea*, 2011.

[46] Y. Abe et al. Indication for the disappearance of reactor electron antineutrinos in the Double Chooz experiment. *arXiv*, hep-ex(1112.6353), 2011.

[47] F. Ardellier et al. Double Chooz, A Search for the Neutrino Mixing Angle theta-13. *arXiv*, hep-ex(0606025), 2006.

[48] F. P. An et al. Observation of electron-antineutrino disappearance at Daya Bay. *arXiv*, hep-ex(1203.1669), 2012.

[49] J.K. Ahn et al. RENO: An Experiment for Neutrino Oscillation Parameter theta_13 Using Reactor Neutrinos at Yonggwang. *arXiv*, hep-ex(1003.1391v1), 2010.

[50] J. K. Ahn et al. Obervation of Reactor Electron Antineutrino Disappearance in the RENO Experiment. *arXiv*, hep-ex(1204.0626v1), 2012.

[51] C. Athanassopoulos et al. Evidence for $\bar{\nu}\mu \rightarrow \bar{\nu}e$ Oscillations from the LSND Experiment at the Los Alamos Meson Physics Facility. *Phys. Rev. Lett.*, 77 (15):3082–3085, 1996.

[52] C. Athanassopoulos et al. Results on $\nu\mu \rightarrow \nu e$ Neutrino Oscillations from the LSND Experiment. *Phys. Rev. Lett.*, 81(9):1774–1777, 1998.

[53] A.A. Aguilar-Arevalo et al. Event Excess in the MiniBooNE Search for $\bar{\nu}\mu \rightarrow \bar{\nu}e$ Oscillations. *Phys. Rev. Lett.*, 105(18):181801, 2010.

[54] A.A. Aguilar-Arevalo et al. Search for electron neutrino appearance at the $\Delta m^2 \sim 1\text{eV}^2$ scale. *Phys. Rev. Lett.*, 98(23):231801, 2007.

[55] A.A. Aguilar-Arevalo et al. Unexplained Excess of Electronlike Events from a 1-GeV Neutrino Beam. *Phys. Rev. Lett.*, 102(10):101802, 2009.

[56] G. Mention at al. The Reactor Antineutrino Anomaly. *arXiv*, hep-ph (1101.2755), 2011.

[57] K. N. Abazajian et al. Light Sterile Neutrinos: A White Paper. *arXiv*, hep-ph (1204.5379), 2012.

[58] K. Abe et al. The T2K experiment. *Nucl. Inst. Methods Phys. Res. A*, 659(1): 106 – 135, 2011.

[59] S. Nakayama. Official plots for Summer 2011 results. URL `http://www.t2k.org/docs/plots/011/`.

[60] S. Agostinelli et al. Geant4 - a simulation toolkit. *Nucl. Inst. Methods Phys. Res. A*, 506(3):250 – 303, 2003.

[61] G. Battistoni et al. The FLUKA code: description and benchmarking. *AIP Conf. Proc.*, 896:31–49, 2006.

[62] A. Laszlo for the NA61 Collaboration. NA61/SHINE at the CERN SPS. *PoS CPOD07*, (054), 2007.

[63] J. Allaby et al. *High-energy particle spectra from proton interactions at 19.2 GeV/c.* CERN, Geneva, 1970.

[64] T. Eichten et al. Particle production in proton interactions in nuclei at 24 GeV/c. *Nuclear Physics B*, 44(2):333 – 343, 1972.

[65] K. Abe et al. Measurements of the T2K neutrino beam properties using the INGRID on-axis near detector. *arXiv*, hep-ex(1111.3119), 2011.

[66] A. Vacheret. Characterization of the 1.30 mm × 1.30 mm mppc for the t2k near detectors. *Nucl. Inst. Methods Phys. Res. A*, 623(1):201 – 203, 2010.

[67] T2K Collaboration. Photographs. . URL `http://www.t2k.org/docs/photos/nd280/`.

[68] K. Ieki. Fgd beam official plots for 2010a data period. URL `http://www.t2k.org/docs/plots/006/`.

[69] S. Fukuda et al. The Super-Kamiokande detector. *Nucl. Inst. Methods Phys. Res. A*, 501(2-3):418 – 462, 2003.

[70] T2K Collaboration. T2K Sensitivity with 30 GeV Beam at SK. . URL `http://www.t2k.org/docs/plots/001/`.

[71] T.S. Virdee. Experimental techniques. oai:cds.cern.ch:454176. (CERN-OPEN-2000-261), 1999.

[72] Y. Uchida et al. Official ECAL Plots for Summer 2011. URL `http://www.t2k.org/docs/plots/011/nd280/ecal/plots`.

[73] A. Carver. Particle Identification in the ND280 Electromagnetic Calorimeter. *T2K Technical Note*, T2K-TN-002, 2009.

[74] A. Hoecker et al. TMVA: Toolkit for Multivariate Data Analysis with ROOT. *PoS ACAT*, 040, 2007.

[75] Rene Brun and Fons Rademakers. ROOT - An Object Oriented Data Analysis Framework. *Nucl. Inst. Methods Phys. Res. A*, 389:81–86, 1997.

[76] N. Abgrall et al. Neutrino Flux Prediction for the 2010a Analysis. *T2K Technical Note*, T2K-TN-038, 2011.

[77] C. Andreopoulos et al. The GENIE neutrino Monte Carlo generator. *Nucl. Inst. Methods Phys. Res. A*, 614(1):87 – 104, 2010.

[78] C. Bojechko et al. CCQE-like and CC-non-QE-like numu event selections in the ND280 tracker using Run 1+2 data. *T2K Technical Note*, T2K-TN-093, 2012.

[79] C. Giganti et al. Measurement of NuE beam component with Run1+Run2 data using the ND280 Tracker. *T2K Technical Note*, T2K-TN-094, 2012.

[80] W. Verkerke and D. Kirkby. The roofit toolkit for data modeling. *arXiv*, physics.data_an(0306116v1), 2003.

[81] L. Escudero. Study of TPC momentum resolution from tracks that cross multiple TPCs and the associated systematic error on the $\nu_\mu$ CC and CCQE analyses. *T2K Technical Note*, T2K-TN-095, 2011.

[82] C. Giganti et al. Study of neutrino charged current interactions in the ND280 tracker. *T2K Technical Note*, T2K-TN-015, 2011.

[83] J. Caravaca et al. Charge Misidentification in local and global reconstruction. *T2K Technical Note*, T2K-TN-048, 2011.

[84] C. Bojechko et al. Measurement and Correction of Magnetic Field Distortions in the TPCs. *T2K Technical Note*, T2K-TN-061, 2012.

[85] C. Andreopoulos et al. Handling Neutrino Interaction Uncertainties using Event Reweighting. *T2K Technical Note*, T2K-TN-007, 2009.

[86] P. de Perio et al. Constraining the Flux and Cross Section Models with Data from the ND280 Detector for the 2012a Oscillation Analysis. *T2K Technical Note*, T2K-TN-106, 2012.

[87] A. Rubbia. Expression of Interest for a very long baseline neutrino oscillation experiment (LBNO). In *European Strategy for Neutrino Oscillation Physics - II, CERN*, 2012.

[88] K. Abe at al. Letter of Intent: The Hyper-Kamiokande Experiment - Detector Design and Physics Potential. *arXiv*, hep-ph(1109.3262), 2011.

[89] M. V. Diwan. The Science and Strategy for Phasing of the Long-Baseline Neutrino Experiment. *LBNE Technical Note*, LBNE-doc-5962, 2012.

[90] C. Anderson at al. First Measurements of Inclusive Muon Neutrino Charged Current Differential Cross Sections on Argon. *arXiv*, hep-ph(1111.0103), 2011.

[91] J. Thomas. GLADE: an opportunity for LAr exploitation in the NuMI beam. In *LAGUNA Collaboration Meeting*, 2012.

[92] A. Carver. *Effect of a particle identification algorithm in the ND280 ECal on an electron neutrino analysis.* PhD thesis, University of Warwick, 2009.